OUKA
Osaka University Knowledge Archive

Title	Thermal degradation mechanisms of package materials for high-temperature power modules
Author(s)	崔, 讃揚
Citation	大阪大学, 2020, 博士論文
Version Type	VoR
URL	https://doi.org/10.18910/76530
rights	
Note	

Osaka University Knowledge Archive : OUKA

https://ir.library.osaka-u.ac.jp/

Osaka University

Doctoral Dissertation

Thermal degradation mechanisms of package materials for high-temperature power modules

Chanyang Choe

January 2020

Department of Adaptive Machine Systems
Graduate School of Engineering
Osaka University

Ph.D. Dissertation

Thermal degradation mechanisms of package materials for high-temperature power modules

by

Chanyang Choe

Department of Adaptive Machine Systems

Graduate School of Engineering

Osaka University

January 2020

Approved by

Professor Katsuaki Suganuma

Professor Hiroshi Utsunomiya

Associate Professor Shijo Nagao

Associate Professor Tohru Sugahara

Thermal degradation mechanisms in package materials for high-temperature power modules

Abstract

Wide-bandgap (WBG) semiconductor materials, such as silicon carbide (SiC) and gallium nitride (GaN), are being increasingly used, and provide significant opportunities to develop power electronic systems with high power densities, high reliability in extreme environments, and high integration. The development of high-temperature-operating power devices enables the use of power modules at high temperatures (>250 °C). The aforementioned power modules have a multi-layered packaging structure that comprises four main components, namely, semiconductors, joints, substrates, and wires. Under high-temperatures, large thermal stress occurs in the power module as coefficients of thermal expansion (CTE) mismatch among multiple layers, resulting in thermal damage. This thesis describes thermal degradation mechanisms in joints and substrates under high-temperature. In addition, a novel real-time monitoring method for damage via acoustic emission (AE) technique is presented.

First, to evaluate the thermal degradation mechanisms in sintered micro-porous silver (Ag), which is regarded as a promising joint material for fabricating high-temperature power modules because of its mechanical/electrical properties, its deterioration and microstructural variations were investigated under high-temperature and correlated with each other. Sintered Ag was fabricated in a specimen shape of a tension test by printing and sintering at 250 °C for 1 h in air without pressure. The sintered Ag was exposed to 250 °C for 1000 h. Subsequently, its tensile strength and electrical resistivity were measured. The tensile strength of the sintered Ag decreased initially, but recovered subsequently during the high-temperature exposure, while its electrical resistivity decreased. For microstructure evolution, sintered Ag grains, their porous structure and fracture surface were characterized by SEM and EBSD. The relationship between their microstructural variations and mechanical/electrical properties was discussed.

The thermal shock damage mechanisms in direct bonded aluminum (DBA) and active metal brazing (AMB) substrates with two types of plating—Ni electroplating and Ni–P electroless plating—were evaluated by thermal shock tests between −50 °C and 250 °C. The AMB substrates with Al_2O_3 and AlN fractured only after 10 cycles, but with Si_3N_4 ceramic, they retained good thermal stability even after 1000 cycles, regardless of the metallization type. The Ni layer on the surviving AMB substrates with Si_3N_4 was not damaged, while a crack occurred in the Ni–P layer. For the DBA substrates, fracture did not occur up to 1000 cycles for all kinds of ceramics. However, the Ni–P layer roughened and cracked because of the severe deformation of the aluminum layer, while the Ni layer was not damaged after the thermal shock tests. In addition, the deformation mechanism of an Al plate on a ceramic substrate was investigated both by microstructural observation and finite element method (FEM) simulation, which confirmed that grain boundary sliding was a key factor in the severe deformation of the Al layer. The deformation resulted in the cracking of the Ni–P layer. The fracture suppression in the Ni layer on DBA/AMB substrates can be attributed to its ductility and higher strength compared with those of Ni–P layer.

Finally, the wear-out damage mechanism in discrete SiC power devices was evaluated by performing a power cycling test (PCT), and acoustic emission (AE) technique was applied to monitor the damage in real-time for the first time. AE is an excellent method to monitor material damage during operation. The discrete devices were fabricated using a SiC diode, Ag sintering die-attachment, and Al ribbon interconnection. PCT was carried out with a harsh junction temperature swing of Δ 150 °C to accelerate the damage occurrence, and AE signals were collected simultaneously using an AE sensor that attached to the discrete devices. The AE cumulative counts, which represent the main characteristic of AE signals, were increased with the number of cycles during PCT, while the thermal fatigue crack propagated in the Al ribbon. The relationship between the AE count rate and the observed fatigue crack propagation was confirmed. The result demonstrates that AE evaluation can be used not only for

understanding the fatigue progress of Al ribbons but also for monitoring the failure of power electronic devices.

In this thesis, the results suggest new damage mechanisms for sintered micro-porous Ag and Ni metalized DBA/AMB substrates under high-temperature, and additionally, propose a novel AE monitoring method for analyzing the thermal fatigue damage in power modules.

Table of contents

Abstract I

Table of contents II

List of tables V

List of figures Ⅵ

Chapter 1 Introduction 1

1.1 Packaging materials and structure for high-temperature power modules 2

1.1.1 Next generation wide bandgap power semiconductors 2

1.1.2 Packaging structure of power modules and reliability issue 4

1.2.3 High-temperature packaging material and its failure mechanisms 6

1.2 Real-time monitoring of thermal fatigue damage 8

1.2.1 Traditional failure precursor monitoring 8

1.2.2 Definition of acoustic emission (AE) monitoring 10

1.2.3 Sources and characteristics of AE signals 12

1.2.4 AE system configuration 14

1.2.5 AE signal characteristics and noise cancelling process 15

1.3 Objective and outline of the thesis 17

Reference 19

Chapter 2 Thermal degradation mechanism of micro-porous silver die-attach 25

2.1 Introduction 26

2.2 Experimental 28

2.2.1 Fabrication of sintered porous Ag specimens 28

2.2.2 Characterization of mechanical/electrical properties 29

2.2.3 Microstructural observation 29

2.3 Results and discussion 32

2.3.1 Deterioration of tensile strength and electrical resistivity 32

2.3.2 Changes in Ag grains and porous structure 33

2.3.3 Relationship between mechanical/electrical properties and microstructural variation 37
2.3.4 Evaluation of fracture surface 39
2.4 Conclusions 40
References 41

Chapter 3 Thermal shock damage mechanism of DBA/AMB substrates plated with Ni and with Ni–P layers 44
3.1 Introduction 45
3.2 Materials and methods 47
3.3 Results and discussion 51
3.3.1 Thermal shock behavior 51
3.3.2 Cracking mechanism of Ni–P layer 59
3.3.3 FEM simulation 61
3.4 Conclusion 63
References 64

Chapter 4 Real-time Al ribbon fatigue monitoring by using AE 68
4.1 Introduction 69
4.2 Experiment 72
4.2.1 The tested discrete devices 72
4.2.2 Power cycling test (PCT) system and setup 74
4.2.3 Acoustic emission (AE) monitoring system and setup 77
4.2.4 Background AE noise cancelling process and setup 79
4.3 Power cycling test 81
4.3.1 Voltage precursor parameter monitoring in power cycling test 81
4.3.2 Physics-of-failure analysis of the tested discrete devices 84
4.4 Acoustic emission monitoring test 87
4.4.1 The source of acoustic emission 87
4.4.2 Monitoring by acoustic emission parameter 89
4.5 Conclusion 93
References 94

Chapter 5 Conclusions 100

List of Publications and Presentations 104

Acknowledgments 109

List of tables

Table		Page
1.1	Physical properties of Si and WBG semiconductors [4, 6].	3
1.2	Mechanism, causes, and precursors of failure in packaging components.	9
1.3	Factors affecting AE response [50].	13
1.4	Typical frequency range of noise in common industries.	16
3.1	Materials and dimensions of multilayered specimens.	48
3.2	Mechanical and thermal properties of the various materials in Ni- and Ni–P-plated DBA/AMB substrates.	50
4.1	Power cycling test condition.	76

List of figures

Figure		Page
1.1	Junction temperature limits according to the breakdown voltage of Si and WBG semiconductors [5]	3
1.2	Packaging structure, materials, and their coefficients of linear thermal expansion (CTE) property in high-temperature power modules	5
1.3	Applications of the Ag sinter paste: (a) joint and clip bonding and (b) printed Ag sinter wire [17, 18].	7
1.4	AE signal generation, propagation, and detection [47].	11
1.5	Burst and continuous AE signals [41].	13
1.6	Illustration of commonly used AE parameters [41].	16
2.1	Fabrication process of Ag specimens for tensile and four probe tests (a-c) and its micro-porous structure observed by SEM (d).	30
2.2	Configuration of a tensile test (a) and four probe resistivity measurement (b) for sintered Ag specimens.	30
2.3	Automatic measurement of pore area and number of sintered Ag.	31
2.4	Deterioration of tensile strength and resistivity of sintered Ag during thermal exposure.	32
2.5	EBSD observation of Ag specimens after different exposure times; (a) 0 h, (b) 200 h, (c) 500 h and (d) 1,000 h.	33
2.6	Variation in Ag grain size and number with thermal exposure time.	34
2.7	Variation in average pore area and number with thermal exposure time.	34
2.8	Variation in porosity of sintered Ag with thermal exposure time.	36
2.9	SEM observations of the fracture surface of Ag specimens aged for different exposure times; (a) 0 h, (b) 50 h, (c) 200 h, (d) 500 h and (d) 1000 h.	39
3.1	(a) Macrograph of a typical substrate specimen, (b) cross-section diagrams of the DBA/AMB substrates plated by Ni and Ni–P layers, surface morphology of Ni (c) and Ni–P (d) layer on the substrates, and surface microstructure of Al (e) and Cu (f) of the DBA/AMB substrates.	48
3.2	FEM model for thermal stress distribution simulation of an AMB substrate with Si_3N_4.	50
3.3	Destructed AMB substrates with Al_2O_3 (a, d) and AlN (b, e) after 10 cycles, nondestructed AMB substrates with Si_3N_4 (c, f) after 1000 cycles plated with Ni (a-c) and Ni–P (d-f), and (g) fracture pattern of AMB substrates.	52

3.4 Surface variation of Ni (a,b) and Ni–P (c,d) layers on AMB substrates with Si_3N_4 before and after 1000 cycles. 53
3.5 Scanning acoustic tomography (SAT) observation of the surface morphology of the Ni–P layer on AMB substrates with Si3N4 after different thermal shock tests: 0, 50, 100, and 1000 cycles. 53
3.6 DBA substrates with Al2O3, AlN, and Si_3N_4 after 1000 cycles, plated with Ni (a–c) and Ni–P (d–f). 55
3.7 Surface morphology of Ni (a,b) and Ni–P (c,d) layers on DBA substrates with Si_3N_4 before and after 1000 cycles. 55
3.8 SAT observation of the surface morphology of a Ni–P layer on DBA substrates with Al_2O_3 (a–d), AlN (e–h), and Si3N4 (i–l) after different thermal shock tests: 0, 50, 100, and 1000 cycles. 57
3.9 Laser surface observation of the Ni–P layer on DBA substrates with Si_3N_4 at the initial state (a) and after 1000 cycles (b,c). Local area with cracked (b) and roughened (c) area, and its roughness profile (d–f) measured by a line profile corresponding to (a–c), respectively. 57
3.10 Variation in surface roughness of Ni (a) and Ni–P (b) layers on DBA/AMB substrates with Al_2O_3, AlN, and Si_3N_4 up to 1000 cycles. 58
3.11 Variation in surface roughness of Ni (a) and Ni–P (b) layers on DBA/AMB substrates with Al_2O_3, AlN, and Si_3N_4 up to 1000 cycles. 60
3.12 SEM observation of bare aluminum surface in DBA substrates with Si_3N_4 at the initial state (a) and after thermal shock tests of 100 cycles (b), and FIB-milled cross section (c) at the location of surface deformation. 60
3.13 Maximum principal stress distribution for Ni and Ni–P layers on DBA/AMB substrates with Si_3N_4 at 250 °C during thermal shock cycling test. 62
4.1 Generation, propagation, and collection process of acoustic emission signals (i.e. elastic waves) in power electronics during PCT. 71
4.2 Fabricated discrete SiC-SBD devices; (a) optical image and (b) its cross-section SEM image. 73
4.3 Configuration of power cycling test system and real-time acoustic emission monitoring system. 75
4.4 Profile of voltage and current during power cycling tests. 76
4.5 Waveform of a collected AE signal and its characteristic including counts and amplitude. 78
4.6 Dummy specimens designed for noise cancelling and (b-d) Typical waveform and frequency spectrum of three types of collected noise; (a) cable noise, (b) cooling fan movement noise and (c) electromagnetic induction noise. 80
4.7 Variation in forward voltage of a diode during PCT tests. 82
4.8 I-V characteristics before and after PCT tests under. 83
4.9 Failure analysis results of failed discrete SiC-SBD devices after PCT tests; (a) lift-off failure of one Al ribbon, (b) fracture surface of lift-off ribbon, (c) magnified 85

observation of crack initiation, and (d) magnified observation of fatigue fracture marks.

4.10 (a) Cross-section observation of another unfractured ribbon portion after PCT tests and (b) a magnified cross-section image of Ag sinter joint. 86

4.11 Micro-focused X-ray inspection results of Ag sinter joint in devices before (a) and after (b) PCT tests. 86

4.12 (a) Dummy specimens designed for noise cancelling and (b) typical waveform and frequency spectrum of three types of collected noise. 88

4.13 Waveform (a-b) and its corresponding frequency spectrum (c-d) of typical AE signals collected during PCT tests. 88

4.14 Histogram of the measured central frequency of collected AE signals. 91

4.15 Monitoring result of time-domain parameters during PCT tests with the monitoring results of forward voltage; (a) cumulative counts, (b) cumulative count rate, and (c) amplitude. 92

4.16 Cumulative counts of collected AE signals during switching ON and OFF period of PCT tests. 92

Chapter 1

Introduction

1.1.1 Next generation wide bandgap power semiconductors

Power electronic modules, such as converter and inverter systems, have been widely used in transportation applications, such as electric vehicles, aircrafts, and high-speed trains. Owing to the increasing demand for power density, efficiency, and switching frequency, traditional power modules based on Si materials cannot satisfy these demands because of the theoretical performance limit of Si materials [1–3]. Therefore, to address the high-performance challenges of power modules, Si devices have been replaced with wide bandgap (WBG) devices containing materials such as silicon carbide (SiC) and gallium nitride (GaN) because of their remarkable physical properties, as listed in Table 1.1 [4–6].

Many researchers have reported the high performance of power modules that are based on WBG devices. Compared with Si IGBTs, SiC MOSFETs achieve higher efficiency and switching frequency, since they reduce the switching loss. Although the converters based on Si IGBTs and Si MOSFETs are operated at a switching frequency less than 10 kHz, converters based on SiC MOSFETs can be operated at a frequency higher than 150 kHz using the same power [7, 8].

In addition, WBG semiconductors conveniently perform high temperature and high power density operations because of their higher breakdown temperature and voltage. Fig. 1.1 shows the minimum junction temperature at which breakdown failure occurs. WBG semiconductors enable operations at high-voltages up to 100 kV, as they can perform even at the high-temperature of 400 °C without device breakdown failure. However, Si devices are limited to only a few hundred voltages and lower junction temperature because of their breakdown failure [9–11].

Table 1.1 Physical properties of Si and WBG semiconductors [4, 6].

	Si	3C-SiC	4H-SiC	3C-GaN	2H-GaN	Diamond
Bandgap energy, E_g (eV)	1.12	2.2	3.26	3.27	3.39	5.45
Critical electric field, E_c (Vcm^{-1})	11.8	9.6	10	1	3.3	5.6
Electrical mobility, μ_n ($cm^2 \cdot V^{-1} \cdot s^{-1}$)	1350	900	720	1000	900	1900
Saturation velocity, ν_{sat} ($cm \cdot s^{-1}$)	1.0	2.0	2.0	2.6	2.5	2.7
Thermal conductivity, λ ($W \cdot cm^{-1} \cdot K^{-1}$)	1.5	4.5	4.5	1.3	1.3	20
Dielectric constant, ε_r	11.8	9.6	10	9.9	8.7	5.5

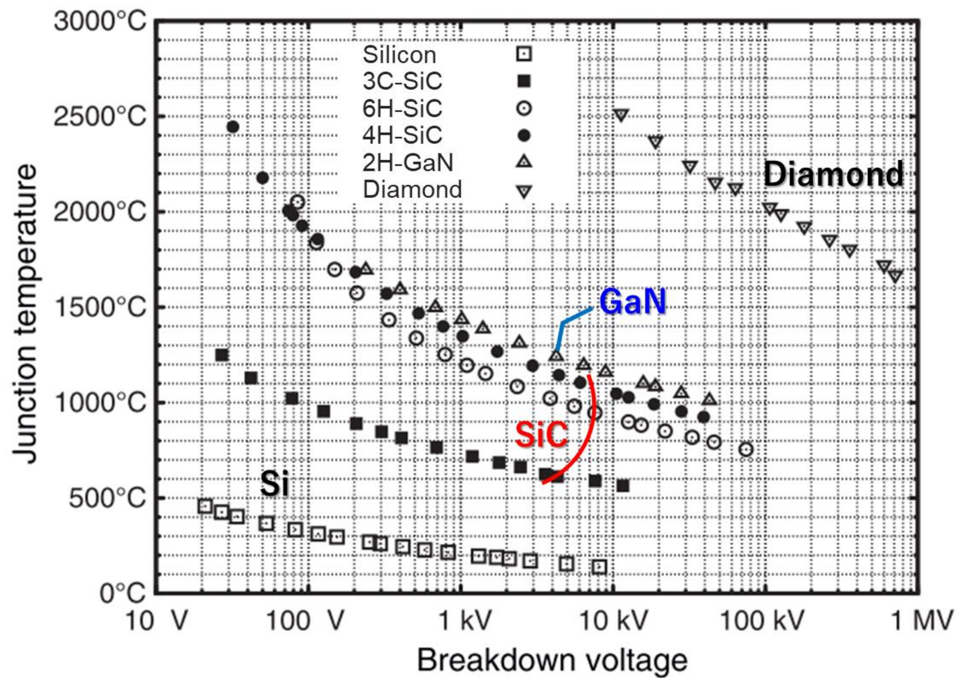

Fig. 1.1 Junction temperature limits according to the breakdown voltage of Si and WBG semiconductors [5].

1.1.2 Package structure of power modules and reliability issue

Generally, conventional power modules have a multi-layered packaging structure that includes five main components, namely, wires, semiconductor devices, die-attach joints, substrates, and baseplates, as shown in Fig. 1.2. Power devices are soldered to ceramic substrates such as direct bonded copper (DBC) and direct-bonded aluminum (DBA). Wires are interconnected between the devices and the metal layer in patterned substrates. Subsequently, the fabricated modules are bonded on a base plate by soldering.

Multilayered package structures are effective in reducing the volume of modules and dissipating heat. However, as seen in Fig. 1.1. To maximize the advantages of the power modules of WBG semiconductors, the modules must operate at a higher junction temperature of approximately 250 °C. In addition, its applications, such as automobiles, aircrafts, and space exploration, currently require power modules to operate in ambient thermal cyclic environments. In automobile industries, environment temperatures under the hood can reach or exceed 150 °C. It can also drop to − 40 °C and the temperature swing is repeated [12]. In aircrafts, the modules are thermally cycled using a wide temperature range from –55 °C to 300 °C and more [13, 14]. In such a high-temperature operating environment, high thermal stress occurs repeatedly at the interface of mutilated structure in a power module because of the mismatch of the coefficients of thermal expansion (CTE) among multiple layers, resulting in significant thermal damage and reliability problem. However, the existing conventional package materials are not appropriate, as they are limited to the maximum junction temperature of 175 °C.

To ensure the reliability of modules, new packaging materials with high damage resistance in extremely severe operation conditions must be developed, and their failure mechanism must be evaluated.

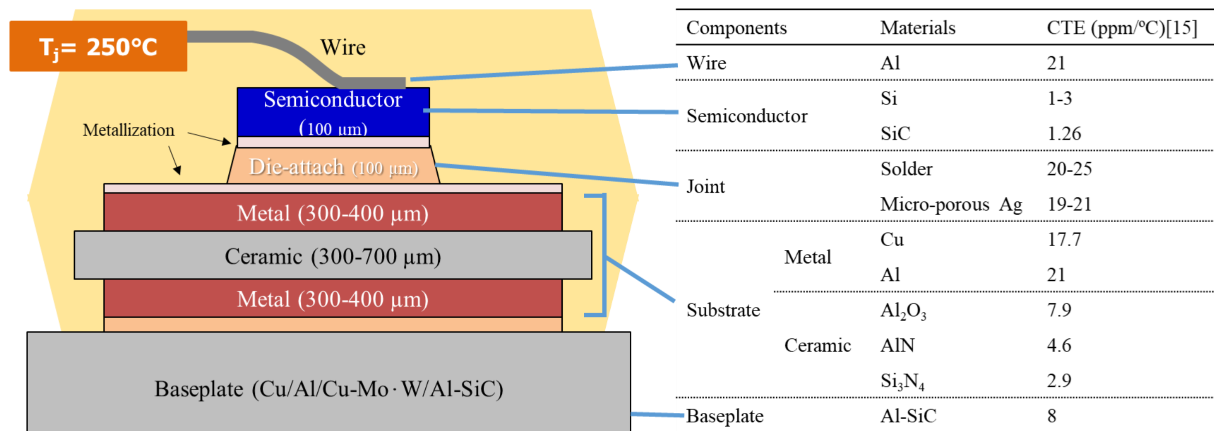

Components		Materials	CTE (ppm/°C)[15]
Wire		Al	21
Semiconductor		Si	1-3
		SiC	1.26
Joint		Solder	20-25
		Micro-porous Ag	19-21
Substrate	Metal	Cu	17.7
		Al	21
	Ceramic	Al_2O_3	7.9
		AlN	4.6
		Si_3N_4	2.9
Baseplate		Al-SiC	8

Fig. 1.2 Packaging structure, materials, and their coefficients of linear thermal expansion (CTE) property in high-temperature power modules.

1.1.3 High-temperature packaging material and its failure mechanisms

For high-temperature interconnection materials, several materials with excellent thermal and electrical properties, such as silver (Ag), gold, and copper (Cu), have been proposed as sinter joining pastes. Additionally, these materials have higher melting points than solder materials. Among them, Ag sinter pastes have been considered as the most promising joining materials because of their excellent characteristics. Ag sinter pastes exhibit a higher bonding strength, lower resistivity, and higher thermal reliability than Au–Sn solder and transient liquid phase (TLP) materials, which can be used at higher temperatures (> 250 °C). Additionally, low-cost micron- and submicron-sized Ag pastes have been developed, thereby widening the possibility of using Ag sinter pastes in power electronics industries [16]. Recently, Ag pastes have been attempted to be widely used not only as joining materials but also for wire interconnections in the form of Ag clip bonding [17] and printed Ag sinter wire [18], as shown in Fig. 1.3.

The mechanism of property deterioration and microstructural changes in sintered Ag joints has been investigated under high temperature. In addition, grain growth, pore coarsening, and increasing porosity of sintered Ag joints in die attach have been studied as the mechanism of the strength decrease [19]. In a thermal shock environment, it was reported that a vertical crack occurred in a sintered Ag joint layer during a thermal shock test for temperatures from − 50 °C to 250 °C [20].

For power package substrates, both direct bonded aluminum (DBA) and active metal brazing (AMB) substrates have been considered as promising substrates for fabricating high-temperature power electronic modules because of their good thermal conductivity, low electrical resistance, and high insulation voltage. The aforementioned advantages are attributed to the metal/ceramic/metal sandwich structure of DBA/AMB substrates. Notably, DBA/AMB

substrates have a ceramic insulator plate composed of materials such as Al_2O_3, AlN, and Si_3N_4. Both the sides of the insulator plate are metalized using aluminum (Al) or copper (Cu) to function as a thermal and electrical conductor layer. The as-prepared metal layer not only improves thermal conductivity but also creates electrical circuits on the insulator plate. However, the sandwich structure of DBA/AMB substrates also results in high thermomechanical stress, which is induced by the difference of CTEs between metal and ceramic in the sandwich structure during temperature cycling. Particularly, AMB substrates, which are bonded using a brazing process, have high thermal resistivity than that of the widely used direct bonded copper (DBC), which is bonded using eutectic bond. Although the need for high-temperature packaging technologies has been increasing, the reliability issues of DBA/AMB substrates still remain unaddressed.

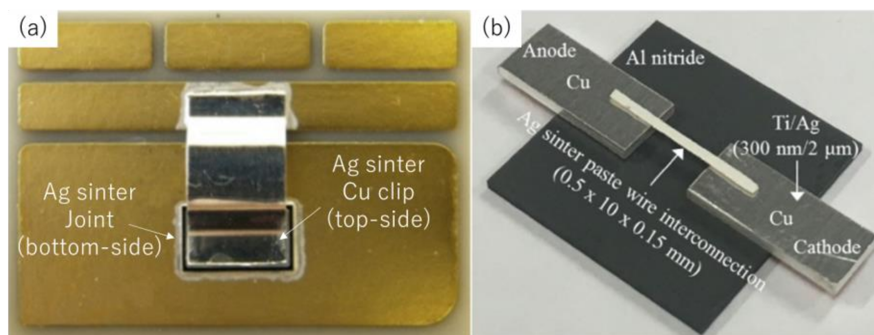

Fig. 1.3 Applications of the Ag sinter paste: (a) joint and clip bonding and (b) printed Ag sinter wire [17, 18].

1.2 Real-time monitoring of thermal fatigue damage

1.2.1 Traditional failure precursor monitoring

Two types of lifetime prediction methods have been studied for power modules. The first method is based on failure mechanism. The lifetime prediction models are based on various failure mechanisms and describe the number of cycles to failure (Nf) as a function of failure-relevant temperature parameters such as the junction temperature swing (ΔTj) and mean junction temperature (Tm). The second method is based on failure precursor parameters. Compared to the first method, this method is typically used to predict remaining useful life (RUL) and to monitor damage progress. Several studies have focused on thermal fatigue damage monitoring in both devices and packaging components, as listed in Table 1.2. However, there are certain disadvantages of second method:

1. It needs an additional electric circuit for monitoring [21].
2. It cannot predict the status of fatigue damage and time of failure [22].
3. Variation in one precursor parameter can affect the other parameters [23].

Table 1.2 Mechanism, causes, and precursors of failure in packaging components.

Components		Failure mode	Mechanism	Precursor parameter	Ref
Semiconductor	Die	- Short circuit - Burn-out - Loss of gate control	- Latch-up - Break- down	- $V_{CE(ON)}$ - t_{off} - $_{GE(th)}$	[24]
	Bond pad	- Void/Crack	- Metallization reconstruction	-	-
Wire	Bond interface	- Liftoff	- Fatigue - Reconstruction	- t_{on}/t_{off} - $V_{CE(ON)}$ - V_{GE}	[25-28]
	Heel	- Heel cracking	- Fatigue	- $V_{CE(ON)}$	[29]
	Body	- Wire burnout	- Joule heating	- $V_{CE(ON)}$	[30]
		- Void	- Stress corrosion	-	-
Solder joint		- Crack - Delamination	- Fatigue or grain growth	- R_{th} - $V_{CE(ON)}$ - t_{off}	[31-33]
Ceramic substrates		- Fracture	- Fatigue, Brittle fracture	- R_{th}	

1.2.2 Definition and application of acoustic emission monitoring

Acoustic emission is defined as a physical phenomenon that elastic energy is dynamically released as a result of material damage, as shown in Fig. 1.4. The released elastic energy propagates in the form of elastic waves inside the material. The waves that reach the surface cause surface deformations and can be detected using piezoelectric transducers. The detected elastic waves are transferred to electric signals called AE signals. AE signals contain damage information, as they result from a specific damage. The AE signals analysis enables various assessments. In the widest sense, acoustic emission is a technique for evaluating material damages by collecting and analyzing the released elastic waves [34, 35].

In metallurgical fields, the AE phenomenon was first studied in 1933 to evaluate the martensite transformation of Ni steel [36]. Thereafter, the AE system and method have been developed and extensively used for monitoring the damage of large structures such as bridges, pressure vessels, and wind turbines [37, 38]. Most AE methods have been standardized based on American Society for Testing and Materials (ASTM) standards (ASTM E 569, E 749, E 751, E 1067, E1139) [39]. In addition, several recent studies have applied the AE methods to evaluate fracture and cracks in advanced microelectronics such as ceramic-metal joints [40], lithium-ion batteries [41–43], multi-layered ceramic capacitors [44], and fuel cells [45].

An AE method is a nondestructive technique related to the passive monitoring of ultrasound. Passive-type AE methods offer significant advantage over other nondestructive techniques. Firstly, a sensor can measure damage in a wide area and the measurement system is much simpler. The AE signals arising from the damage can be detected by a sensor attached to the surface of a test object as the signals can spread in all directions within a solid. Secondly, standby power consumption is much lower for monitoring. Most nondestructive techniques usually input energy and collect the input energy after the reaction with test objects. The AE

method is a passive-type of technique, and thus, does not need to input energy. Thirdly, AE system is composed of fewer elements. Thus, it is easy to implement in industries. On the other hand, a modified scanning acoustic tomography (SAT) system was proposed to observe the degradation of power modules under power cycling test [46]. However, this system is still limited for the damage monitoring application of power modules in industries, as it is complex and bulky.

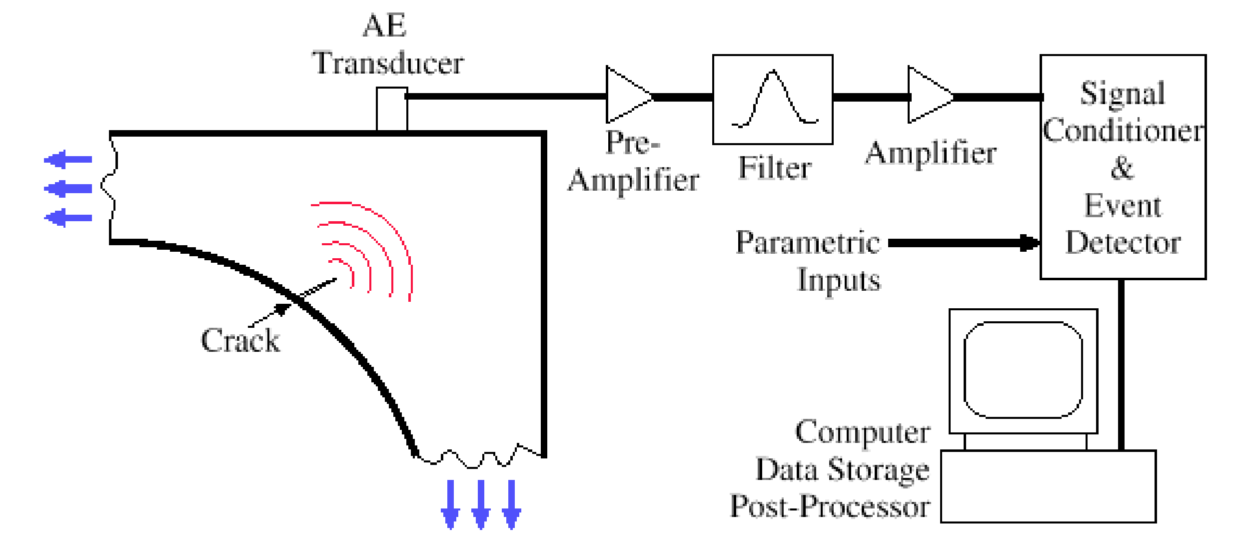

Fig. 1.4 AE signal generation, propagation, and detection [46].

1.2.3 Sources and characteristics of AE signals

The AE signals are obtained from sources that rapidly release elastic energy. Based on the source mechanism, the AE sources can be broadly classified into three types: the primary source, the secondary source, and noise [48]. The following section describes the AE source mechanism and the characteristics of AE signals arising from the sources.

The primary sources produce AE signals when materials undergo permanent changes. The AE activity resulting from permanent changes can be explained based on the Kaiser effect [49]. Significant AE activity can be observed under a certain load. However, AE activity is not observed when a material is unloaded and reloaded, until the previous maximum load is reached. This indicates that permanent deformation in materials can release energy through elastic waves. Permanent changes are represented in the form of dislocation, deformation, crack initiation, and crack propagation. Such damages usually generate AE signals in the form of a discrete transient burst, as shown in Fig. 1.5(a). Burst AE signals have different characteristics depending on the source type. In particular, the amplitude of signals can significantly vary depending on both the deformation mechanism and material properties. The factors that affect the amplitude of an AE event are listed in Table 1.3 [50]. In secondary source mechanism, the AE signals are a result of frictional rubbing and bubbling, which accompany damages such as leaks and corrosion. These signals are commonly characterized by low amplitude and long duration as shown in Fig. 1.5(b).

Noise is defined as an elastic wave generated from a source that is not related to the purpose of AE monitoring. The noise cancelling technique for eliminating the signals arising from the noise sources is explained in section 1.3.4.

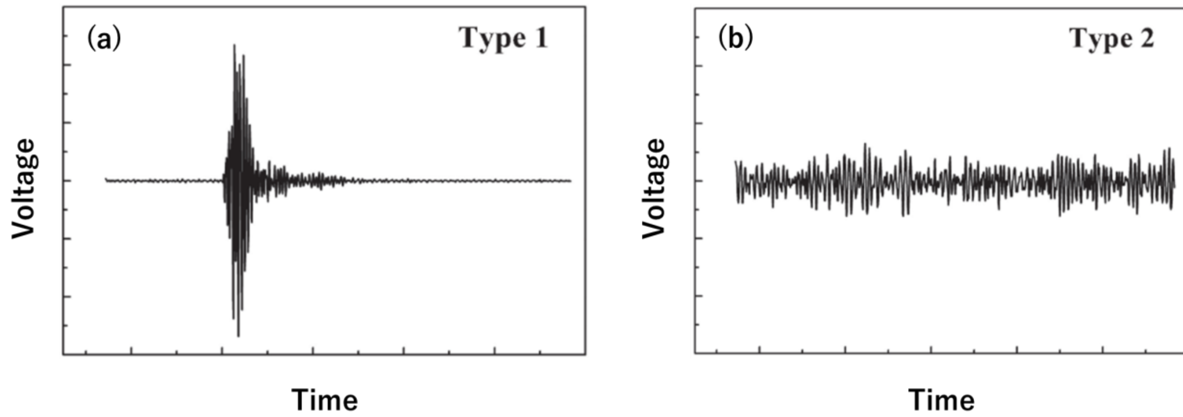

Fig. 1.5 Burst and continuous AE signals [41].

Table 1.3 Factors Affecting AE Response [50].

Factors that increase the AE amplitude	Factors that decrease the AE amplitude
High strength	Low strength
High strain rate	Low strain rate
Low temperature	High temperature
Anisotropy	Isotropy
Non-homogeneity	Homogeneity
Thick sections	Thin sections
Brittle failure (cleavage)	Ductile fracture (shear)
Crack propagation	Plastic deformation
Large grain size	Small grain size

1.2.4 AE system configuration

The acoustic emission system consists of three parts: sensors for detecting the elastic waves, a preamp for amplifying the collected low-level signals, and a signal processing board for characterization and noise cancellation of the signals.

In general, elastic waves arising from these sources have frequencies from several kHz to 1 MHz. Elastic waves are detected by the AE sensor, which is usually fabricated using piezoelectric elements. Further, they are converted into electrical signals. Since the sensing characteristics of the sensors vary depending on the material of the piezoelectric element and its internal structure, it is important to use appropriate sensors considering the target damage event. Two types of AE sensors are used: broadband and narrowband (wideband) sensors. This division is based on the detectable frequency range of the elastic wave. The resonant sensor is used to collect the AE signals at certain frequencies with high sensitivity. However, the sensitivity characteristics of a particular frequency domain can also result in waveform deformation. Broadband sensors have sensitivity in a wide frequency band. They are used for waveform and frequency analysis without waveform deformation.

A preamplifier increases the sensitivity of the AE signals in the form of electrical signals (voltage-time curve), as shown in Fig. 1.5, compared to noise. The unit used for AE signals is μV, which can be expressed in decibels (dB). This is calculated using the logarithmic equation (1.1) based on the minimum perceived amplitude (V_0) of 1 μV (0 dB).

$$\mathrm{dB} = 20\log\frac{V}{V_0} \quad (1.1) \qquad (1.1)$$

The AE signals are analyzed in the final signal processing board, which is described in section 1.2.5.

1.2.5 AE signal characteristics and noise cancelling process

The characteristics of the AE signals can be used to evaluate material damage since these signals have an abundant amount of damage information. Fig. 1.6 shows an example of a signal waveform in time domain and the characteristic parameters extracted from the signal. The point at which the sound pressure is highest is defined as the peak and the sound pressure at this point is called amplitude. In particular, a signal is recorded when its amplitude is greater than or equal to the threshold value (i.e., threshold), which is the criterion for an effective signal. The recorded signal is called a hit. The number of times that a hit signal waveform exceeds the threshold is termed as counts. Counts and amplitude indicate the number and degree of damage, respectively, and are most often used as parameters for acoustic emission assessment. In addition, the length of time for which a sound pressure exceeds the threshold and stays above it is termed as duration.

Additionally, the frequency-domain characteristics of the AE signals can be analyzed using a fast Fourier transform (FFT) algorithm. Ideally, it is used to determine the AE source with the time-domain characteristics and to eliminate noise. In general, AE sources emit elastic waves with broadband frequencies ranging from 10 kHz to 1 MHz [51]. However, for common AE signals in metallic materials, the frequencies range from 100 kHz to 500 MHz [50]. The AE events arising from non-detrimental sources such as hydraulics and bearing movement are regarded as “background AE” or “noise”. These noise often occur at low frequencies (< 100 kHz) due to the nature of the source. Table 1.4 lists the frequency ranges of noise arising from various sources in nature and vehicle. The frequency for most of the noises ranges from several Hz to 100 kHz.

The noise cancelling method is performed in the following sequence: Firstly, the noise source is identified and fundamentally eliminated. Secondly, it should be noted that noise has a

lower level of amplitude compared to that of damage. Thus, when it is difficult to eliminate the noise sources, the noise is collected and noise amplitude is analyzed. Based on the amplitude of the collected noise, a reference voltage (i.e., threshold) is set. The signals are recorded when the amplitude of the signals exceeds this threshold. Thirdly, frequency range of the collected noise is analyzed. Noise can be filtered by using an analog high-pass filter (HPF) and low-pass filter (LPF) in a signal processing board. The filtering frequency value is set based on the frequency range database of the collected noise. The de-nosing process is most important in AE monitoring, as it can lead to major errors during accurate assessment of material damage.

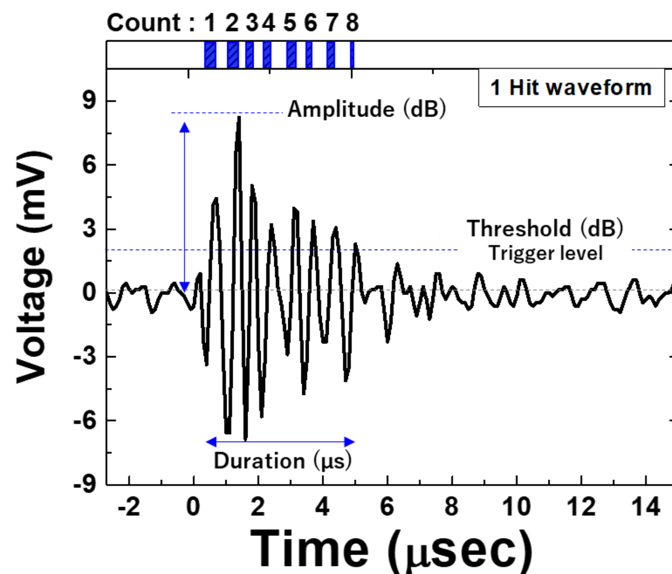

Fig. 1.6 Illustration of commonly used AE parameters [41].

Table 1.4 Typical frequency range of noise in common industries.

Source	Frequency range (Hz)
Suspension and wheels	5–10
Engine	11–17
Electric motor	50–80
Human motion	0–40
Human voice	100–9500
Music	30–12000

1.3 Objective and outline of the thesis

As mentioned in the previous sections, WBG power modules have demonstrated excellent potential toward achieving high efficiency and high power density performance for high-temperature operations. To ensure the reliability of WBG power modules at such high temperatures, the thermal degradation mechanism of high-temperature package materials such as sintered micro-porous Ag and DBA/AMB substrates must be understood. Therefore, this thesis focused on the study on the thermal degradation mechanism of package materials for high-temperature power modules. In addition, the real-time monitoring method for analyzing thermal damages in power modules was studied using the AE technique.

In Chapter 1, a brief description of the background of power electronics and emerging issues associated with the use of WBG semiconductors is introduced. The current candidates for high-temperature package materials and their reliability issues are also introduced. The current understanding on AE monitoring is also briefly discussed.

In Chapter 2, the thermal aging mechanism of sintered micro-porous Ag, which is a promising high-temperature joint material, is explored. The tensile strength and electrical resistivity of sintered Ag are evaluated during the thermal exposure at 250 °C. In addition, the changes in the grain and porous structure of sintered Ag are quantitatively characterized. Thermal aging mechanisms in sintered micro-porous Ag are discussed on the basis of the relationship between microstructural variations and mechanical/electrical properties.

In Chapter 3, the thermal shock damage mechanisms of DBA/AMB substrates with three types of ceramic plates and two types of Ni metallization are studied. The thermal shock resistance of DBA/AMB substrates is evaluated according to various material combinations. The mechanism of fractures, which are attributed to the Al creep deformation in DBA substrates, in Ni and Ni–P plating layers are discussed.

In Chapter 4, an attempt was made to monitor the fatigue damage occurring in the Al ribbon interconnection of discrete SiC Schottky barrier diode devices for the first time. The electrical switching noise signals are eliminated by a noise-cancelling process. During the power cycling test, AE signals were successfully collected. In addition, AE counts, which represent one of the time-domain parameters of AE signals, increased with the number of power cycles while fatigue cracks propagated in the Al ribbon. The AE count rate was significantly correlated with crack growth rate. On the basis of the relationship between AE activities and fatigue crack propagation, it is discussed that AE monitoring can be used for not only for understanding the fatigue propagation in Al ribbons but also monitoring the failure of power electronic devices.

In Chapter 5, a summary of the failure mechanisms in high-temperature power modules was presented. In addition, a real-time AE monitoring method was proposed as a novel monitoring technique for next-generation power modules.

Reference

[1] X. She, A. Q. Huang, and B. Ozpineci, “Review of silicon carbide power devices and their applications,” IEEE Trans. Ind. Electron., vol. 64, no. 10, pp. 8193–8205, 2017.

[2] J. Millan, P. Godignon, X. Perpina, A. Perez-Tomas, and J. Rebollo, “A survey of wide bandgap power semiconductor devices,” IEEE Trans. Power Electron., vol. 29, no. 5, pp. 2155–2163, 2014.

[3] J. Biela, M. Schweizer, S. Waffler, and J. W. Kolar, “SiC versus Si - evaluation of potentials for performance improvement of inverter and DCDC converter systems by SiC power semiconductors,” IEEE Trans. Ind. Electron., vol. 58, no. 7, pp. 2872–2882, 2011.

[4] M. Bhatnagar and B. J. Baliga, “Comparison of 6H-SiC, 3C-SiC, and Si for power devices,” IEEE Trans. Electron Devices, vol. 40, no. 3, pp. 645–655, 1993.

[5] C. Buttay, D. Planson, B. Allard, D. Bergogne, P. Bevilacqua, C. Joubert, M. Lazar, C. Martin, H. Morel, D. Tournier, et al., “State of the art of high temperature power electronics,” Mater. Sci. Eng. B Solid-State Mater. Adv. Technol., vol. 176, no. 4, pp. 283–288, 2011.

[6] T. P. Chow, “High-voltage SiC and GaN power devices,” Microelectron. Eng., vol. 83, no. 1 SPEC. ISS., pp. 112–122, 2006.

[7] C. K. Chung, Y. J. Chen, W. M. Chen, and C. R. Kao, “Origin and evolution of voids in electroless Ni during soldering reaction,” Acta Mater., vol. 60, no. 11, pp. 4586–4593, 2012.

[8] S. Hazra, A. De, L. Cheng, J. Palmour, M. Schupbach, B. A. Hull, S. Allen, and S. Bhattacharya, “High switching performance of 1700-V, 50-A SiC power MOSFET over Si IGBT/BiMOSFET for advanced power conversion applications,” IEEE Trans. Power Electron., vol. 31, no. 7, pp. 4742–4754, 2016.

[9] M. R. Werner and W. R. Fahrner, “Review on materials, microsensors, systems, and devices for high-temperature and harsh-environment applications,” IEEE Trans. Ind. Electron., vol. 48, no. 2, pp. 249–257, 2001.

[10] P. Diaz Reigosa, H. Luo, and F. Iannuzzo Ge, “Implications of ageing through power cycling on the short circuit robustness of 1.2-kV SiC MOSFETs,” IEEE Trans. Power Electron., vol. 8993, no. c, pp. 1–1, 2019.

[11] P. Ning, R. Lai, D. Huff, F. Wang, K. Ngo, V. Immanuel, and K. Karimi, “SiC Wirebond Multichip Phase-Leg Module Packaging Design and Testing for Harsh Environment,” IEEE Trans. Power Electron., vol. 25, no. 1, pp. 16–23, 2010.

[12] B. J. Watson and G. Castro, “High-temperature electronics pose design and reliability challenges,” Analog Dialogue, vol. 46, no. 2, pp. 1–7, 2012.

[13] D. Spry1, P. Neudeck, L. Chen, G. Beheim, R. Okojie, C. Chang, R. Meredith, T. Ferrier, and L. Evans, “Fabrication and testing of 6H-SiC JFETs for prolonged 500 °C operation in air ambient,” Mater. Sci. Forum, vol. 600–603, pp. 1079–1082, 2009.

[14] P. G. Neudeck, R. S. Okojie, and L. Y. Chen, “High-temperature electronics - A role for wide bandgap semiconductors?,” Proc. IEEE, vol. 90, no. 6, pp. 1065–1076, 2002.

[15] C. Choe, C. Chen, S. Noh, K. Suganuma, “Thermal shock performance of DBA/AMB substrates plated by Ni and Ni–P layers for high-temperature applications of power device modules,” Materials, vol. 11, pp. 2394-1-13, 2018

[16] K. Suganuma, S. Sakamoto, N. Kagami, D. Wakuda, K. S. Kim, and M. Nogi, “Low-temperature low-pressure die attach with hybrid silver particle paste,” Microelectron. Reliab., vol. 52, no. 2, pp. 375–380, 2012.

[17] S. Kraft, A. Schletz, and M. März, “Reliability of silver sintering on DBC and DBA substrates for power electronic applications,” Integr. Power Electron. Syst. (CIPS), 2012 7th Int. Conf., no. December 2015, pp. 1–6, 2012.

[18] S. Noh, C. Choe, C. Chen, H. Zhang, and K. Suganuma, “Printed wire interconnection using Ag sinter paste for wide band gap power semiconductors,” J. Mater. Sci. Mater. Electron., vol. 29, no. 17, pp. 15223–15232, 2018.

[19] H. Zhang, S. Nagao, K. Suganuma, H. J. Albrecht, and K. Wilke, “Thermostable Ag die-attach structure for high-temperature power devices,” J. Mater. Sci. Mater. Electron., vol. 27, no. 2, pp. 1337–1344, 2016.

[20] C. Chen, C. Choe, D. Kim, Z. Zhang, and K. Suganuma, “Low-stress design of bonding structure and its thermal shock performance (− 50 to 250 °C) in SiC/DBC power die-attached modules,” J. Mater. Sci. Mater. Electron., vol. 29, no. 16, pp. 14335–14346, 2018.

[21] U. M. Choi, F. Blaabjerg, and S. Jørgensen, “Power cycling test methods for reliability assessment of power device modules in respect to temperature dtress,” IEEE Trans. Power Electron., vol. 33, no. 3, pp. 2531–2551, 2018.

[22] A. Lahyani, P. Venet, G. Grellet, and P. J. Viverge, “Failure prediction of electrolytic capacitors during operation of a switchmode power supply,” IEEE Trans. Power Electron., vol. 13, no. 6, pp. 1199–1207, 1998.

[23] H. Huang and P. A. Mawby, “A lifetime estimation technique for voltage source inverters,” IEEE Trans. Power Electron., vol. 28, no. 8, pp. 4113–4119, 2013.

[24] N. Patil, J. Celaya, D. Das, K. Goebel, and M. Pecht, “Precursor parameter identification for insulated gate bipolar transistor (IGBT) prognostics,” IEEE Trans. Reliab., vol. 58, no. 2, pp. 271–276, 2009.

[25] M. Held, P. Jacob, G. Nicoletti, P. Scacco, and M.-. Poech, “Fast power cycling test of IGBT modules in traction application,” in Proceedings of Second International Conference on Power Electronics and Drive Systems, 1997, vol. 1, pp. 425–430 vol.1.

[26] L. Zhou, S. Zhou, and M. Xu, “Investigation of gate voltage oscillations in an IGBT module after partial bond wires lift-off,” Microelectron. Reliab., vol. 53, no. 2, pp. 282–287, 2013.

[27] V. Smet, F. Forest, J. J. Huselstein, A. Rashed, and F. Richardeau, “Evaluation of Vce monitoring as a real-time method to estimate aging of bond wire-IGBT modules stressed by power cycling,” IEEE Trans. Ind. Electron., vol. 60, no. 7, pp. 2760–2770, 2013.

[28] M. Tounsi, A. Oukaour, B. Tala-Ighil, H. Gualous, B. Boudart, and D. Aissani, “Characterization of high-voltage IGBT module degradations under PWM power cycling test at high ambient temperature,” Microelectron. Reliab., vol. 50, no. 9–11, pp. 1810–1814, 2010.

[29] U. M. Choi, F. Blaabjerg, and S. Jørgensen, “Study on effect of junction temperature swing duration on lifetime of transfer molded power IGBT modules,” IEEE Trans. Power Electron., vol. 32, no. 8, pp. 6434–6443, 2017.

[30] U. M. Choi, S. Jorgensen, and F. Blaabjerg, “Advanced accelerated power cycling test for reliability investigation of power device modules,” IEEE Trans. Power Electron., vol. 31, no. 12, pp. 8371–8386, 2016.

[31] D. Xiang, L. Ran, P. Tavner, A. Bryant, S. Yang, and P. Mawby, “Monitoring solder fatigue in a power module using case-above-ambient temperature rise,” IEEE Trans. Ind. Appl., vol. 47, no. 6, pp. 2578–2591, 2011.

[32] D. Xiang, L. Ran, P. Tavner, S. Yang, A. Bryant, and P. Mawby, “Condition monitoring power module solder fatigue using inverter harmonic identification,” IEEE Trans. Power Electron., vol. 27, no. 1, pp. 235–247, 2012.

[33] Y. Xiong, X. Cheng, Z. J. Shen, C. Mi, H. Wu, and V. K. Garg, "Prognostic and warning system for power-electronic modules in electric, hybrid electric, and fuel-cell vehicles," IEEE Trans. Ind. Electron., vol. 55, no. 6, pp. 2268–2276, 2008.

[34] T. F. Drouillard and F. J. Laner, "Acoustic Emission: A Bibliography With Abstracts," Springer US, 1979.

[35] U. S. A. Drouillard, Thomas F. "Acoustic emission: The first half century," EG&G Rocky Flats, Inc., Golden, Colorado 80402, 1994.

[36] F. Förster and E. Scheil, "Acoustical study of formation of martensite needles," Naturwissenschaften, vol. 28, no. 9, pp. 245–247, 1936.

[37] M. Eaton, "Acoustic Emission (AE) monitoring of buckling and failure in carbon fibre composite structures," Cardiff University, 2007.

[38] S. K. J. Al-jumaili, "Damage assessment In complex structures using acoustic emission.," Cardiff University, 2016.

[39] M. F. Carlos, "Overview of current and developing ASTM acoustic emission (AE) standards," J. Acoust. Emiss., vol. 28, pp. 229–233, 2010.

[40] S. Katsuaki, O. Taira, K. Mitsue, and S. Masahiko, "Acoustic emission from ceramic/metal joints on cooling," Am. Ceram. Soc. Bull., vol. 65, no. 7, pp. 1060–1064, 1986.

[41] C.-Y. Choe, W.-S. Jung, and J.-W. Byeon, "Damage evaluation in lithium cobalt oxide/carbon electrodes of secondary battery by acoustic emission monitoring," Mater. Trans., vol. 56, no. 2, pp. 269–273, 2015.

[42] K. Rhodes, N. Dudney, E. Lara-Curzio, and C. Daniela, "Understanding the degradation of silicon electrodes for lithium-ion batteries using acoustic emission," J. Electrochem. Soc., vol. 157, no. 2, pp. A1354–A1360, 2010.

[43] C. Villevieille, M. Boinet, and L. Monconduit, “Direct evidence of morphological changes in conversion type electrodes in Li-ion battery by acoustic emission,” Electrochemistry Communications, vol. 12, no. 10. pp. 1336–1339, 2010.

[44] S. Levikari, T. J. Karkkainen, C. Andersson, J. Tamminen, and P. Silventoinen, “Acoustic phenomena in damaged ceramic capacitors,” IEEE Trans. Ind. Electron., vol. 65, no. 1, pp. 570–577, 2018.

[45] B. Legros, P. X. Thivel, Y. Bultel, M. Boinet, and R. P. Nogueira, “Acoustic emission: Towards a real-time diagnosis technique for Proton exchange membrane fuel cell operation,” J. Power Sources, vol. 195, no. 24, pp. 8124–8133, 2010.

[46] A. Watanabe, M. Tsukuda, and I. Omura, “Real time degradation monitoring system for high power IGBT module under power cycling test,” Microelectron. Reliab., vol. 53, no. 9–11, pp. 1692–1696, 2013.

[47] H. Miinshiou, J. Liang, K. L. Peter, R. B. Charlie, S. Rodger, and L. K. Dwaine, “Using acoustic emission in fatigue and fracture materials research,” ournal Eng. Mater., vol. 50, no. 11, pp. 1–14, 1988.

[48] J. R. Naumann, “Acoustic emission monitoring of small wind turbine blades,” The University of Sheffie, 2014.

[49] Knud G. Bøving, “Non-destructive examination methods for condition monitoring: Acoustic emission,” Butterworth-Heinemann, pp. 17–23, Jan. 1989.

[50] R. K. Miller and P. McIntire, “Acoustic emission testing, volume 5 of nondestructive testing handbook”, 2nd editio. American Society of Nondestructive Testing, 1987.

[51] P. T. Cole, “NDT Part 7. Acoustic emission,” The British Institute of Non-Destructive Testing, 1988.

Chapter 2

Thermal degradation mechanism of micro-porous silver die-attach

2.1 Introduction

To address high performance challenges of power modules, Si devices have been replaced with wide band-gap (WBG) semiconductors including silicon carbide (SiC) and gallium nitride (GaN), which allow power modules to be operated at high power densities and high temperatures above 250 ºC [1][2]. Normally, power modules are manufactured by bonding semiconductors on power substrates with interconnect materials. However, the existing conventional solders are not suitable for WBG interconnect materials due to their poor reliability at high temperatures [3]. To ensure high temperature operation of WBG semiconductors, numerous joint materials with high melting points, excellent thermal and electrical properties such as silver, gold and copper have been proposed.

Silver (Ag) sinter pastes have been considered as promising joint materials due to various advantages such as high bonding strength, low resistivity and excellent thermal reliability, compared with Au-Sn solder and nano copper sinter paste, all of which can be used at higher temperature (>250 °C) [4][5]. Additionally, low-cost micron- and submicron-sized Ag pastes have been developed in recent [6] compared to high-cost nano Ag sinter paste, enlarging the possibility of Ag sinter paste in the power industries. However, a large amount of thermal stress induced by the mismatch in coefficients of thermal expansion (CTE) causes various microstructural changes and properties deterioration in sintered Ag joints during long-term high temperature exposure.

The mechanism of properties deterioration and microstructural changes in sintered Ag joints have been investigated under high temperature exposure [7][8]. Grain growth, pore coarsening, increasing porosity of sintered Ag joints in a die-attach have been studied as the mechanism of strength decreases [9][10][11]. However, the strength decreases of a die-attachment structure can be affected by degradation of sintered Ag joints as well as the other

components including chips, metallization and substrates. For this reason, it is difficult to certainly understand relationship between strength decreases, and observed microstructure changes. Moreover, changes in grain and pore structure were also related with electrical properties which is another most important properties for joint materials. However, the effect of thermal exposure on electrical properties were not reported. Therefore, it is important to investigate relationship between mechanical/electrical properties deterioration and microstructure variation during high temperature exposure by using sintered Ag specimens, in order to eliminate other component effect and understand the relationship.

In this work, the effect of thermal exposure on mechanical and electrical properties and microstructural changes on sintered porous Ag during thermal exposure was demonstrated. The tensile strength and electrical resistivity of sintered Ag were evaluated. Changes in grains and porous structure of sintered Ag were quantitatively characterized. This relationship between microstructural variations and mechanical and electrical properties were discussed.

2.2 Experimental

2.2.1 Fabrication of sintered porous Ag specimens

Two types of Ag particles with different sizes and shapes were mixed to be a "Hyblid paste". Ag flakes have an average lateral length of 5 μm and thickness of 260 nm (Fukuda metal Co.). The others are Ag spherical particles with an average diameter of 400 nm (Mitsuimining and smelting Co.) [6]. The Ag paste was made by mixing them and ethylene glycol (EG) at a weight ratio of 5:5:1 to control paste viscosity. Fig. 2.1 (a-c) show the manufacturing process of Ag specimens for tensile strength and electrical resistivity measurements. First, Cu plates were sprayed with boron nitride lubricant to prevent bonding between Ag paste and Cu plates during a sintering process (Fig. 2.1 (a)). Ag paste was printed in the shape of a test specimen by using screen mask on the pre-treated Cu plates as shown in Fig. 2.1 (b). Afterwards, the Ag paste was sintered at 250 °C for one hour without pressure on the hot plate as shown in Fig. 2.1 (c). After sintering, Ag specimens were easily detached from Cu plates. The width and thickness of the sintered Ag specimens were 5 mm and 0.5 mm, respectively. The micro-porous structure of sintered Ag specimens was confirmed by SEM observation, as shown in Fig. 2.1 (d).

2.2.2 Characterization of mechanical/electrical properties

To characterize changes in sintered Ag during thermal exposure, Ag specimens were exposed at 250 °C for different exposure times of 0, 50, 200, 500, and 1000 hours in air. To evaluate the deterioration of mechanical and electrical properties, tensile tests and electrical resistivity measurements were conducted on the aged Ag specimens, as shown in Fig. 2.2 (a) and (b), respectively. Tensile strength was tested by a universal testing machine (Tytron 250, MTS Co.) at a strain rate of 1.0×10^{-5}/s. Electrical resistivity was measured by a four probe test with span distance of 5 mm. Source currents were supplied from 500 mA to 1,000 mA.

2.2.3 Microstructural observation

To observe microstructural changes, Ag grains and porous structure of the aged Ag specimens were evaluated. The cross-section of each Ag specimen being aged for different thermal exposure times was prepared by ion-milling. The Ag grain size and number was characterized by electron backscatter diffraction (EBSD). EBSD data for aged Ag specimens was collected using a step size of 0.1 μm. The porous structure including pore size, number and porosity was observed by a field emission scanning electron microscope (FE-SEM) as shown in Fig. 2.1 (d). To automatically distinguish between sintered Ag and pores, the observed SEM images were processed into black and white by using image-processing software (IPWin) as shown in Fig. 2.3. The sintered Ag and pore area were transformed to black and white, respectively. Afterwards, pore size, number and porosity were measured. The average area of a pore was used as pore size. To evaluate fracture mode, fracture surface was observed by FE-SEM after tensile test.

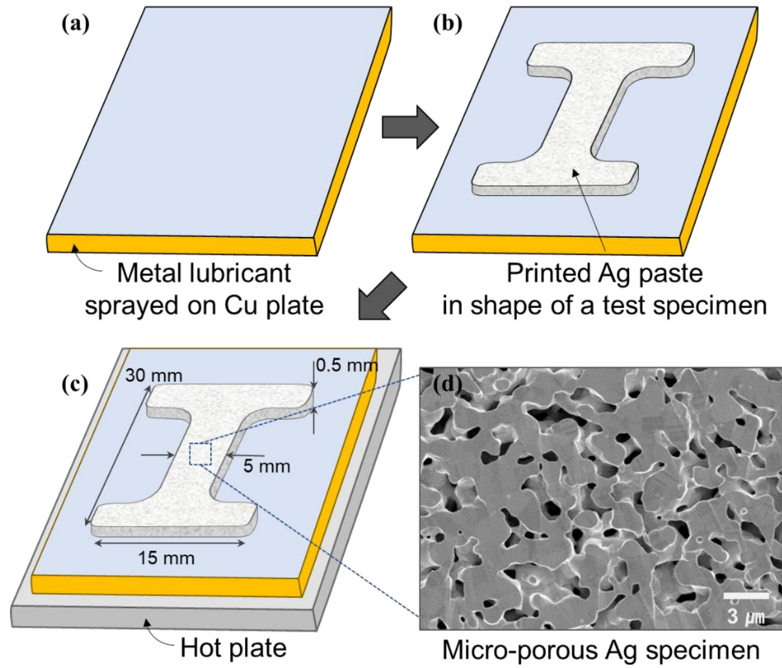

Fig. 2.1 Fabrication process of Ag specimens for tensile and four probe tests (a-c) and its micro-porous structure observed by SEM (d).

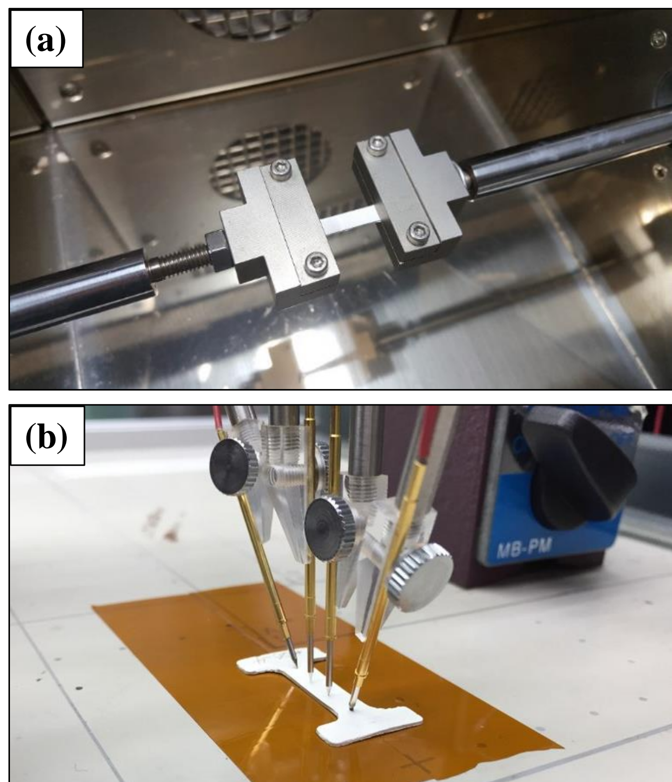

Fig. 2.2 Configuration of a tensile test (a) and four probe resistivity measurement (b) for sintered Ag specimens.

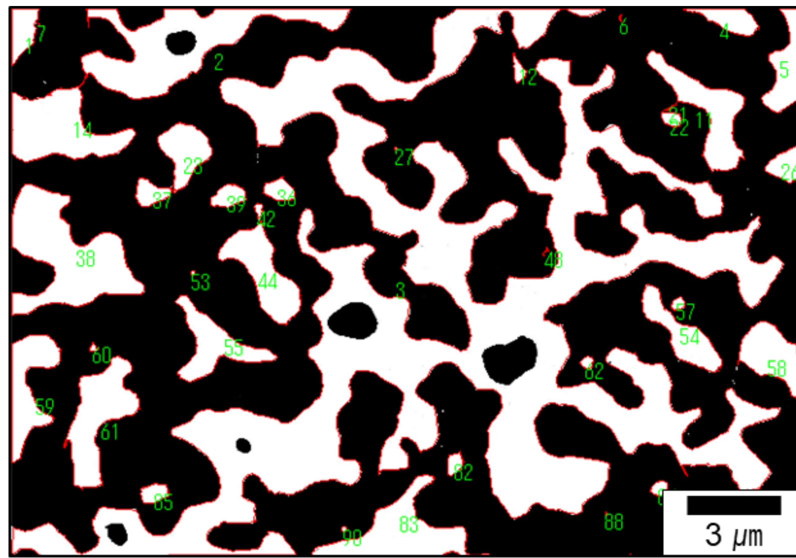

Fig. 2.3 Automatic measurement of pore area and number of sintered Ag.

2.3 Results and discussion

2.3.1 Deterioration of tensile strength and electrical resistivity

Fig. 2.4 shows changes in tensile strength and electrical resistivity under high temperature exposure. Initial porous Ag has a tensile strength of 42 MPa and an electrical resistivity of 8.5 $\times 10^{-6}$ Ωcm after being sintered at 250 °C for 1 hour. The tensile strength was altered during thermal exposure time. According to the strength change trends, the change in the tensile strength was divided into three distinct stages. Tensile strength gradually decreased during thermal exposure time up to 200 hours. However, the reduced strength of aged Ag almost fully returned to its initial value during thermal exposure time from 200 hours to 500 hours. The recovered strength was maintained for up to 1000 hours of thermal exposure time. On the other hand, the electrical resistivity of sintered Ag did not change during the first 200 hours of thermal exposure, but significantly decreased from 200 to 500 hours and kept the reduced resistivity. This change trendency of both strength and resistivity occurs in the same exposure time of 200 and 500 hours. To investigate the reason of properties change, microstructure after each exposure time was observed.

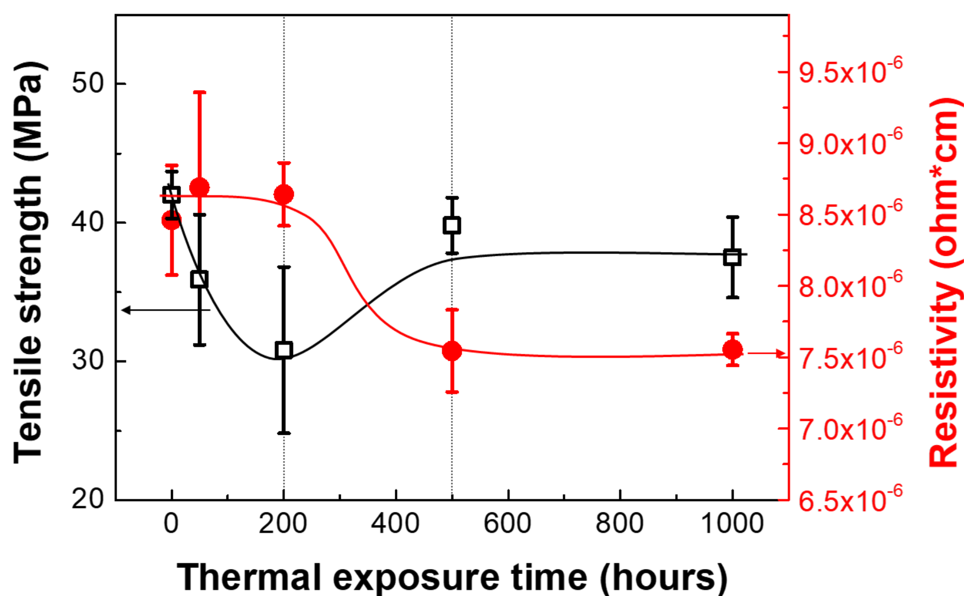

Fig. 2.4 Deterioration of tensile strength and resistivity of sintered Ag during thermal exposure.

2.3.2 Changes in Ag grains and porous structure

Fig. 2.5 shows grains of sintered Ag at different thermal exposure times. Pores were indicated in white areas. At the initial state, sintered Ag had numerous fine Ag grains as shown in Fig. 2.5 (a). After thermal exposure, the Ag grains became bigger and fewer. To quantitatively evaluate microstructure changes including Ag grains and pores, their size and number were measured and the results are shown in Fig. 2.6 and Fig. 2.7, respectively.

Fig. 2.6 quantitatively shows the changes in grain size and number of sintered Ag in thermal exposure. The average Ag grain size increased with thermal exposure time up to 500 hours, while the grain number decreased. The Ag grain growth indicated an exponential increase, and its trend was similar with that of general fine-grained materials. Fig. 2.7 shows the changes in pore average area and number of sintered Ag during thermal exposure time. The average area of pores was used to represent pore size. The pore number at different thermal

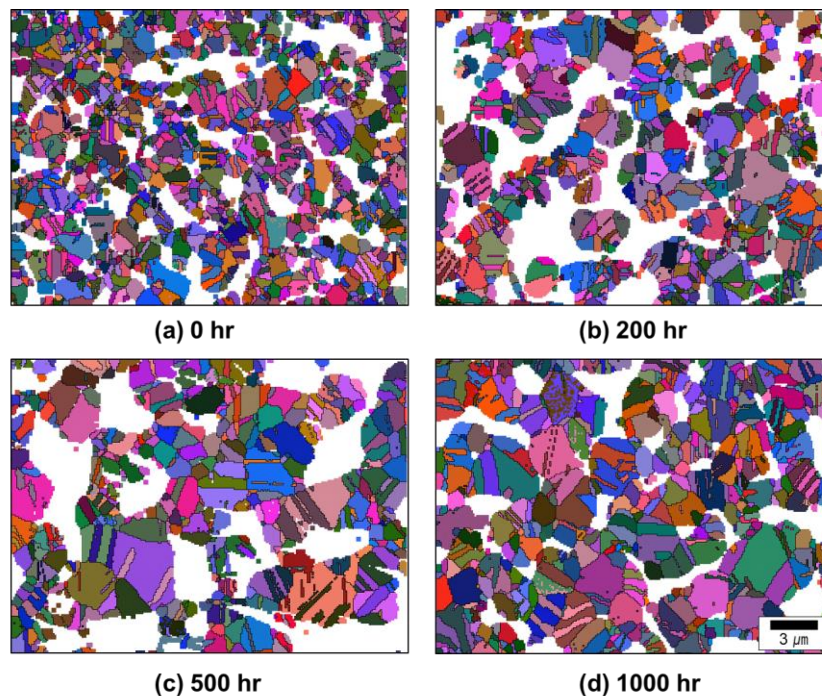

Fig. 2.5 EBSD observation of Ag specimens after different exposure times; (a) 0 h, (b) 200 h, (c) 500 h and (d) 1,000 h.

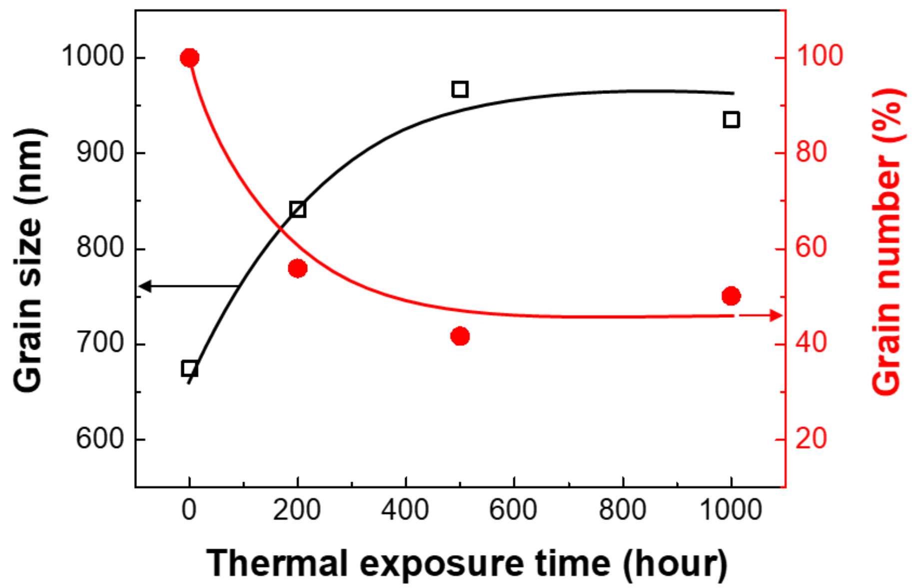

Fig. 2.6 Variation in Ag grain size and number with thermal exposure time.

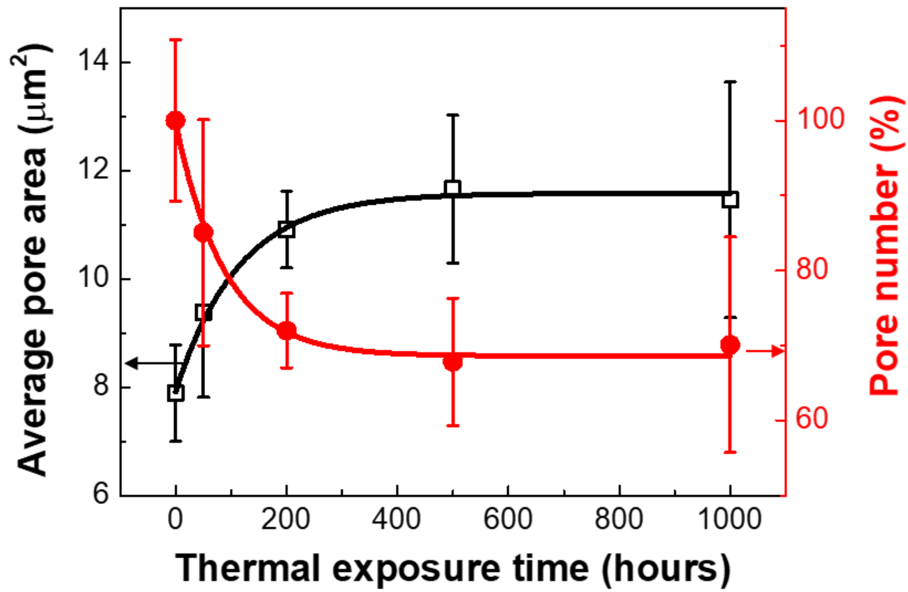

Fig. 2.7 Variation in average pore area and number with thermal exposure time.

exposure time was automatically counted in 17μm x 25 μm area, and it was expressed in percentiles based on the initial pore number. This pore size increased with increasing thermal exposure time, while the pore number decreased. Although the most pore coarsening occured before 200 hours, pore coarsening with pore number reduction occurred until 500 hours.

Fig. 2.8 shows the change in porosity of sintered Ag during thermal exposure time. Porosity was measured by calculating the ratio of pore area to observed area of 425 μm^2 [12]. The porosity of sintered Ag that was exposed for 0, 200, 500 and 1000 hours was 38 %, 37 %. 29 % and 31 %, respectively. The porosity of sintered Ag decreased with exposure time up to the first 500 hours. In the whole of thermal exposure period, most of the porosity reduction of sintered Ag occurred from 200 hours to 500 hours of thermal exposure time.

Grain growth, pore coarsening and porosity reductions occurred in thermal exposure. Among them, the size of grain and pore simultaneously increased with thermal exposure time. When polycrystalline materials are exposed to high temperature, grain size grows to reduce the interface energy of numerous grain boundaries through the migration of these grain boundaries [13]. During this grain growth process, pores also simultaneously migrate along with the migration of grain boundaries, resulting in pore coarsening [14]. This driving force to reduce the surface energy promotes Ag grain growth as well as pore coarsening. As a result, Ag grain growth and pore coarsening seems to occur at the same time.

On the other hand, the most porosity reduction in sintered Ag occurred in the thermal exposure period from 200 to 500 hours. Such silver porosity reduction was observed in sintered Ag joints [8]. The porosity in sintered Ag joins decreased with thermal exposure time, especially from 100 to 500 hours, which is similar with that observed in bare sintered Ag from 200 to 500 hours. When sintered Ag is exposed to high temperatures, its porosity reduction is generated by a driving force to reduce surface energy [15]. The driving force is the same with those of grain

growth and pore coarsening. The porosity reduction in sintered Ag seems to be related with grain growth and pore coarsening.

The grain growth, pore coarsening and porosity reduction occurred between exposure times of 200 and 500 hours, similarly with deterioration trends in mechanical/electrical properties as shown in Fig. 2.4.

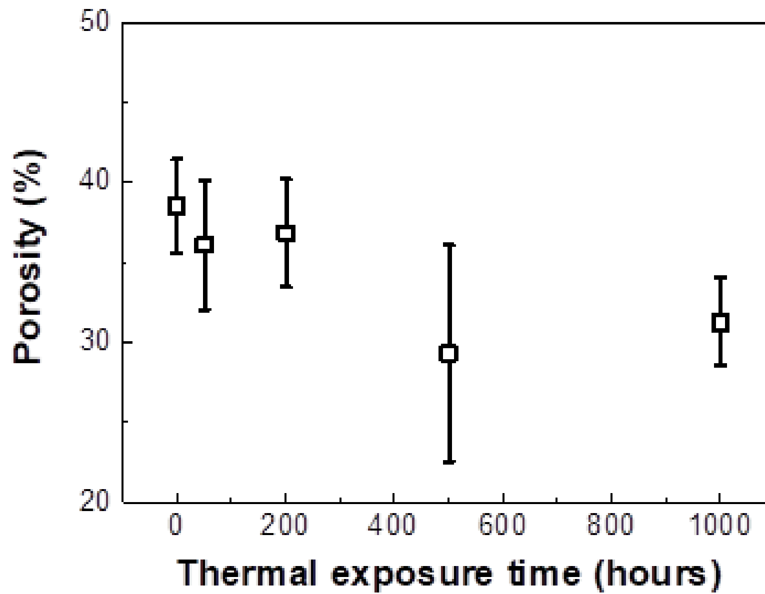

Fig. 2.8 Variation in porosity of sintered Ag with thermal exposure time.

2.3.3 Relationship between mechanical/electrical properties and microstructural variation

The tensile strength gradually decreased up to 200 hours of thermal exposure time. The grain growth and pore coarsening remarkably occurred during this thermal exposure period, which well known as the mechanism of strength decreases in polycrystalline porous materials. Normally, the grain growth with grain number reduction generally leads to strength decreases due to an decrease in the Hall–Petch strengthening effect of grain boundaries [16]. In addition, pore coasening in sintered Ag also can contributed to tensile strength deterioration, because it can offer the site for stress concentration and crack generation. Thus, strength deterioration was caused by grain size and pore size growth during thermal exposure by 200 hours.

On the other hand, the decreased strength of sintered Ag recovered from 200 to 500 hours. In this period, porosity was remarkably reduced from 36 % to 29 %. The decreasing porosity indicates the reduction of total pore volume which will lead to a strength increase. It was reported that the tensile strength of porous Ag will be influenced by the microstructure and is inversely proportional to the porosity of porous Ag [10]. Thus, the porosity reduction in sintered Ag from 200 to 500 hours seems to results in the strength recovery occurring for the same period. After 500 hours, tensile strength as well as microstructure did not altered.

Although in the previous studies, a relationship between the porosity reduction and shear strength was reported in the sintered Ag joining structure [8], it is difficult to eliminate the interference of other factors such as metallization oxidation and substrate roughening. In this study, based on the confirmed relationship between tensile strength and porosity of bare sintered Ag, it was considered that the reported shear strength recovering phenomenon [7][17]in Ag joints also was caused by the porosity reduction of sintered Ag joints in a die-attachment.

Electrical resistivity was not changed in the early exposure period before 200 hours, while the grain size growth and pore coarsening significantly occurred in the same period. Grain size growth and pore coarsening did not significantly affect electrical resistivity. On the other hand, the electrical resistivity of sintered Ag was significantly decreased from 200 to 500 hours. Most of the porosity reduction of sintered Ag occurred in the same period. Thus, porosity and resistivity have a proportional relationship. It is supported by previous study[18]. In metal foams, relative electrical resistivity decreased in a non-linear way with relative density. Although various microstructural factors such as porosity, pore size, pore shape, and grain size can affect the electrical resistivity in porous material systems [19-21], porosity more sensitively influences electrical resistivity [20-22]. In this chapter, the porosity reduction in sintered Ag also was a dominant microstructural change for electrical resistivity decreases, compared to grain growth and pore coarsening.

2.3.4 Evaluation of fracture surface

Fig. 2.9 shows the tensile fracture surfaces of sintered Ag that was exposed for different thermal exposure time. The fracture surface at an initial state indicated a brittle fracture pattern without apparent plastic deformation. However, small dimple patterns appeared after thermal aging of 50 hours. Dimple size increased up to 200 hours. The grain size and pore size increased up to 200 hours as in section 2.3.2. The fracture mode changes from brittle fracture to ductile fracture. Normally, a dimple fracture pattern presents ductile fracture due to plastic deformation than brittle fracture. This fracture strength decrease after a thermal exposure time up to 200 hours reflects on the fracture mode.

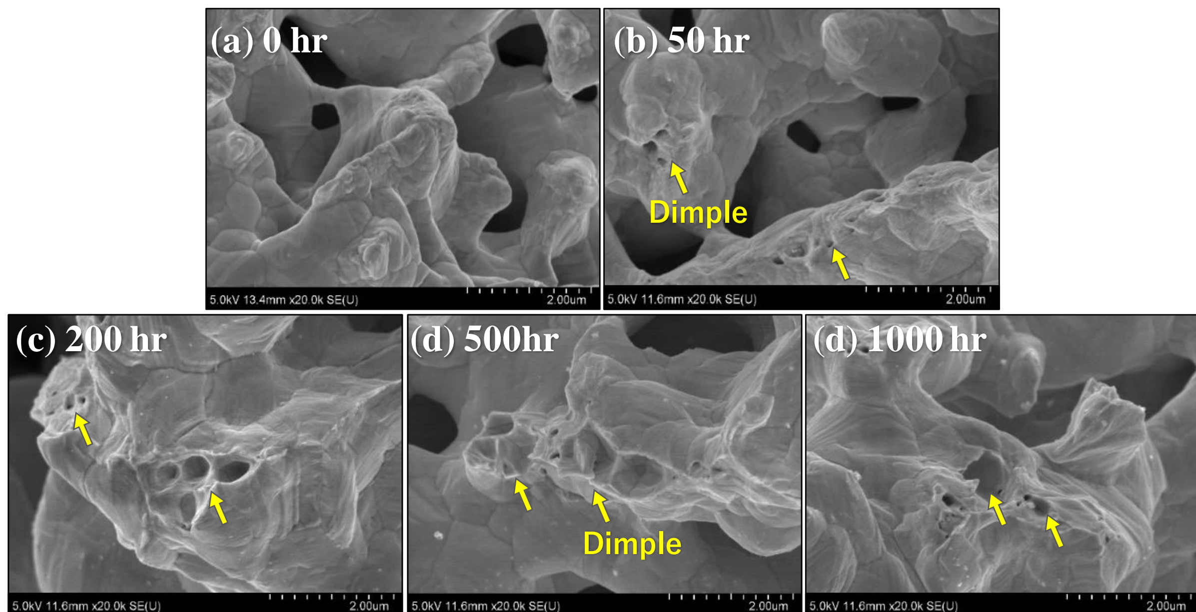

Fig. 2.9 SEM observations of the fracture surface of Ag specimens aged for different exposure times; (a) 0 h, (b) 50 h, (c) 200 h, (d) 500 h and (d) 1000 h.

2.4 Conclusion

In this chapter, thermal aging effects on tensile strength, electrical resistivity and microstructural changes in sintered porous Ag were investigated at 250 °C during different duration of 0, 50, 200, 500, and 1000 hours. The relationship between microstructural changes and mechanical/electrical properties was discussed.

1. Tensile strength and electrical resistivity of sintered Ag was varified with thermal exposure time. Strength processed via three steps including deterioration, recovering, and maintaining during the thermal exposure. Electrical resistivity decreased in the middle of the thermal exposure period.
2. Accompanied with the decreasing number of Ag grains and pores, the size of the Ag grains and pores was increased with with thermal exposure time. Grain growth and pore coarsening occurred until 500 hours. On the other hand, porosity mostly reduced from 200 to 500 hours.
3. The decreasing tensile strength results from Ag grain growth and porous coarsening which is well-known as a strength deterioration mechanism. On the other hand, the decreased strength recovered by the porosity reduction during the long-time thermal exposure from 200 to 500 hours.
4. Electrical resistivity decreased with exposure time especially from 200 to 500 hours. It was dominantly affected by porosity reduction that occurred in the same period.

Reference

[1] K. Suganuma, J.M. Song, Y.S. Lai, "Power electronics packaging", Microelectron. Reliab., vol. 55, pp. 2523, 2015.

[2] S.H. Ryu, B.A. Hull, S. Dhar, L. Cheng, Q.C.J. Zhang, J. Richmond, M.K. Das, A.K. Agarwal, J.W. Palmour, A.J. Lelis, "Performance, reliability, and robustness of 4H-SiC power DMOSFETs", Mater. Sci. Forum., vol. 645, pp. 69–974, 2010.

[3] S. Menon, E. George, M. Osterman, M. Pecht, "High lead solder (over 85 %) solder in the electronics industry: RoHS exemptions and alternatives", J. Mater. Sci. Mater. Electron., vol. 26, pp. 4021–4030, 2015.

[4] K.S. Siow, "Mechanical properties of nano-silver joints as die attach materials", J. Alloys Compd., vol. 514, pp. 6–19, 2012.

[5] V.R.V.R. Manikam, K.Y.K.Y.K.Y. Cheong, "Die attach materials for high Temperature applications: A review", Components, Packag. Manuf. Technol. IEEE Trans., vol. 1 , pp. 457–478, 2011.

[6] K. Suganuma, S. Sakamoto, N. Kagami, D. Wakuda, K.S. Kim, M. Nogi, "Low-temperature low-pressure die attach with hybrid silver particle paste", Microelectron. Reliab., vol. 52, pp. 375–380, 2012.

[7] H. Zhang, S. Nagao, K. Suganuma, H.J. Albrecht, K. Wilke, "Thermostable Ag die-attach structure for high-temperature power devices", J. Mater. Sci. Mater. Electron., vol. 27, pp. 1337–1344, 2016.

[8] S.A. Paknejad, G. Dumas, G. West, G. Lewis, S.H. Mannan, "Microstructure evolution during 300 °C storage of sintered Ag nanoparticles on Ag and Au substrates", J. Alloys Compd., vol. 617, pp. 994–1001, 2014.

[9] Y. Akada, H. Tatsumi, T. Yamaguchi, A. Hirose, T. Morita, E. Ide, "Interfacial bonding

mechanism using silver metallo-organic nanoparticles to bulk metals and observation of sintering behavior”, Mater. Trans., vol. 49, pp. 1537–1545, 2008.

[10] V. Caccuri, X. Milhet, P. Gadaud, D. Bertheau, M. Gerland, “Mechanical properties of sintered Ag as a new material for die bonding: Influence of the density”, J. Electron. Mater., vol. 43, pp. 4510–4514, 2014.

[11] J. Carr, X. Milhet, P. Gadaud, S.A.E. Boyer, G.E. Thompson, P. Lee, “Quantitative characterization of porosity and determination of elastic modulus for sintered micro-silver joints”, J. Mater. Process. Technol., vol. 225, pp. 19–23, 2015.

[12] L.Q.N. Tran, T.N. Minh, C.A. Fuentes, T.T. Chi, A.W. Van Vuure, I. Verpoest, “Investigation of microstructure and tensile properties of porous natural coir fibre for use in composite materials”, Ind. Crops Prod., vol. 65, pp. 437–445, 2015.

[13] W.D. Kingery, B. Francois, “Grain growth in porous compacts”, J. Am. Ceram. Soc., vol. 48, pp. 546–547, 1965.

[14] H. Li, S. Dey, R.H.R. Castro, “Kinetics and thermodynamics of densification and grain growth: Insights from lanthanum doped zirconia”, Acta Mater., vol. 150, pp. 394–402, 2018.

[15] J.D. Osorio, D. Maya, A.C. Barrios, A. Lopera, F. Jiménez, J.M. Meza, J.P. Hernández-Ortiz, A. Toro, “Correlations between microstructure and mechanical properties of air plasma-sprayed thermal barrier coatings exposed to a high temperature”, J. Am. Ceram. Soc., vol. 96, pp. 3901–3907, 2013.

[16] T. Kizuka, H. Ichinose, Y. Ishida, “Structure and hardness of nanocrystalline silver”, J. Mater. Sci., vol. 2, pp. 1501–1507, 1997.

[17] H. Zhang, S. Nagao, K. Suganuma, “Addition of SiC particles to Ag die-attach paste to improve high-temperature stability; Grain growth kinetics of sintered porous Ag”, J.

Electron. Mater., vol. 44, pp. 3896–3903, 2015.

[18] M. F. Ashby, A. G. Evans, N. A. Fleck, L. J. Gibson, J. W. Hutchinson, and H. N. G. Wadley, "Metal Foams: Chapter 14 - Electrical properties of metal foams," Butterworth-Heinemann, pp. 189-193, 2000.

[19] K.M. Mannan, K.R. Karim, "Grain boundary contribution to the electrical conductivity of polycrystalline Cu films", J. Phys. F Met. Phys., vol. 5, pp. 1687–1693. 1975.

[20] M. Hakamada, T. Kuromura, Y. Chen, H. Kusuda, M. Mabuchi, "Influence of porosity and pore size on electrical resistivity of porous aluminum produced by spacer method", Mater. Trans., vol. 48, pp. 32–36, 2007.

[21] J.M. Montes, F.G. Cuevas, J. Cintas, "Porosity effect on the electrical conductivity of sintered powder compacts", Appl. Phys. A Mater. Sci. Process., vol. 92, pp. 375–380, 2008.

[22] T. SUN, L. DONG, C. WANG, W. GUO, L. WANG, T. LIANG, "Effect of porosity on the electrical resistivity of carbon materials", New Carbon Mater., vol. 28, pp. 349–354, 2013.

Chapter 3

Thermal shock damage mechanism of DBA/AMB substrates plated with Ni and with Ni–P layers

3.1 Introduction

Power electronic modules, such as converter and inverter systems, have been widely used in transportation, including electric vehicles, aircraft, and high-speed railroads. Usually, the power module simply consists of five main components: wires, semiconductor devices, joints, substrates, and heat sink. With the increasing use of wide-bandgap (WBG) semiconductor devices, such as silicon carbide (SiC) and gallium nitride (GaN), which provide great opportunities to develop power electronic systems with increased power densities, high reliability in extreme environments, and higher integration, the development of high-temperature-operating power devices allows for the use of power electronic modules at high temperatures (>250 °C) [1,2]. In this case, large thermal stress occurs in the power electronic module due to coefficients of thermal expansion (CTE) mismatch in multiple layers, leading to a reliability issue for its high-temperature application.

To dissipate much heat that causes power electronic module failure, a power electronic substrate plays an important role. A power electronic substrate is located between a semiconductor die and heat sink and transfers heat generated in semiconductors to cooling plates [3–5]. Direct bonded aluminum (DBA) and active metal brazing (AMB) substrates have been considered as the most promising ceramic substrates for power electronic modules due to their good thermal conductivity, low electrical resistance, and high insulation voltage [6,7]. The advantage comes from the metal/ceramic/metal sandwich structure of DBA/AMB substrates. DBA/AMB basically has a ceramic insulator plate composed of materials such as Al_2O_3, AlN, and Si_3N_4. Both sides of an insulator plate are metalized by aluminum (Al) or copper (Cu) to function as a thermal and electrical conductor layer [8]. Such a metal layer enables not only improved thermal conductivity but also creates electrical circuits on an insulator plate.

However, the sandwich structure of DBA/AMB substrates also results in a large amount of thermomechanical stress induced by the difference in CTEs between metal and ceramic in the sandwich structure in changing temperatures [5,9–11]. Repeated thermomechanical stress finally induces the total fracture of DBA/AMB substrates [12]. Thermomechanical stress in DBA/AMB substrates at high temperatures depends on the material properties of ceramic and metal components. In addition, Ni metallization, fabricated by two principally different process techniques—the electroplated Ni plating and electroless Ni–P plating—is most generally plated on the surface of DBA/AMB substrates as a metallization layer to protect the oxidation of Cu and Al. Additionally, electroplated Ni and electroless-plated Ni–P also have different mechanical properties. Electroplated Ni has good ductility and high tensile strength [13,14], while electroless Ni–P has good hardness and a simple manufacturing process because of its chemical reduction process without any need of electric connection [15–22].

The thermal shock performance of the DBA/AMB substrates as well as the Ni metallization layer determines the whole lifespan of the power electronic module [9,21,22]. Therefore, the material design of DBA/AMB substrates became an important issue, since it determines their thermal cycling reliability of power electronic modules. However, thermal cycling reliability of Ni-plated DBA/AMB substrates with various ceramics has been rarely studied.

In this chapter, a thermal shock cycling test of DBA/AMB substrates with various ceramics plated with Ni and Ni–P layers was carried out to investigate their high-temperature reliability for a WBG power electronic module. The cracking and roughening of Ni–P layer on DBA/AMB substrates were evaluated by field-emission scanning electron microscopy (FE-SEM), scanning acoustic tomography (SAT), and laser profile microscopy. The fracture suppression mechanism in a Ni layer on DBA/AMB substrates was also examined with the aid of a stress analysis by finite element method (FEM) simulation.

3.2 Materials and methods

In this work, DBA and AMB substrates were supplied from Mitsubishi Materials Co., Japan. Table 3.1 shows all the material combinations of DBA/AMB substrates, such as substrate types and plated layers. The dimensions of the ceramics of Al_2O_3, AlN, and Si_3N_4 were 32 × 32 × 0.65 mm and the dimensions of the Al and Cu metal were 30 × 30 × 0.31 mm, which was bonded on both sides of a ceramic plate. Ni metallization layer on DBA/AMB substrates was conducted by electro and electroless plating methods. The electroplated Ni film was deposited at the current density of 2 A/cm^2. Ni–P electroless deposition was plated at 85 °C for pH 6.4. It was confirmed that the Ni–P plating layer contained 1 wt% phosphorus. Two different metallization times were respectively adjusted to achieve an average thickness of around 7 µm. Fig. 3.1a shows the image of the DBA substrate coated with a Ni–P layer with electroless plating. The dimensions and structure of the DBA/AMB substrate coated with a Ni metallization layer are shown in Fig. 3.1b. Fig. 3.1c,d show the SEM image of the surface of the Ni metallization layer by electro and electroless plating, respectively. The electroplated Ni layer had a pyramid-like crystal morphology, which is generally observed [23]. On the other hand, the Ni–P electroless plating layer had a smoother surface than the Ni electroplating layer. Fig. 3.1e,f show the microstructure of Al and Cu with a few hundred micrometer-sized grains in the DBA and AMB substrates, respectively. Two samples per material combination were fabricated to check the experiment's reproducibility.

To evaluate the high-temperature reliability of the DBA/AMB substrates with Ni electroplating and Ni–P electroless plating layers, a thermal shock cycling test between −50 °C and 250 °C was performed up to 1000 cycles by using a thermal shock chamber (TSE-110-A-S, ESPEC Corp., Japan). The dwelling time at the upper and lower temperatures was 30 min.

Table 3.1 Materials and dimensions of multilayered specimens.

Substrates			Metallization (Thickness: 7 µm)
Type	**Metal (30 × 30 × 0.31 mm)**	**Ceramic (32 × 32 × 0.65 mm)**	
DBA	Al	Al_2O_3	Ni electroplating or Ni–P electroless plating
		AlN	Ni electroplating or Ni–P electroless plating
		Si_3N_4	Ni electroplating or Ni–P electroless plating
AMB	Cu	Al_2O_3	Ni electroplating or Ni–P electroless plating
		AlN	Ni electroplating or Ni–P electroless plating
		Si_3N_4	Ni electroplating or Ni–P electroless plating

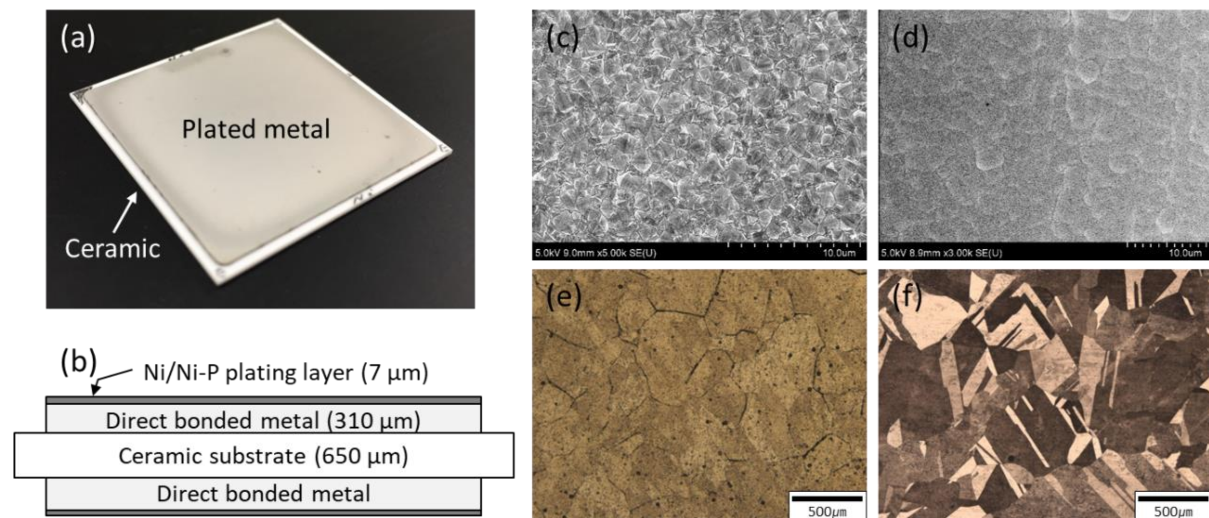

Fig. 3.1 (a) Macrograph of a typical substrate specimen, (b) cross-section diagrams of the DBA/AMB substrates plated by Ni and Ni–P layers, surface morphology of Ni (c) and Ni–P (d) layer on the substrates, and surface microstructure of Al (e) and Cu (f) of the DBA/AMB substrates.

Regarding to the industry standards for the harsh environmental testing of microelectronics [24,25], the temperature range of a thermal shock test is set between low temperatures of −50 °C to −40 °C and high temperatures of 125 °C to 150 °C. However, advanced SiC power electronic modules are generally expected to be used at a temperature up to 250 °C. For this reason, the upper temperature of 250 °C was chosen for this study. In addition, two samples per type were tested after 100 cycles.

To characterize fracture in the metallization and substrates during thermal shock cycling test, the thermally aged specimens were taken out at 0, 50, 100, 200, 600, and 1000 cycles. The surface change of the electro and electroless plating layers was analyzed by FE-SEM (SU8020, HITACHI, Tokyo, Japan) and SAT (FineSAT FS300, HITACHI, Japan). The surface roughness of the plated specimens was measured using laser profile microscopy (VK-9510, Keyence Corp., Osaka, Japan). In order to investigate the failure mechanism, the cross-section of the aged plating layer was prepared by focused ion beam (FIB, FIB-2100, HITACHI, Japan) milling and observed using FE-SEM.

To understand thermal stress distribution, stress distribution in Ni- and Ni–P-plated DBA/AMB substrates at a high temperature of 250 °C during a thermal shock cycling test was investigated by a two-dimensional FEM simulation. The model was fabricated by commercial FEM code (ANSYS 15.0). Al and Cu metals in DBA/AMB substrates were considered as a polycrystalline face centered cubic structure consisting of hypothetical grains of (111), (110), and (001) orientation. Fig. 3.2 representatively shows the FEM model of a Ni-plated AMB substrate with Si_3N_4 ceramic, where the Cu metal consisted of Cu (111), Cu (110), and Cu (001) orientations. In this simulation, the angular point of the model was fixed in the X, Y directions. The stress-free temperature for the model was assumed to be 25 °C. FEM was used for elastic–plastic deformation analysis. Because there was no additional stress in this model, it was

considered that the FEM analysis exhibited a plane stress state. The properties of the materials used for this model of plated DBA/AMB substrates are summarized in Table 3.2.

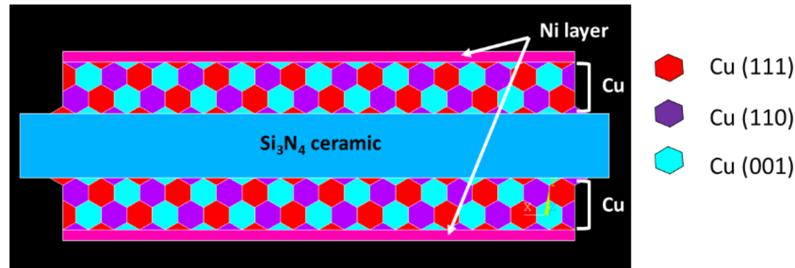

Fig. 3.2 FEM model for thermal stress distribution simulation of an AMB substrate with Si_3N_4.

Table 3.2 Mechanical and thermal properties of the various materials in Ni- and Ni–P-plated DBA/AMB substrates.

Materials	**Young's modulus (GPa)**	**Poisson's ratio**	**Coefficient of linear thermal expansion (μm·m^{-1}·K^{-1})**	**Yield strength (GPa)**	**Tensile strength (MPa)**	**Fracture toughness (MPa·m$^{1/2}$)**
Cu (001) [27,28]	75.7	0.28	17.7	0.7	-	
Cu (110) [27,28]	101.8	0.3	17.7	0.93	-	
Cu (111) [27,28]	123.4	0.3	17.7	1.2	-	
Al (001) [29]	63.7	0.34	21.3	0.59	-	
Al (110) [29]	72.59	0.34	21.3	0.52	-	
Al (111) [29]	76.1	0.34	21.3	0.51	-	
Al_2O_3	280	0.23	7.9	-	-	4
AlN	320	0.24	4.6	-	-	3
Si_3N_4	290	0.27	2.9	-	-	7
Ni [30, 31]	220	0.31	14.1	0.08	500–1000	53
Ni–P [30, 30-32]	50	0.31	13.0	0.23	50–150	1.1–2.1

3.3 Results and discussion

3.3.1 Thermal shock behavior

3.1.1.1 Active metal brazing (AMB)

Fig. 3.3 shows Ni- and Ni–P-plated AMB substrates with Al_2O_3 and AlN ceramic after 10 cycles and those with Si_3N_4 ceramic after 1000 cycles. AMB substrates with Al_2O_3 and AlN ceramic fractured regardless of the type of metallization. The fracture of Al_2O_3 and AlN ceramic of AMB substrates occurred along vertical and horizontal directions, as shown in Fig. 3.3g. The horizontal fracture occurred inside the Al_2O_3 and AlN ceramic, while the interface delamination was never observed. On the other hand, AMB substrates with Si_3N_4 survived until 1000 cycles, regardless of the metallization type. Although Si_3N_4 ceramic has the biggest CTE mismatch with Cu among three types of ceramic, as shown in Table 3.2, the superior thermal cycling lifetime of the Si_3N_4 substrate was confirmed, which agrees with a report in a recent study [26]. This is due to Si_3N_4 having a larger fracture toughness of 7 $MPa \cdot m^{1/2}$, which provides the ability of a material to resist crack initiation and extension leading to fracture, while the other ceramics does not. Among three types of AMB substrates, AMB substrates with Si_3N_4 showed the best thermal shock resistance.

Fig. 3.4 shows SEM images of the surface of the Ni electroplating and Ni–P electroless plating layers on AMB substrates with Si_3N_4 at the initial state and after 1000 cycles. A thin cracks were observed in the Ni–P electroless plating layer, as shown in Fig. 3.4d, which was not visible through visual inspection, see Fig. 3.3f, while a crack did not occur in the Ni electroplating layer after 1000 cycles. Crack generation and propagation of the Ni–P layer on the AMB substrates with Si_3N_4 were investigated by SAT observation. Fig. 3.5 shows SAT surface images of the Ni–P layer on AMB substrates with Si_3N_4 during a thermal shock cycle test up to 1000 cycles. The dark area in the SAT surface images indicates surface defects such

as cracks, voids, and roughening, which were made by the diffused reflection of the acoustic wave at the surface defect. It is difficult to definitively distinguish cracking from roughening but SAT image clearly indicates that the surface defects gradually increased with thermal shock cycles.

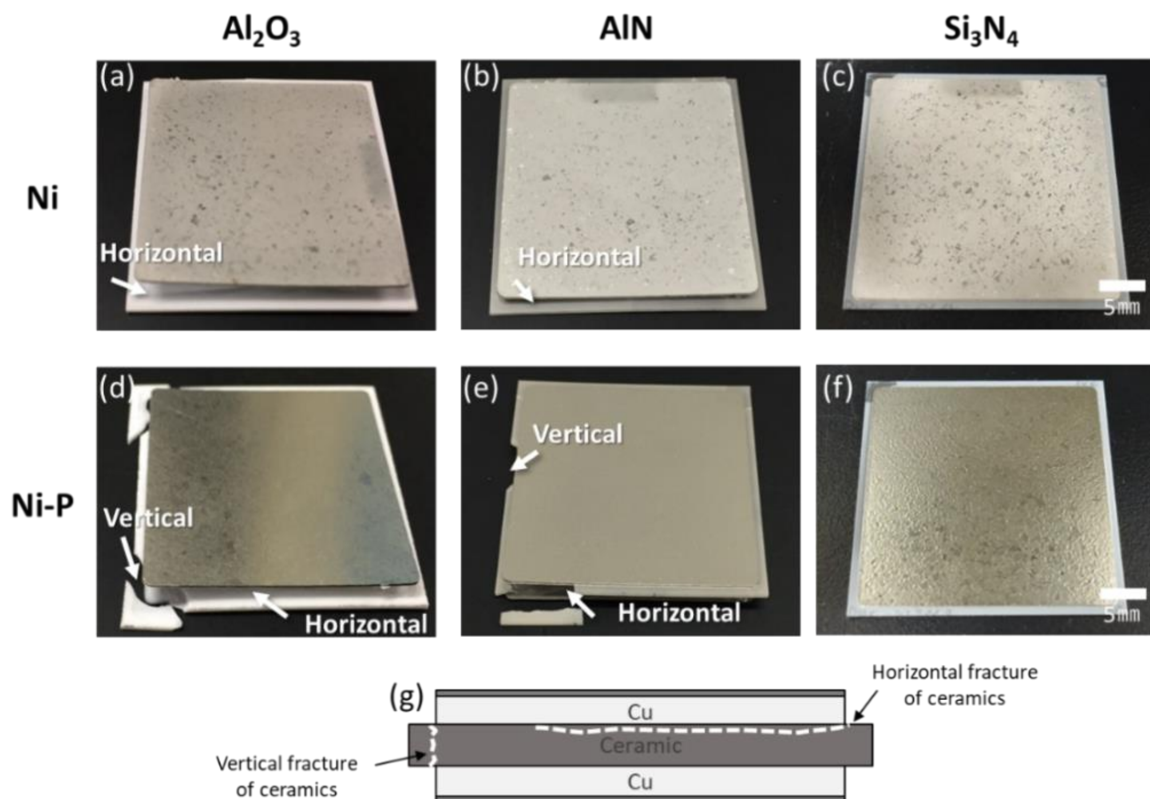

Fig. 3.3 Destructed AMB substrates with Al_2O_3 (a, d) and AlN (b, e) after 10 cycles, nondestructed AMB substrates with Si_3N_4 (c, f) after 1000 cycles plated with Ni (a-c) and Ni–P (d-f), and (g) fracture pattern of AMB substrates.

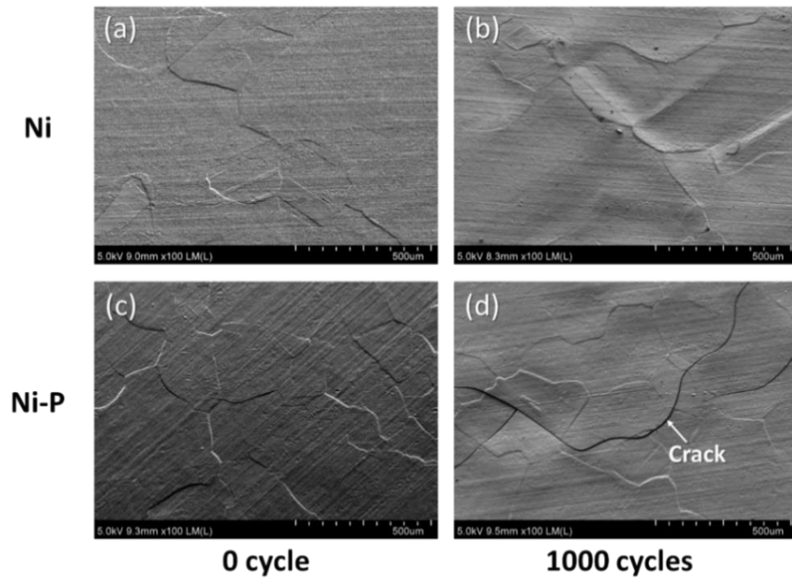

Fig. 3.4 Surface variation of Ni (a,b) and Ni–P (c,d) layers on AMB substrates with Si_3N_4 before and after 1000 cycles.

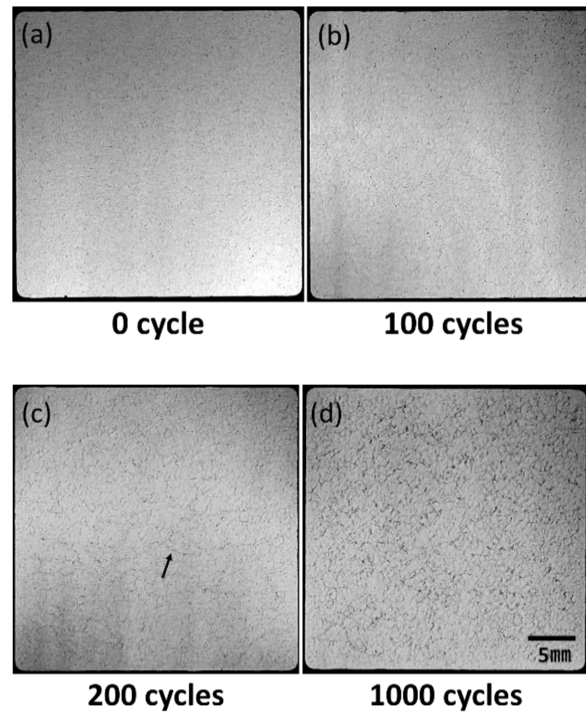

Fig. 3.5 Scanning acoustic tomography (SAT) observation of the surface morphology of the Ni–P layer on AMB substrates with Si_3N_4 after different thermal shock tests: 0, 50, 100, and 1000 cycles.

3.1.1.2 Direct bonded aluminum (DBA)

All DBA substrates survived until 1000 cycles, regardless of ceramic material used, as shown in Fig. 3.6. Three types of ceramics in DBAs were the same as those for AMB. Unlike DBA substrates, AMB substrates with Al_2O_3 and AlN were fractured. This clearly indicates that thermal stress in the DBA with Al_2O_3 and AlN ceramics is much smaller than that of AMB. The thermal stress dependence of metal types in DBA/AMB substrates was studied by Hamilton et al. [4]. It was reported that DBA substrates have lower stress than AMB substrates due to lower yield strength of aluminum. This contributes to DBA having longer thermal shock resistivity compared to AMB in spite of the bigger CTE mismatch of aluminum in DBA.

On the other hand, the Ni–P layer on the DBA substrates severely cracked after 1000 cycles, regardless of type of ceramics, as shown in Fig. 3.6d–f, while the Ni layer retained a sound surface. Unlike AMB substrates, see Fig. 3.3d–f, cracking in Ni–P on DBA was evident even upon visual inspection. Fig. 3.7 shows the SEM images of the surface of the Ni and Ni–P layers on a DBA substrate with Si_3N_4 at the initial state and after 1000 cycles. The surface of the Ni and Ni–P layers was roughened compared to the initial state. The Ni–P layer was cracked and the crack was thicker than that of the Ni–P layer on a AMB substrate, see Fig. 3.4d. Moreover, the cracks completely opens for the Ni–P layer and even Al surface appeared in side open cracks In contrast, the electroplated Ni layer with the higher fracture toughness showed a more stable thermal shock reliability.

To investigate the Ni–P crack evolution on DBA substrates with three kinds of ceramic, SAT images were acquired. Fig. 3.8 shows the SAT surface images of the Ni–P layer on DBA substrates with Al_2O_3, AlN, and Si_3N_4 up to 1000 cycles. The Ni–P layer on all

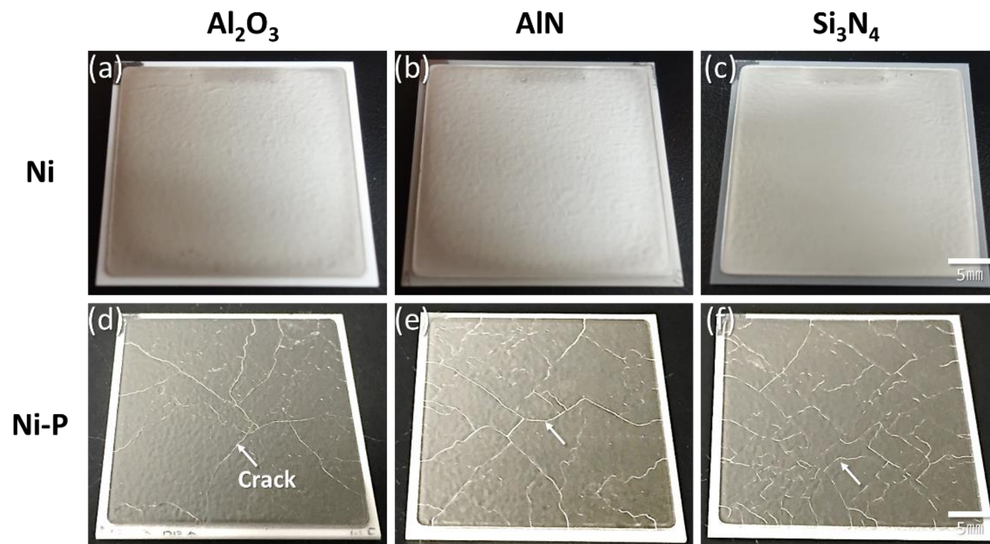

Fig. 3.6 DBA substrates with Al_2O_3, AlN, and Si_3N_4 after 1000 cycles, plated with Ni (a–c) and Ni–P (d–f).

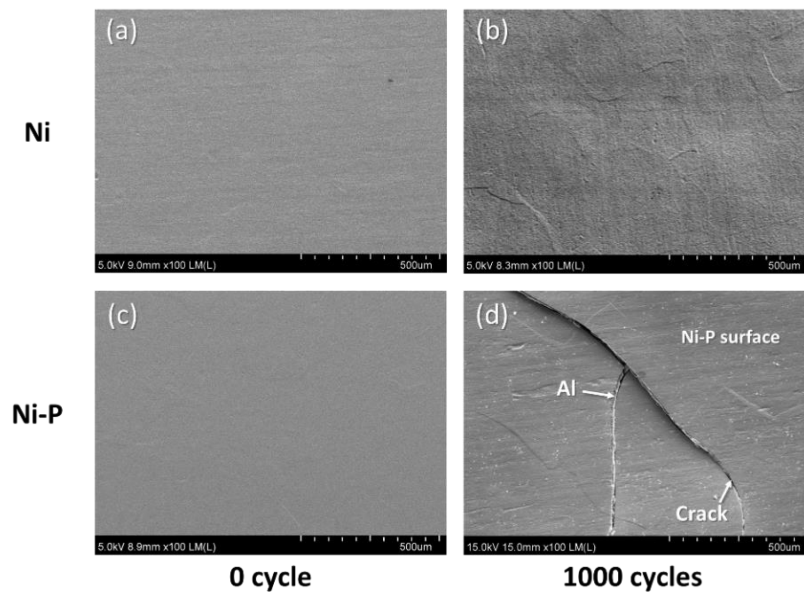

Fig. 3.7 Surface morphology of Ni (a,b) and Ni–P (c,d) layers on DBA substrates with Si_3N_4 before and after 1000 cycles.

DBA substrates cracked and roughened even after 50 cycles. The cracks propagated and new cracks appeared up to 1000 cycles. The roughening also became more remarkable after 1000 cycles. Compared to DBA substrates with AlN and Si_3N_4, cracks were fewer generated in the Ni–P layer on DBA substrates with Al_2O_3. The surface defects of the cycled specimens were analyzed by laser profile microscopy. Fig. 3.9 shows the Ni–P layer on DBA substrates with Si_3N_4 at the initial state and after 1000 cycles. The surface of the Ni–P layer at the initial state was relatively flat. After 1000 cycles, cracks occurred on the roughened surface of the Ni–P layer, as see in Fig. 3.9b,e. The depth of the cracks was about 15 – 20 μm. This means that the cracks open through the Ni–P layer of a thickness of 7 μm and they extend into the Al surface beneath. The surface roughening of the Ni–P layer, as see in Fig. 3.9c,f, was observed on the entire layer, regardless of cracks.

Using laser profile microscopy, the roughness of the Ni and Ni–P layers on the DBA/AMB substrates was evaluated during thermal shock cycling test, and the results are shown in Fig. 3.10a,b, respectively. The AMB substrates with Al_2O_3 and AlN, which fractured only after 10 cycles, were excluded from the roughness evaluation. The roughness of the Ni and Ni–P layers on the AMB substrates gradually increased. Regarding the DBA substrates, the roughness of all Ni layers increased by a few micrometers, regardless of type of ceramic plates. Ni–P layer roughness increased up to 600 cycles at different rates, and then remained nearly constant. Roughening in the Ni–P layer on a DBA substrate with Si_3N_4 ceramic was most remarkable, revealing that the Ni–P layer on DBA substrates with Si_3N_4 was most roughened among only DBA substrates. Compared to the other ceramics, Si_3N_4 has the biggest CTE mismatch with Al metal, which induces the largest stress. Based on these results, the roughening in the Ni–P layer is closely related to thermal stress.

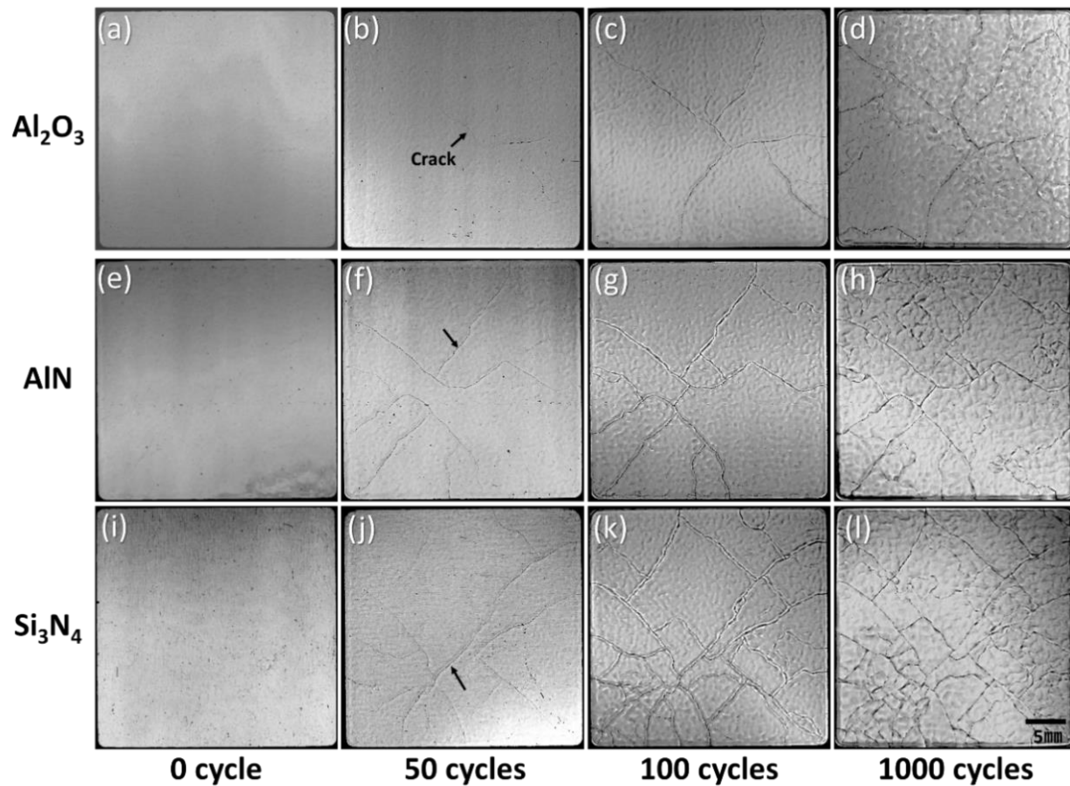

Fig. 3.8 SAT observation of the surface morphology of a Ni–P layer on DBA substrates with Al_2O_3 (a–d), AlN (e–h), and Si_3N_4 (i–l) after different thermal shock tests: 0, 50, 100, and 1000 cycles.

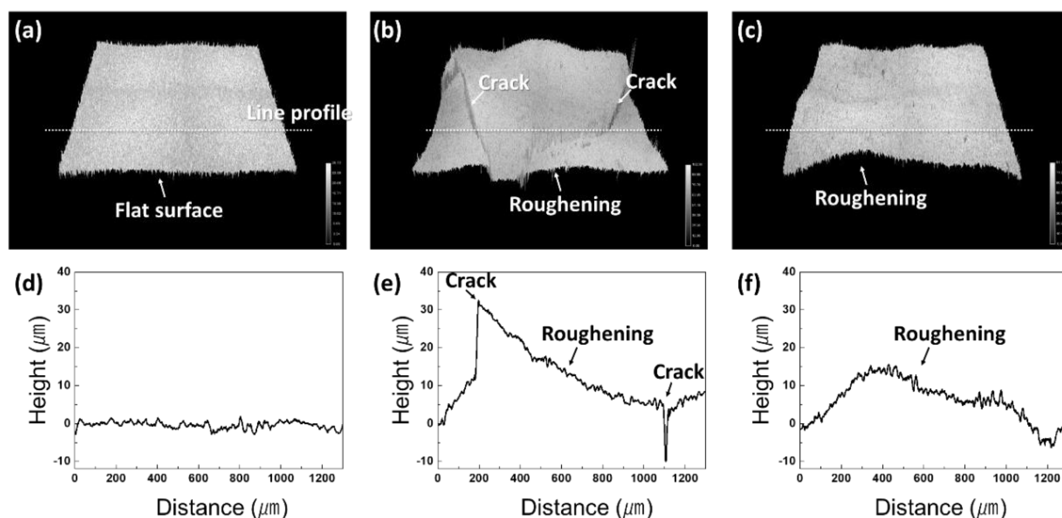

Fig. 3.9 Laser surface observation of the Ni–P layer on DBA substrates with Si_3N_4 at the initial state (a) and after 1000 cycles (b,c). Local area with cracked (b) and roughened (c) area, and its roughness profile (d–f) measured by a line profile corresponding to (a–c), respectively.

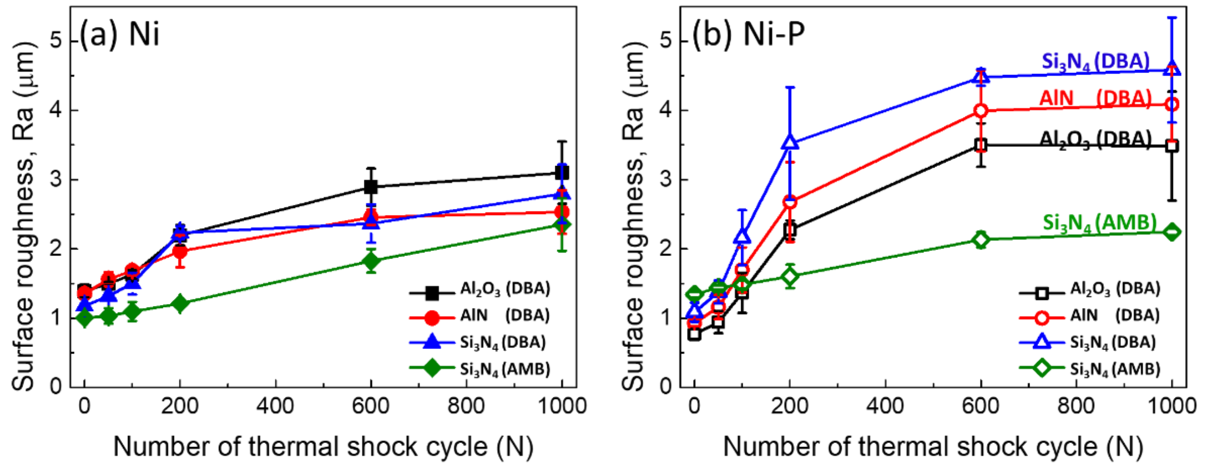

Fig. 3.10 Variation in surface roughness of Ni (a) and Ni–P (b) layers on DBA/AMB substrates with Al_2O_3, AlN, and Si_3N_4 up to 1000 cycles.

3.3.2 Cracking mechanism of Ni–P Layer

Fig. 3.11a,d show surface and cross-section images, respectively, of the Ni–P layer on DBA substrates with Si_3N_4 at the initial state. A FIB image of a cross-section was taken at an ion beam angle of 30°. The Ni–P layer was uniformly plated on a flat Al surface of the DBA substrates. Fig. 3.11e,f shows the cross section of cracks in the Ni–P layer after 100 and 1000 cycles, respectively. The flat Al face was deformed only after 100 cycles. The crack in the Ni–P layer occurred just on the deformed Al surface. Thus, the deformation of Al metal layer in DBA substrates caused cracking and roughening of the Ni–P layer. After 1000 cycles, the deformation of Al metal layer became more serious. It caused deep cracking in the Ni–P layer and even crack opening.

To confirm the reason for cracking of the Ni–P layer on DBA substrates, a bare DBA substrate with no plating layer was also observed after a thermal shock cycling test. The flat Al surface at the initial state, as shown in Fig. 3.12a, was significantly roughened after 100 cycles, see Fig. 3.12b. Al roughening occurred relating to grain boundary of Al layer. Some grains protruded from an aluminum surface after cycle tests, as shown in Fig. 3.12c. A grain boundary was always observed under the roughened surface of an Al layer, especially at the interface between the protruding grain and the nondeformed grain. Normally, grain boundary sliding (GBS) deformation of polycrystalline metal, one of the creep plastic deformation mechanisms, occurs under high temperatures and tensile/compressive stress [35]. During the thermal shock cycling test, Al metal layer on DBA was suffered from compressive and tensile stress caused by CTE mismatch between Al and ceramic.

The deformation occurring in an Al layer, see Fig. 3.12c, was considered as GBS deformation. For AMB substrates, it was also reported that copper in AMB substrates is roughened through grain boundary sliding after thermal cycling from −55 °C to 250 °C [26],

which is similar to the condition of the thermal shock test in this study. Metallic deformation can result from GBS deformation as well as simple homogeneous deformation. The observed Al GBS deformation and the referred Cu GBS deformation indicates that GBS is one of the main deformation mechanisms of the metallic layers, resulting in the cracking of the Ni–P layer on the DBA/AMB substrates.

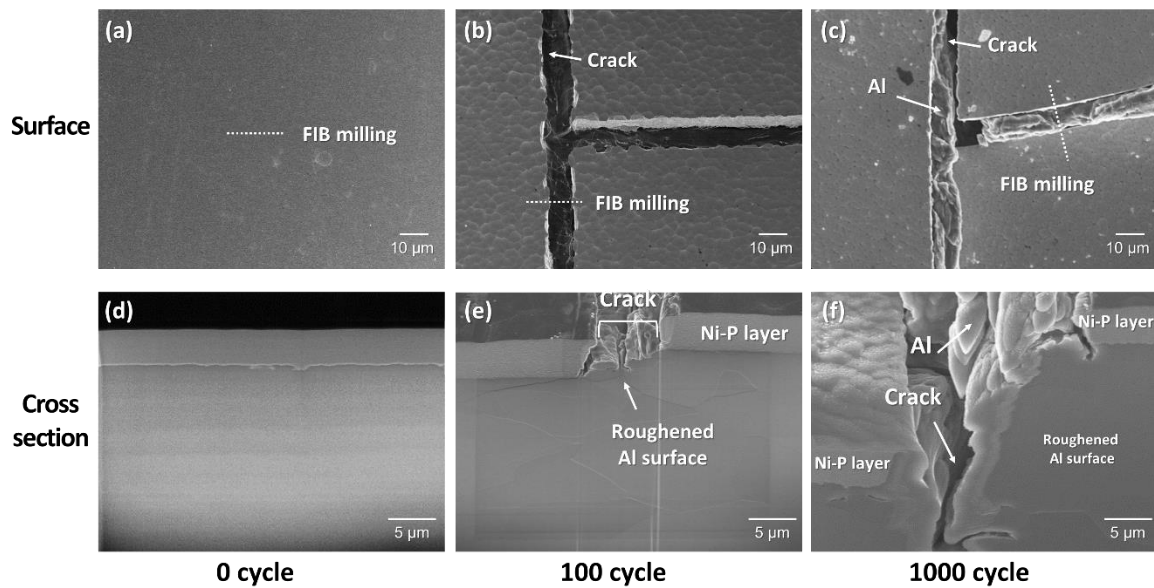

Fig. 3.11 Variation in surface roughness of Ni (a) and Ni–P (b) layers on DBA/AMB substrates with Al_2O_3, AlN, and Si_3N_4 up to 1000 cycles.

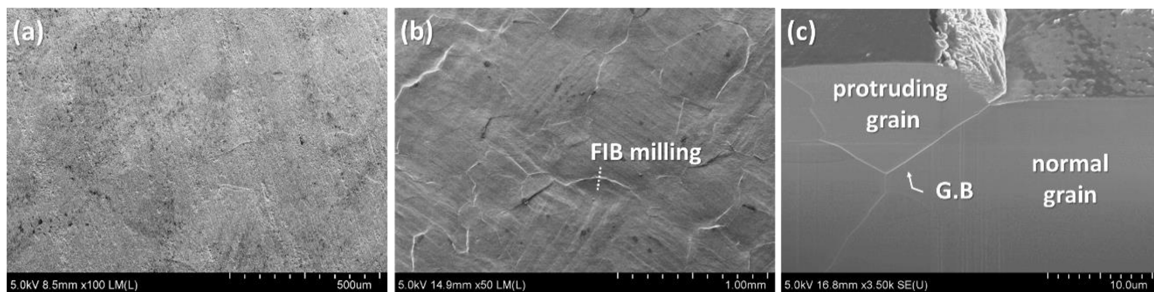

Fig. 3.12 SEM observation of bare aluminum surface in DBA substrates with Si_3N_4 at the initial state (a) and after thermal shock tests of 100 cycles (b), and FIB-milled cross section (c) at the location of surface deformation.

3.3.3 FEM simulation

Fig. 3.13 shows the maximum principal stress distribution of DBA and AMB with the same Si_3N_4 plated with Ni and Ni–P layers. The FEM simulation of the maximum principal stress distribution was conducted at the thermal shock cycling test from −50 °C to 250 °C. In the case of DBA, the stress concentration at the interface between the polycrystalline Al grain layer and the plated Ni and Ni–P layers is shown in Fig. 3.13a,c. The maximum stress was 69 and 30 MPa for the Ni- and Ni–P-plated layers, respectively. In the case of AMB, the maximum principal stress was also concentrated at the interface between the crystalline Cu layer and the Ni and Ni–P layers, as shown in Fig. 3.13b,d, respectively. The maximum stress at the interface of Ni/Cu was also larger than that of Ni–P/Cu. This result is caused by the differences of materials properties between Ni and Ni–P layers, especially Young’s modulus, as shown in Table 3.2. In addition, although the maximum stress at the interface between the Ni layer and Cu/Al layers was larger than that between the Ni–P layer and Cu/Al layers, the surface deformation and crack occurred at the Ni–P layer on DBA and AMB substrates, as shown in Fig. 3.4d and 7d. The cracking of the Ni–P layer can be explained by the difference in fracture toughness between electroless-plated Ni–P and electroplated Ni layers. The fracture toughness of a crystalline Ni–P electroless plating layer is between 1.1 and 2.1 $MPa \cdot m^{1/2}$ [32–34], while an electroplated Ni layer is around 53 $MPa \cdot m^{1/2}$ [31]. High fracture toughness is closely related to crack initiation resistance and slow crack growth under the same stress conditions [36]. Ductile Ni layer with a higher fracture toughness likely suppressed crack initiation as well as growth by absorbing cracking energy. This is the reason why the electroplated Ni layer showed better crack resistivity during thermal shock test. The FEM simulation result indicates that the fracture toughness of the plating layer on DBA substrates is a key factor, which strongly influences crack generation and propagation.

Compared with the maximum stress that appears in the DBA substrates, the maximum stress increased in AMB substrates for both plating layers; although, Al in DBA had a bigger CTE mismatch with ceramic compared with Cu in AMB. The stress changes from 69 MPa to 85 MPa in the case of Ni plating, while it changes from 30 MPa to 57 MPa in the case of the Ni–P plating substrate. Since Al has lower Young's modulus as well as yielding stress, stress relaxation during thermal shock test becomes effective. The results also supports the experimental results, which demonstrates that AMB substrates with Al_2O_3 and AlN ceramics fractured easily, as shown in Fig. 3.3. In addition, it was also found that the stress distribution accumulated at the grain boundary and triple points in Al and Cu layers. Thermal stress concentration at grain boundaries and triple points due to material and geometrical singularities. As explained in Section 3.3.2, GBS deformation occurred in Al and Cu layers along with grain boundaries, leading to deformation and crack generation of a Ni–P layer plated on DBA and AMB substrates.

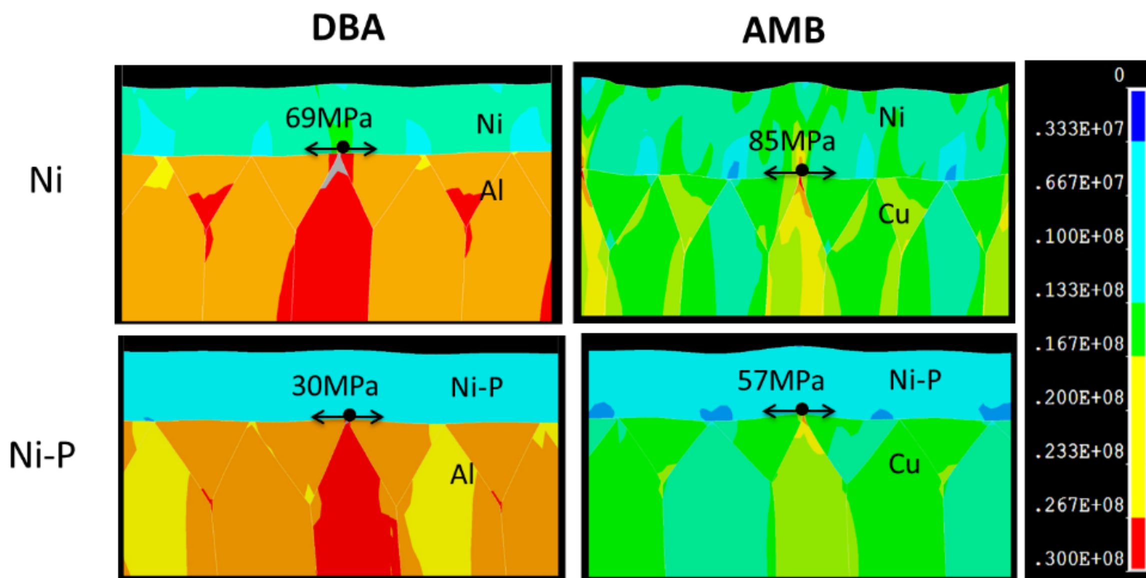

Fig. 3.13 Maximum principal stress distribution for Ni and Ni–P layers on DBA/AMB substrates with Si_3N_4 at 250 °C during thermal shock cycling test.

3.4 Conclusion

In this chapter, a thermal shock cycling test of DBA/AMB substrates with three types of ceramic plates and with two types of Ni metallization was presented. The material combination for high thermal shock resistance was confirmed. The failure mechanism for Ni and Ni–P plating layers on ceramic substrates was also discussed.

1. AMB substrates with AlN and Al_2O_3 fractured only after a thermal shock test of 10 cycles between −50 °C and 250 °C, while AMB with Si_3N_4 survived after a thermal shock test up to 1000 cycles. On the other hand, all DBA substrates survived up to 1000 cycles. However, after 1000 cycles, Ni–P electroless plating layer on DBA/AMB substrates became rough and cracked, regardless of ceramic and metal type after 1000 cycles, while Ni electroplating was not cracked. This is because ductile Ni layer had a higher fracture toughness than Ni–P layer, which can suppress crack generation by absorbing cracking energy.
2. Beneath a cracked Ni–P layer of DBA substrates, severe GBS deformation of Al was observed. Such deformation resulted in cracking and roughening of a Ni–P layer. Thermal stress distribution simulation indicates that tensile stress was concentrated at the interface between polycrystalline metal layers and a plated Ni–P layer, along with grain boundary. The cracking mechanism of a Ni–P layer is well explaned by the GBS deformation of metals.
3. Ni-plated AMB substrates with Si_3N_4 as well as Ni-plated DBA substrates with Al_2O_3, AlN, and Si_3N_4 are promising material combinations for high-temperature power substrates based on the proper ductility of an electroplated Ni layer.

Reference

[1] T. J. Flack, B. N. Pushpakaran, and S. B. Bayne, "GaN technology for power electronic applications: A review". J. Electron. Mater., vol. 45, pp. 2673–2682, 2016.

[2] T. P. Chow, "High-voltage SiC and GaN power devices," Microelectron. Eng., 83, pp. 112–122, 2006.

[3] R. Khazaka, L. Mendizabal, D. Henry, R. Hanna, "Survey of high-temperature reliability of power electronics packaging components". IEEE Trans. Power Electron., vol. 30, pp. 2456–2464, 2015.

[4] D. Hamilton, L. Mills, J. Bowen, M. Jennings, P. Mawby, "High temperature reliability of power module substrates". In Proceedings of PCIM Europe 2015, International Exhibition and Conference for Power Electronics, Intelligent Motion, Renewable Energy and Energy Management, Nuremberg, Germany, pp. 1–7, 2015.

[5] C. Y. Lin, W. H. Tuan, "Direct bonding of aluminum to alumina for thermal dissipation purposes". Int. J. Appl. Ceram. Technol., vol. 13, pp. 170–176, 2016.

[6] K. Hromadka, J. Stulik, J. Reboun, A. Hamacek, "DBC technology for low cost power electronic substrate manufacturing". Procedia Eng., vol. 69, pp. 1180–1183, 2014.

[7] A. Lindemann, G. Strauch, "Properties of direct aluminium bonded substrates for power semiconductor components". IEEE Trans. Power Electron., vol. 22, pp. 384–391, 2007.

[8] M. Y. Tsai, P. S. Huang, C. H. Lin, C. T. Wu, S. C. Hu, "Mechanical design and analysis of direct-plated-copper aluminum nitride substrates for enhancing thermal reliability". Microelectron. Reliab., vol. 55, pp. 2589–2595, 2015.

[9] L. Xu, M. Wang, Y. Zhou, Z. Qian, S. Liu, "An optimal structural design to improve the reliability of Al_2O_3-DBC substrates under thermal cycling". Microelectron. Reliab., vol. 56, pp. 101–108, 2016.

[10] M. Fei, R. Fu, S. Agathopoulos, J. Fang, C. Wang, H. Zhu, “A preparation method for Al/AlN ceramics substrates by using a CuO interlayer”. Mater. Des., vol. 130, pp. 373–380, 2017.

[11] P. Zhang, R. Fu, Y. Tang, B. Cao, M. Fei, Y. Yang, “Morphology of thick film metallization on aluminum nitride ceramics and composition of interface layer”. Ceram. Int., vol. 41, pp. 13381–13388, 2015.

[12] T. G. Lei, J. N. Calata, K. D. T. Ngo, G. Q. Lu, “Effects of large-temperature cycling range on direct bond aluminum substrate”. IEEE Trans. Device Mater. Reliab., vol. 9, pp. 563–568, 2009.

[13] C. D. Gu, Y. H. You, Y. L. Yu, S. X. Qu, J. P. Tu, “Microstructure, nanoindentation, and electrochemical properties of the nanocrystalline nickel film electrodeposited from choline chloride-ethylene glycol”. Surf. Coat. Technol., vol. 205, pp. 4928–4933, 2011.

[14] A. M. Rashidi, A. Amadeh, “Effect of electroplating parameters on microstructure of nanocrystalline nickel coatings”. J. Mater. Sci. Technol., vol. 26, pp. 82–86, 2010.

[15] C. A. Loto, “Electroless nickel plating – A review”. Silicon, vol. 8, pp. 177–186, 2016.

[16] K. H. Krishnan, S. John, K. N. Srinivasan, J. Praveen, M. Ganesan, P. M. Kavimani, “An overall aspect of electroless Ni-P depositions—A review article”. Metall. Mater. Trans., vol. 37A, pp. 1917–1926, 2006.

[17] K. G. Keong, W. Sha, S. Malinov, “Crystallisation kinetics and phase transformation behaviour of electroless nickel-phosphorus deposits with high phosphorus content”. J. Alloys Compd., vol. 334, pp. 192–199, 2002.

[18] M. O. Alam, Y. C. Chan, K.C. Hung, “Reliability study of the electroless Ni–P layer against solder alloy”. Microelectron. Reliab., vol. 42, pp. 1065–1073, 2002.

[19] B. Färber, E. Cadel, A. Menand, G. Schmitz, R. Kirchheim, “Phosphorus segregation in

nanocrystalline Ni-3.6 at.% P alloy investigated with the tomographic atom probe (TAP)". Acta Mater., vol. 48, pp. 789–796, 2000.

[20] Q. X. Mai, R. D. Daniels, H. B. Harpalani, "Structural changes induced by heating in electroless nickel-phosphorus alloys". Thin Solid Films, vol. 166, pp. 235–247, 1988.

[21] S. Pietranico, S. Pommier, S. Lefebvre, S. Pattofatto, "Thermal fatigue and failure of electronic power device substrates". Int. J. Fatigue, vol. 31, pp. 1911–1920, 2009.

[22] L. Dupont, Z. Khatir, S. Lefebvre, S. Bontemps, "Effects of metallization thickness of ceramic substrates on the reliability of power assemblies under high temperature cycling". Microelectron. Reliab., vol. 46, pp. 1766–1771, 2006.

[23] Z. Ning, Y. He, W. Gao, "Mechanical attrition enhanced Ni electroplating". Surf. Coatings Technol., vol. 202, pp. 2139–2146, 2008.

[24] MIL-STD-883E: "Test method standard for microcircuits"; Department of Defense: Columbus, USA, 1996.

[25] AQG 324: "Qualification of power modules for use in power electronics converter units in motor vehicles"; European Center for Power Electronics: Nuremberg, Germany, 2018.

[26] A. Fukumoto, D. Berry, K. D. T. Ngo, G. Q. Lu, "Effects of extreme temperature swings (−55 °C to 250 °C) on silicon nitride active metal brazing substrates". IEEE Trans. Device Mater. Reliab., vol. 14, pp. 751–756, 2014.

[27] A. Basavalingappa, M. Y. Shen, J. R. Lloyd, "Effect of texture and elastic anisotropy of copper microstructure on reliability". Mech. Adv. Mater. Mod. Process., vol. 3, pp. 6, 2017.

[28] H. Liang, C. Woo, H. Huang, A. H. W. Ngan, T. X. Yu, "Surfaces during nanoindentation". Comput. Model. Eng. Sci., vol. 6, pp. 105–114, 2004.

[29] R. Komanduri, N. Chandrasekaran, L. M. M. D. Raff, "Simulation of nanometric cutting

of single crystal aluminum-effect of crystal orientation and direction of cutting". Wear, vol. 242, pp. 60–88, 2000.

[30] K. Seigo, M. Sato, "Properties of electroless nickel deposit". J. Surf. Finish. Soc. Jpn., vol. 64, pp. 118–122, 2014.

[31] W. Dai, C. Oropeza, K. Lian, W. Wang, "Experiment design and UV-LIGA microfabrication technology to study the fracture toughness of Ni microstructures". Microsyst. Technol., vol. 12, pp. 306–314, 2006.

[32] Q. J. Zhou, J. Y. He, D. B. Sun, W. Y. Chu, L. J. Qiao, "Deformation and fracture of nickel phosphorus coatings". Scr. Mater., vol. 54, pp. 603–608, 2006.

[33] A. Roman, D. Chicot, J. Lesage, "Indentation tests to determine the fracture toughness of nickel phosphorus coatings". Surf. Coat. Technol., vol. 155, pp. 161–168, 2002.

[34] B. Bozzini, M. Boniardi, "Fracture toughness of supported Ni-P films prepared by autocatalytic chemical deposition". Z. Met., vol. 88, pp. 493–497, 1997.

[35] C. Molteni, N. Marzari, M. C. Payne, V. Heine, "Mechanisms in aluminum grain boundaries". Phys. Rev. Lett., vol. 79, pp. 869–872, 1997.

[36] R. O. Ritchie, A. W. Thompson, "On macroscopic and microscopic analyses for crack initiation and crack growth toughness in ductile alloys". Metall. Trans. A, vol. 16, pp. 233–248, 1985.

Chapter 4

Real-time Al ribbon fatigue monitoring by using AE

4.1 Introduction

In general, the wear-out failure of power electronics devices has been evaluated by Physics-of-Failure (POF) analysis after power cycling test (PCT) or thermal shock test (TST) [1][2][3]. However, the POF analysis is much complex and expensive to be applied in field reliability and it cannot predict the lifetime of power electronics. Recently, many studies have focused on the real-time monitoring methods using various failure precursor parameters, which allowing to analyze the wear-out failure mechanism and lifetime during a reliability test. The value of failure precursor parameters such as ON-state resistance, collector-emitter voltage, forward voltage, junction temperature and thermal resistance are well related and changed with the wear-out failure of packaging components during device operation, and thus can provide the information for final failure [4][5]. However, the current failure precursor monitoring was limited to apply in real power electronic devices [6] because it needs an additional electric circuit and high-resolution measurement to sense a small deviation under a high-voltage high-current operation [7]. Additionally, failure precursor parameters are sensitive to final failure, while it cannot detect the failure progress [8]. Finally, the variation in one of the failure precursor parameters can affect another parameter, which results in an incorrect understanding of wear-out damage mechanism and lifetime prediction [9][10]. Therefore, it is still needed to modify failure precursor monitoring.

An acoustic emission (AE) monitoring has been used as a real-time evaluation technique for material damage in bulk materials [11] as well as various microelectronics such as a lithium-ion battery [12], multi-layered ceramic capacitor [13], and fuel cell [14]. An AE sensor is attached to the test object and collects the elastic waves released from materials when they are damaged such as cracking, delamination and fracture simultaneously during a reliability test. Fig. 4.1 shows the occurrence and propagation process of elastic waves from the wear-out

failure of power electronic devices as an example. The collected elastic waves were called as AE signals, which include various damage information such as the amount, size, and growth ratio of damage. By analyzing the time-domain and frequency-domain characteristics of AE signals including counts, amplitude, and a central frequency, the damage and final failure information can be defined. Recently, Tommi et al. tried to conduct an AE sensor on a half-bride power module which consists of power semiconductors, capacitor and inductors during PCT [15]. Although AE signals were collected during power module switch, it could not be confirmed these AE signals are released from wear-out failure or just generated from the power on-off switch. Therefore, in order to apply AE to monitor the wear-out failure of power electronic devices, the relationship between collected AE signals and damage should be confirmed. In addition, for accurate AE assessment, background AE noise, such as the power on-off switch noise and surroundings noise, need to be filtered during PCT.

In this chapter, AE was the first time applied to real-time monitor the wear-out failure of discrete SiC Schottky barrier diode (SiC-SBD) devices during PCT. The structure of discrete SiC-SBD devices, PCT setups and a real-time AE monitoring system were explained. The forward voltage of discrete devices was monitored during power cycling. The Physic-of-Failure (POF) analysis of tested power discrete devices by field emission scanning electron microscopy (FE-SEM) and X-ray inspections was performed. Background AE noise was filtered by the noise cancelling process for accurate AE assessment. AE signals were collected during PCT and the relationship between the observed damage and the collected AE signals was discussed. Finally, based on the relationship, the ability of proposed real-time AE monitoring was demonstrated.

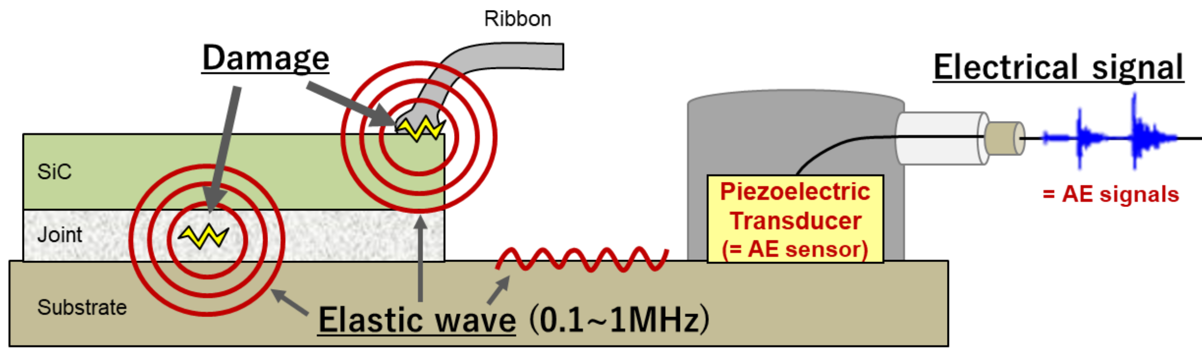

Fig. 4.1 Generation, propagation, and collection process of acoustic emission signals (i.e. elastic waves) in power electronics during PCT.

4.2 Experiment

4.2.1 The tested discrete devices

Power semiconductors such as MOSFET, IGBT, diode are commonly packaged in two kind structures such as discrete devices and power electronic modules. Compared with modules, discrete devices have a simpler packaging structure including one power semiconductor, a substrate, die-attachment (i.e. joints), and wire interconnection. In this work, as the first attempt of AE monitoring, a discrete device having a simpler packaging structure was used. Fig. 4.2 shows the tested discrete device, which was fabricated using one 1200V/50A SiC Schottky barrier diode (SBD) with a dimension of 4.77 mm × 4.77 mm × 0.235 mm. The SiC-SBD device was die attached on an active metal brazing (AMB) substrate by using micron Ag sinter paste and was interconnected by Al ribbons. The AMB consists of a Si_3N_4 ceramic plate of 0.32 mm thickness and two Cu metallized layers of 0.30 mm thickness. Among three types of ceramic including Al_2O_3, AlN, and Si_3N_4 in AMB substrates, the Si_3N_4 based AMB substrate was selected due to which possessed the highest thermal damage resistance [16][17]. To focus on failure monitoring of Al ribbons in the discrete device, Ag micro-particles sinter paste [18] was chosen as the die attach materials because it has a higher thermal resistance than that of traditional high-temperature solder [19–21]. For Ag sinter joints, the backside of the SBD device and the top side of AMB substrates were metallized with a 100 nm Ti barrier layer and 2 μm Ag adhesion layer in order. The Ag paste was printed on the AMB substrates with 100 μm by using a stainless screen mask. The devices were placed onto the printed paste and heated at 250 °C for one hour without sintering pressure. Afterward, two Al ribbons with each cross-section area of 1.5 × 0.2 mm^2 were bonded on the SiC-SBD device and the Cu layer of an AMB substrate using an ultrasonic ribbon bonder (HB-30, TPT Co.) with ultrasonic power of 20 W for 2 s [22].

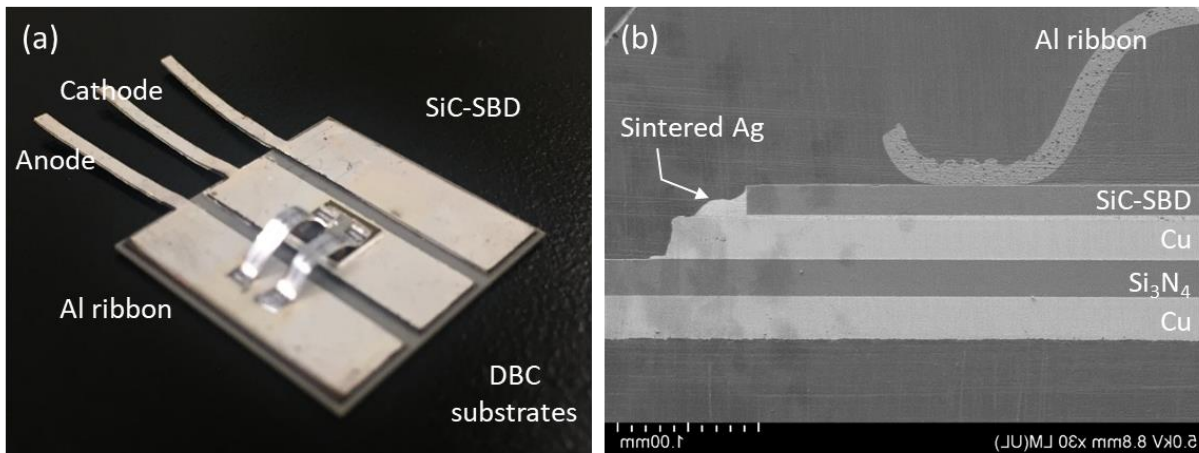

Fig. 4.2 Fabricated discrete SiC-SBD devices; (a) optical image and (b) its cross-section SEM image.

4.2.2 Power cycling test (PCT) system and setup

PCT were carried out using a power cycle test system (PST-2404, ESPEC Co.), consisting of power supply, switching circuit, V_F measurement circuit, heatsink, and an air cooling system. The discrete device was mounted on the heatsink as shown in Fig. 4.3(a). A 50 µm-thick silicon film was placed between the modules and the heatsink to reduce interfacial thermal resistance. The heatsink was cooled by a rotating fan, where the temperature was maintained at approximately 25 °C.

During PCT, the discrete device was heated by a constant stress current (Is) of 45 A, as shown in Fig. 4.4. The heating ON time and OFF time were fixed at 2 s and 30 s respectively, performing an initial junction temperature swing (ΔT_j) of 150 °C. This PCT condition was listed in Table 1. The harsh temperature swing was chosen for this accelerate PCT test, which was larger than general T_j of 100 °C [23]. Before and after carrying the stress current, the junction temperature (T_j) was measured using temperature dependent forward voltage (V_F). The value of T_j was calculated by

$$T_j = \mathrm{K}V_F + m \tag{4.1}$$

where V_F was measured under low measurement current (I_m) of 400 mA, K is the linear association constant between V_F and T_j, which is referred to as K-factor [24], and m is the material constant. K and m could be calculated by measuring V_F at several different temperatures from 25 °C to 200 °C prior to PCT.

During PCT, V_{F_ON} and T_j were recorded at each cycle and monitored as a failure precursor parameter, which was well known as a good indicator for detecting the wear-out failure in bond-wire and die-attachment [6]. The temperature swing was repeated up to failure

based on failure criteria, which was defined as a rise of the V_F by 20 % compared to its initial value to protect the tested discrete devices against catastrophic failure [25].

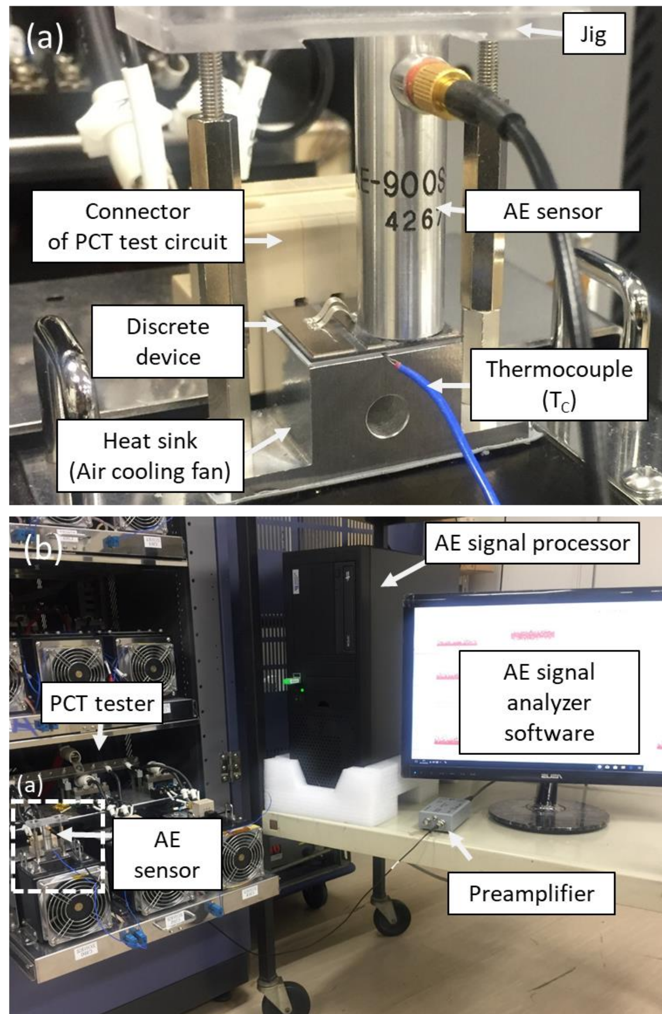

Fig. 4.3 Configuration of power cycling test system and real-time acoustic emission monitoring system.

Table 4.1 Power cycling test condition.

Stress current (I_s)	Stress time	Measurement current (I_m)	Cooling time	Junction temperature Minimum (T_{j_min})	Junction temperature Maximum (T_{j_max})	Temperature swing (ΔT_j)
45A	2 s	0.4 A	30 s	25 ºC	175 ºC	150 ºC

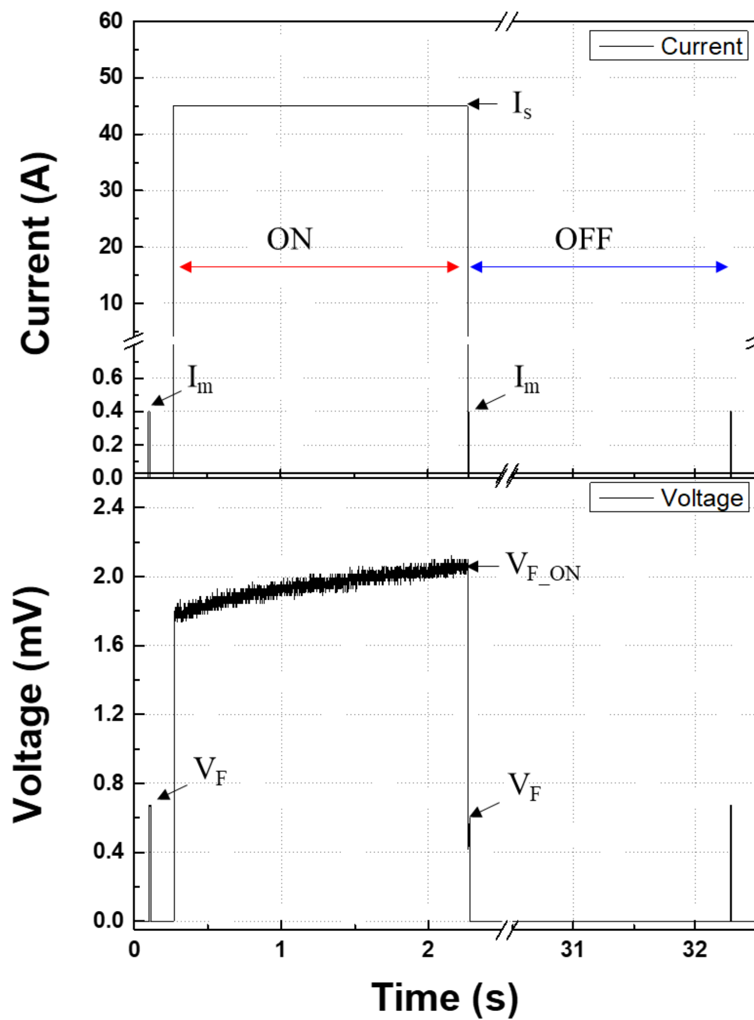

Fig. 4.4 Profile of voltage and current during power cycling test.

4.2.3 Acoustic emission (AE) monitoring system and setup

The AE monitoring was suggested as a new wear-out failure monitoring method. During PCT, AE signals were detected from discrete devices and used to monitor the progress of failure. As shown in Fig. 4.3(a), the experimental apparatus was specially designed to simultaneously detect AE signals during PCT. AE signals were collected by a wideband piezoelectric AE sensor (AE-900S-WB, NF Electronics Co.), which was directly mounted onto the AMB substrate in discrete devices by using ultrasonic couplant and acrylic jig. The AE sensor is electrically insulated from the AMB substrate by an insulating ceramic layer on the bottom of the sensor. The wideband type sensor was chosen for frequency analysis of collected AE signals due to its high and uniform sensitivity in the large frequency range from 100 kHz up to 1 Mhz. The collected AE signals were amplified by a preamplifier (2/4/6, Physical Acoustic Co.) at a gain of 40dB and recorded at a sampling rate of 2 MHz by the AE acquisition system (PCI-2, Physical Acoustic Co.), as shown in Fig. 4.3(b).

The characteristics of AE signals can be used to evaluate material damage. Fig. 4.5 shows the representative waveform of AE signals and its time-domain characteristic parameters [12]. The highest sound pressure is defined as amplitude. Basically, a signal is recorded when its amplitude is higher than or equal to the threshold value, which is the criterion for effective signals. The number of times that waveform exceeds the threshold is defined as AE counts and its time derivative. In addition, the frequency-domain characteristics of AE signals can be analyzed through a Fast Fourier Transform (FFT). It is commonly used not only to determine AE source with time-domain parameters but also for eliminating noise.

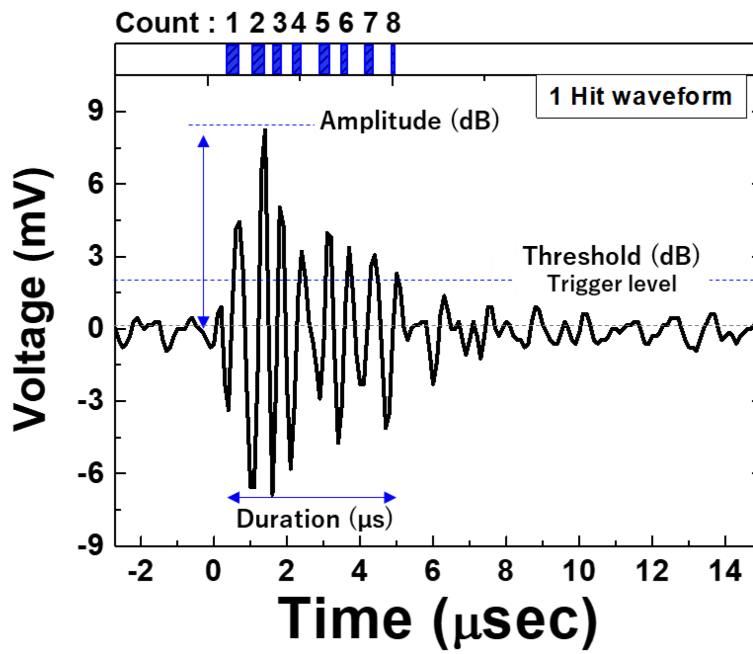

Fig. 4.5 Waveform of a collected AE signal and its characteristic including counts and amplitude.

4.2.4 Background AE noise cancelling process and setup

Noise cancelling method often has been applied to filter out the unnecessary noise and to collect the AE signals corresponding to the wear-out damage [26][27], which is considered as the most important step for accurate AE assessment. In noise cancelling, background noise must be collected under the same environment as an actual test and noise can be filtered out based on the investigated noise level including frequency. In this chapter, a noise levelling test was investigated using dummy specimens. The specimens were specially fabricated without the SiC-SBD chip and Ag sinter joints to avoid joule heating of a diode. The patterned Cu islands on substrates were interconnected by Al ribbons as shown in Fig. 4.6 (a). PCT was carried out on the dummy specimens under the same condition including high current and fan cooling introduced in table 1. During PCT, all AE noise signals were recorded with no filtering.

Fig. 4.6 (b), (c), and (d) show the representative surrounding noise signals from cables, a rotating fan, and switching on-off signals of high-current carrying circuits in the PCT system for the background AE noise cancelling process, respectively. The recorded noise signals did not include AE signals from the damage of discrete devices, since the used dummy specimen without a chip could not be heated and damaged even under high current. The cables in AE system had very low amplitude noise below 25 kHz. The mechanical vibration of a cooling fan (below 30 kHz) and the electromagnetic interference (EMI) of current switching (below 87 kHz) also generated noise signals. The frequency level of collected AE noise is ranged less than 87 kHz. Based on these results, the high-pass frequency filter at 100 kHz was employed to eliminate noise in PCT and AE system. In addition, low-pass filter the amplitude thresholds was set at 30 dB. Afterward, the noise levelling test using dummy specimens was repeated with these setup of low-pass filter and thresholds. AE signals were not detected and no occurrence

of AE signals during PCT clearly proves that the noise cancelling process completely eliminates the background AE noise.

This demonstrates that noise signals from the current PCT system were completely eliminated by high pass filter. Afterward, true AE signals were collected during PCT and the characteristics of signals were monitored as failure indicator. In addition, most industrial machinery vibration including motor and engine has the frequency response characteristic below 10 kHz. Thus, the AE system can be used for various power electronics in industrial environment without noise problem.

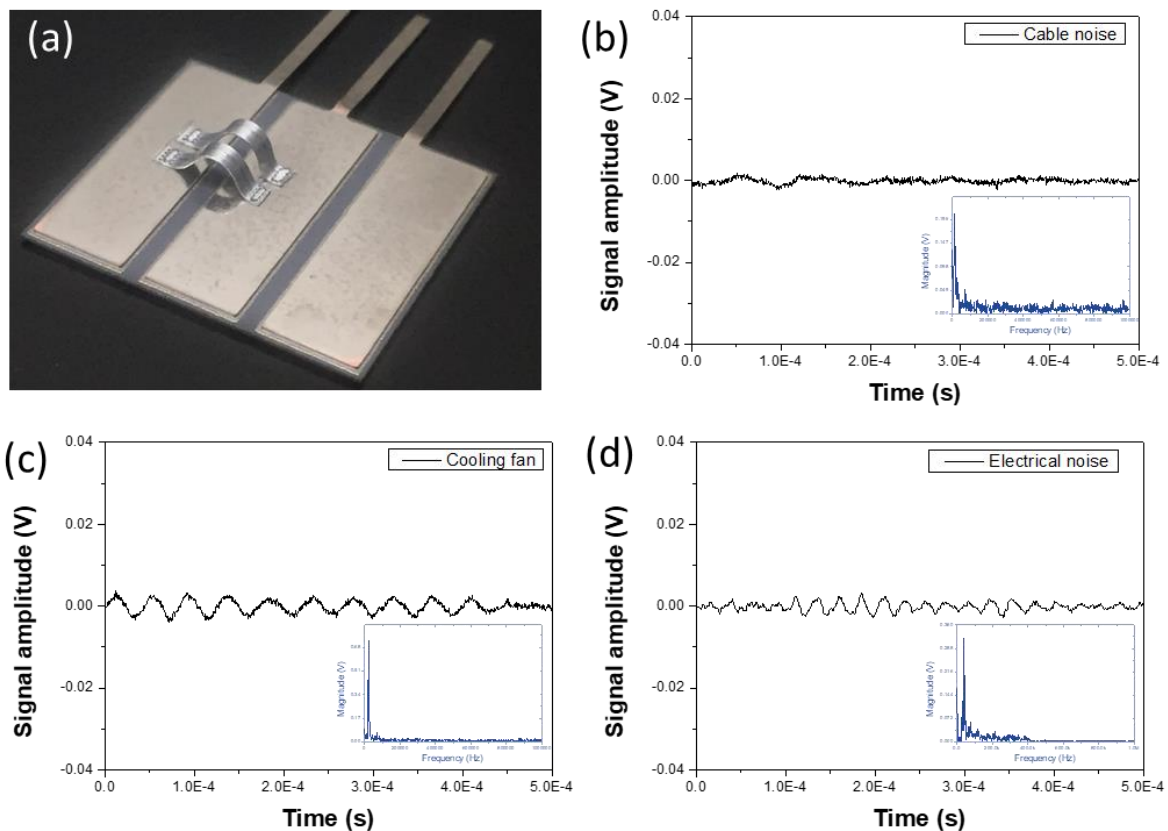

Fig. 4.6 Dummy specimens designed for noise cancelling and (b-d) Typical waveform and frequency spectrum of three types of collected noise; (a) cable noise, (b) cooling fan movement noise and (c) electromagnetic induction noise.

4.3 Power cycling test

4.3.1 Voltage precursor parameter monitoring in power cycling test

Fig. 4.7 shows the V_F measurement results of discrete SiC-SBD devices during the power cycling test under a test condition as listed in Table 1. After 4,060 cycles, there was a sudden increase in V_F and then the V_F increased by 20 % from its initial value after 5,123 cycles. Based on the failure criteria of a V_F increase, lifetime of devices could be determined.

Fig. 4.8 shows the comparison of current-voltage (I-V) characteristics of discrete devices before and after PCT. The I-V curves was measured at room temperature by a curve tracer (CS-3200, IWATSU Co.). The electrical resistance (R_F) of discrete devices was measured form I-V curves and it increased after PCT. The measured R_F is the sum of the individual resistance in chip and packaging and can be simply expressed as

$$R_F = R_{chip} + R_{package} \tag{4.2}$$

where R_{chip} and $R_{packaging}$ represent the resistance of the chip and the resistance of packaging elements including ribbons, die-attachment, metallization, and substrates, respectively. In general, an increase in R_{chip} occurs due to the oxidation of Si diodes' leads. In the case of SiC diodes, no remarkable change was noticed in the electrical characteristic up to maximum exposure temperature of 240 °C [28]. On the other hand, failure in die-attachment and bond wire makes the noticeable increase in R_F after PCT with ΔT_j from 80 °C to 160 °C, due to the reduction of cross-section area in packaging elements acting as the current path leads to an increase of $R_{packaging}$ [29]. Therefore, R_F increased after power cycling, which resulting from the failure such as cracks, delamination, and lift-off failure in die-attachment or in ribbon bonding. In addition, V_{F_ON} variation shown in Fig. 4.7 can be explained as

$$V_{F_ON} = I_s \cdot R_F = I_s \cdot (R_{chip} + R_{packaging}) \quad (4.3)$$

where I_s represents the stress current for heating in power cycling test. I_s was fixed at 45 A. For maintaining the constant stress current, the increase of R_F after PCT lead to an increase of V_{F_ON}.

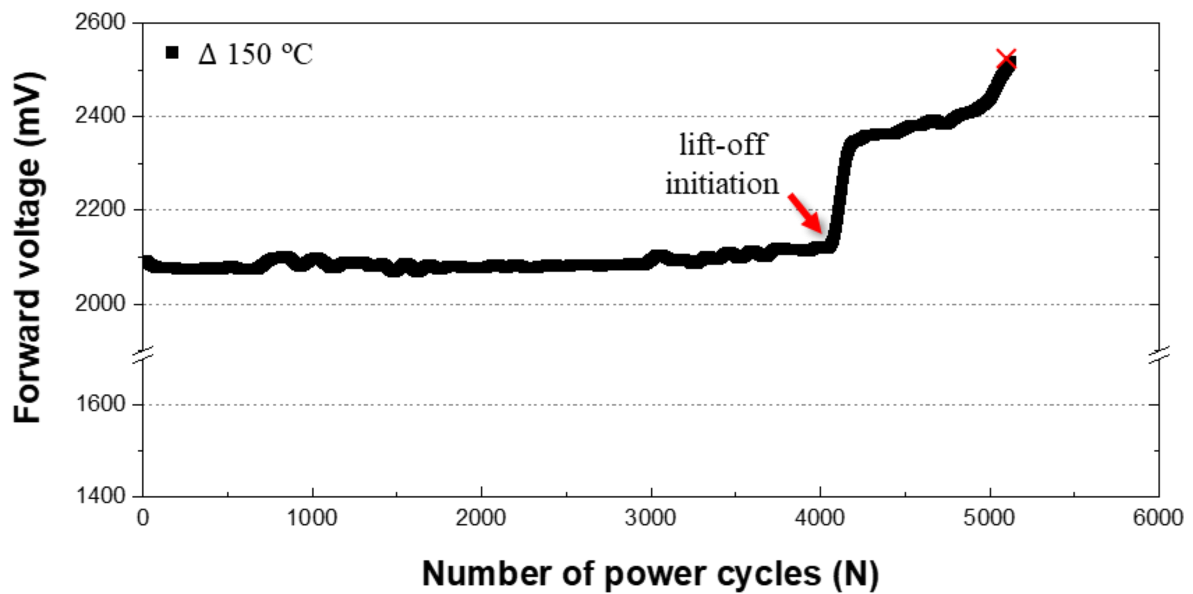

Fig. 4.7 Variation in forward voltage of a diode during PCT tests.

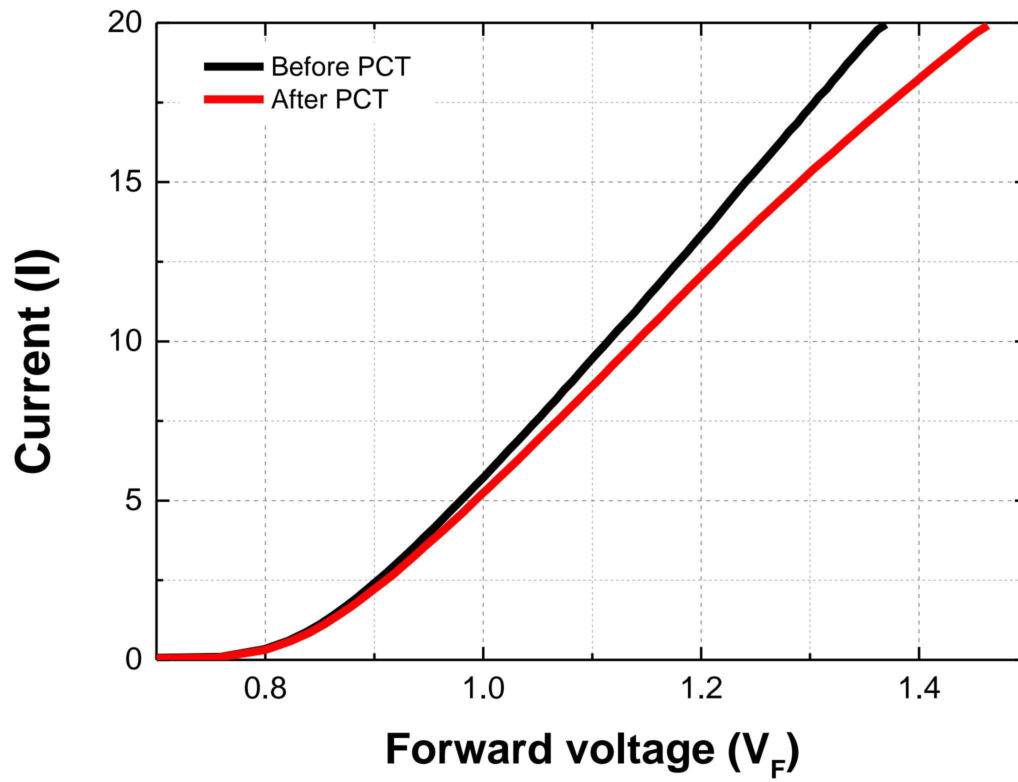

Fig. 4.8 I-V characteristics before and after PCT tests.

4.3.2 Physics-of-failure analysis of tested discrete devices

The failure mode of tested discrete devices was evaluated by FE-SEM observation and X-ray transmission inspection. Fig. 4.9 shows the inspection results of the appearance and fracture surface of devices after PCT. One of two Al ribbons was totally fractured by lift-off and another was still bonded on a chip as shown in Fig. 4.9 (a). Ratchet marks were observed on the fracture surface of the ribbon lift-off as shown in Fig. 4.9 (b). These marks, which are often observed on a fatigue fracture surface, indicate that this lift-off failure was induced by fatigue. In general, fatigue fracture has three steps including crack initiation, crack propagation and final fracture. The sharp fatigue cracks firstly occurred at the edge of Al ribbon bonding as shown in Fig. 4.9 (c). The cracks propagated into the center as the direction of ratchet marks as indicated in Fig. 9 (b) followed by the final lift-off failure. Striation marks in the vertical direction to ratchet marks were observed as shown in the magnified images of Fig. 4.9 (d), which also indicates the propagation direction of fatigue cracks.

Fig. 4.10 shows the cross-section of one unfractured ribbon of the tested discrete device after PCT. More than half of the bonded interface between an Al ribbon and a SiC-SBD chip was delaminated, which caused by fatigue cracks as shown in Fig. 4.10 (a). On the other hand, after PCT, any delamination did not occur at the interface between sintered Ag and the substrate or between sintered Ag and a SiC-SBD chip as shown in Fig. 4.10 (b). The Ag sinter joints maintained a micro-porous network structure without any obvious cracks, which attributed to robust die shear strength of around 40 MPa as well as the low resistivity of 3.9×10^{-6} Ω cm [18]. Fig. 4.11 shows the micro-focused X-ray inspection results of Ag sinter joints in the discrete device before and after PCT. There are some voids after sintering but which did not expand and not any new voids appeared after PCT. Although the thermal shock resistant of Ag sinter joints depends on manufacturing conditions, chip size and used Ag paste [30][31][32],

the results in the present study revealed that Ag sinter joints have an excellent high temperature reliability for this PCT.

Based on these results of Al ribbons and Ag sinter joints after PCT, fatigue cracks and lift-off in Al ribbons were the dominant failure mode for the discrete devices in the current study. The results also were similar with the previous studies where bond wire lift-off is the main failure mechanism. V_F of diodes goes up with the bond wire lift-off [33][34][35]. Therefore, Al ribbon's lift-off was the main reason of the increases in V_F as shown in Fig. 7 and it can be evaluated by the V_F measurement. However, although the observed fatigue cracks propagate gradually before final lift-off failure, V_F was not changed before the sudden increase which is caused by lift-off failure. In this case, V_{F_ON} measurement cannot monitor the progress of fatigue cracks in the Al ribbon resulting in the final ribbon's lift-off failure.

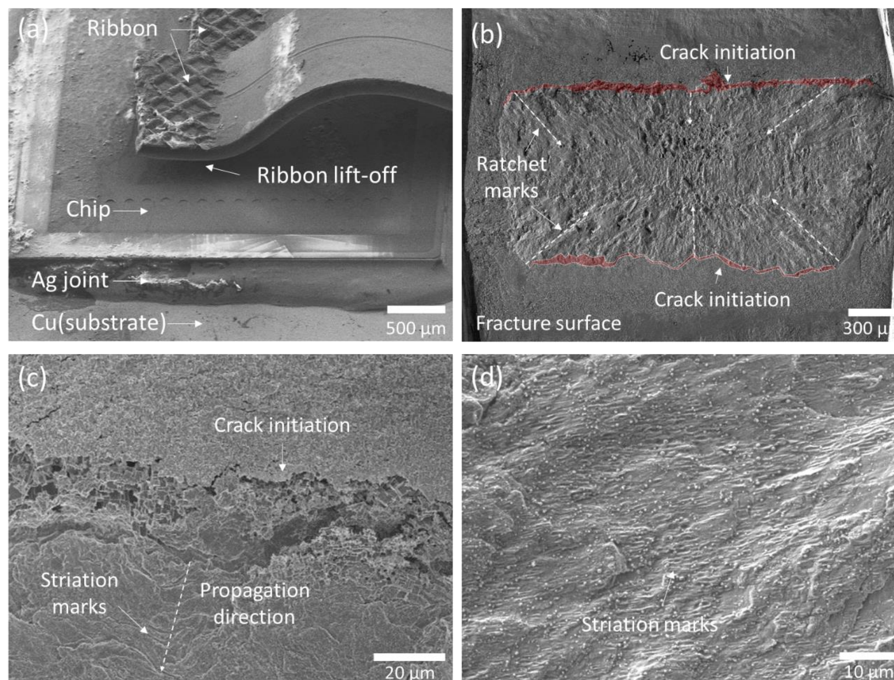

Fig. 4.9 Failure analysis results of failed discrete SiC-SBD devices after PCT tests; (a) lift-off failure of one Al ribbon, (b) fracture surface of lift-off ribbon, (c) magnified observation of crack initiation, and (d) magnified observation of fatigue fracture marks.

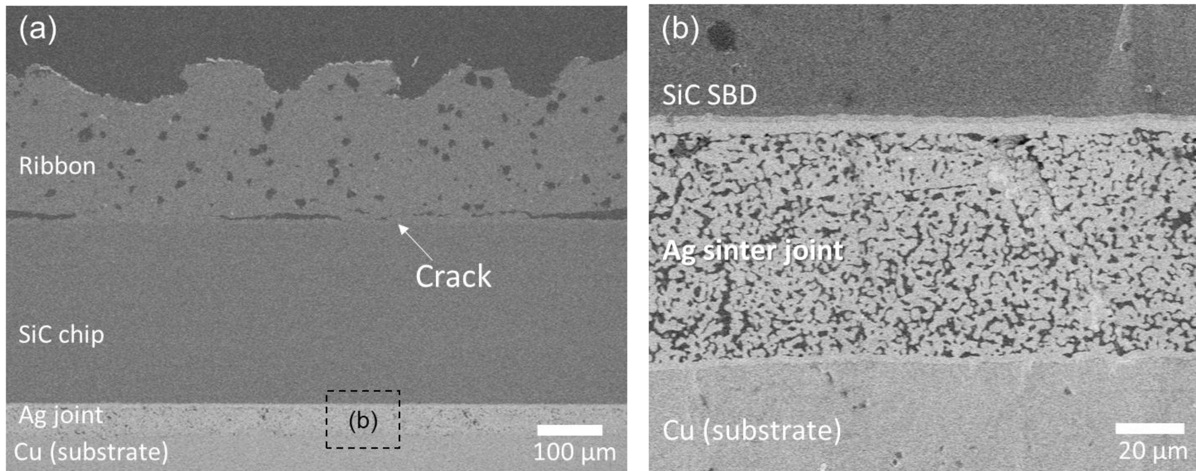

Fig. 4.10 (a) Cross-section observation of another unfractured ribbon portion after PCT tests and (b) a magnified cross-section image of Ag sinter joint.

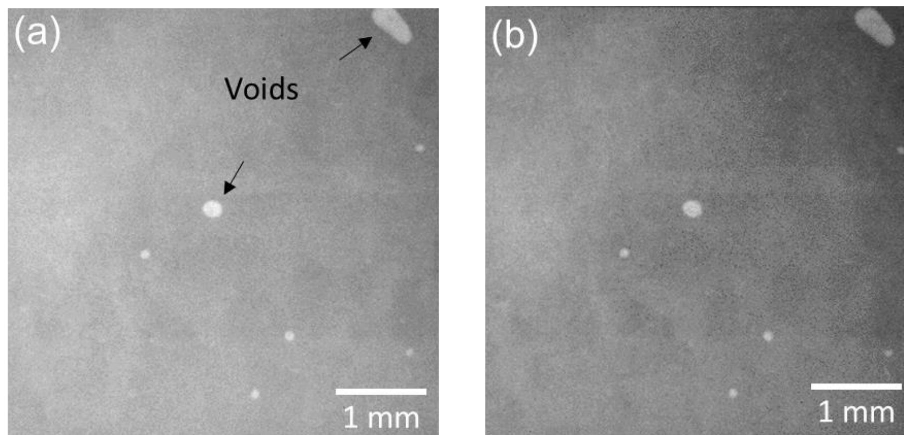

Fig. 4.11 Micro-focused X-ray inspection results of Ag sinter joint in devices before (a) and after (b) PCT tests.

4.4 Acoustic emission monitoring test

4.4.1 The source of acoustic emission

AE monitoring was simultaneously performed with PCT and a number of AE signals were collected during PCT. Fig. 4.12 shows typical waveforms and their frequency spectrum. Fig. 4. 12 (a) and (b) presented a signal waveform and amplitude, respectively. They indicate that the AE signals were burst type waveform, which was completely different compared to the noise signals as shown in Fig. 4.6. It is known that the burst type signals are often emitted by a sudden energy release when damage such as cracks and delamination occurs [36]. Based on the typical source of burst type and the observed fatigue cracks in Al ribbon bonding shown in Fig. 4.9, the source of collected AE signals from discrete devices during PCT can be attributed to fatigue cracks in Al ribbon bonding.

The frequency components of collected AE signals were estimated by fast Fourier transform (FFT) as typically shown in Fig. 4.12 (c) and (d). The signals were composed of various frequency components. A central frequency defined by the arithmetic mean of frequency components in the spectrum was used for characterizing the representative frequency of each AE signal [37]. The distribution of estimated central frequency has a bell-shaped curve as shown in Fig. 4.13. A peak in the distribution curve was around 500 kHz. The frequency component depends on the type of fracture, which is the source mechanism of AE signals [38]. The bell-shaped distribution with a single peak also supports that the collected AE signals are emitted just from the fatigue cracks in Al ribbon bonding.

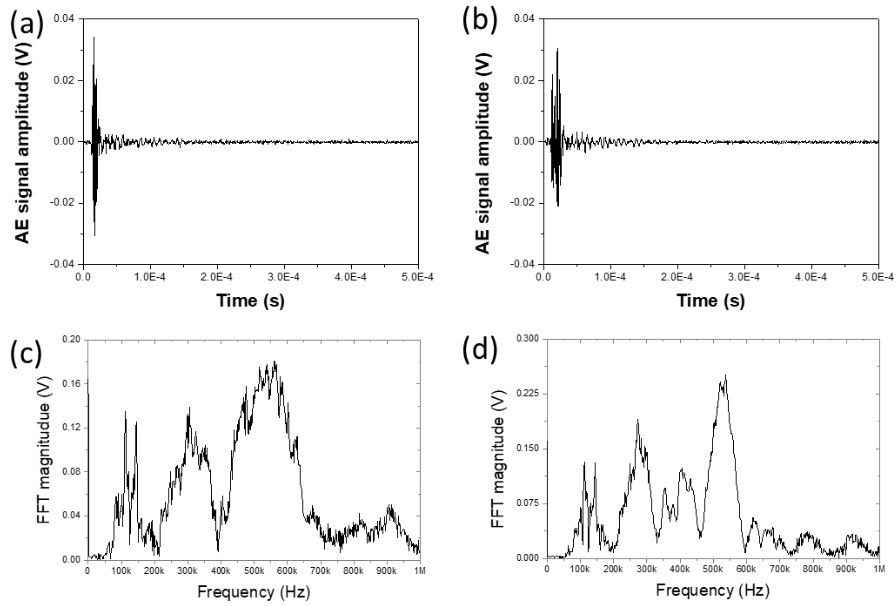

Fig. 4.12 Waveform (a-b) and its corresponding frequency spectrum (c-d) of typical AE signals collected during PCT tests.

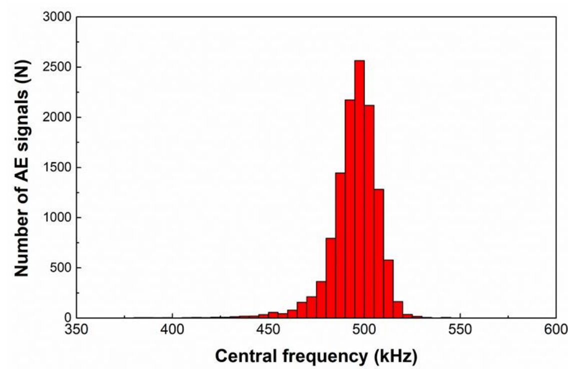

Fig. 4.13 Histogram of the measured central frequency of collected AE signals.

4.4.3 Monitoring by acoustic emission parameter

Two kinds of time-domain characteristic parameters of collected AE signals, including total AE counts and amplitude, were monitored during PCT and which were compared with V_{F_ON} monitoring results (Fig. 4.7) as shown in Fig. 4.14 and Fig. 4.15, respectively. Fig. 4.14 (a) shows the monitoring results of total AE counts in PCT. The total number of AE counts (i.e. total AE counts) increased at a different rate during PCT. The increase of total AE counts proceeded through three stages according to a count rate, which is equal with the inclination of the total count curve. Total AE counts steeply increased with a high count rate at first (stage 1), then increased smoothly with a low count rate (stage 2), and was as-followed by an abrupt increase (stage 3). The AE counts are generally considered to best reflect material damage and total AE counts are proportional to the progress of materials damage corresponding to AE source. Thus these results indicate that fatigue cracks propagated according to three stages at a different rate during PCT.

To clearly divide the progress of fatigue by the AE stage, an AE count rate was calculated as the total count number per cycle as shown in Fig. 4.14 (b). The change of count rate more clearly shows that the progress of fatigue crack can be divided into three stages as indicated by a red dashed line; into the highest count rate at the early step of PCT (stage 1), low count rate (stage 2), and re-high count rate (stage 3). The stage 2 and stage 3 were divided at around 4,060 cycles where a count rate started to increase again. In fatigue tests of bulk metals, high AE count rates are found when fatigue cracks are initiated, cracks are rapidly propagated, and metals are finally fractured [11][39][40][41]. Based on these previous study results, stage 1 is attributed to the crack initiation as shown in Fig. 4.9 (c). AE signals in stage 2 occur from the crack extension at the crack tip during the crack propagation as shown in Fig. 4.9 (d). In stage 3, crack propagation made catastrophic fractures, leading to an increase in an AE count rate.

Based on the relationship of the AE count rate and fatigue progress, it can be concluded that AE offers the ability to accurately not only detect fatigue crack but also crack propagation and catastrophic fracture. It demonstrates that the monitoring of the AE count rate can provide early warning before final lift-off fracture by evaluating the progress status of fatigue cracks.

Fig. 4.15 shows variation in the amplitude of collected signals during power cycling. One dot indicates the amplitude of one AE signal and a lot of AE signals with amplitude range from 30 dB to 71 dB occurred before lift-off failure. Low amplitude signals below 40 dB occurred through the whole process of fatigue damage but the high amplitude signals ranged from 41 to 71 dB were emitted in the early and in the middle of total power cycling. In a bulk metal, it was reported that high amplitude signals are generated by the plastic activities ahead of a crack tip when fatigue cracks initiate as well as rapidly propagate [42][43][44]. Thus high amplitude signals in stage 1 occurred from crack initiation in Al ribbons and those in stage 2 can be attributed to the accelerated crack propagation before ribbon's lift-off failure, which supporting the relationship of an AE count rate and fatigue progress.

Fig. 4.16 shows the cumulative counts of collected AE signals during switching ON and OFF period in PCT. The number of cumulative AE counts during the ON period of power cycling, which defined as the total amount of fatigue crack initiation and propagation, is significantly smaller than for that during the OFF period. AE occurrence suggests that the fatigue cracks of Al ribbon bonding almost nucleated and grew during the cooling stage in power cycling.

Future work will proceed with damage position identification in multichip IGBT modules. AE signals, which generated from the damage of numerous die-attachment and wire-bond in power modules, will be detected using four AE sensors. Based on the time delay of the detected AE signals from four sensors, damage position identification will be studied.

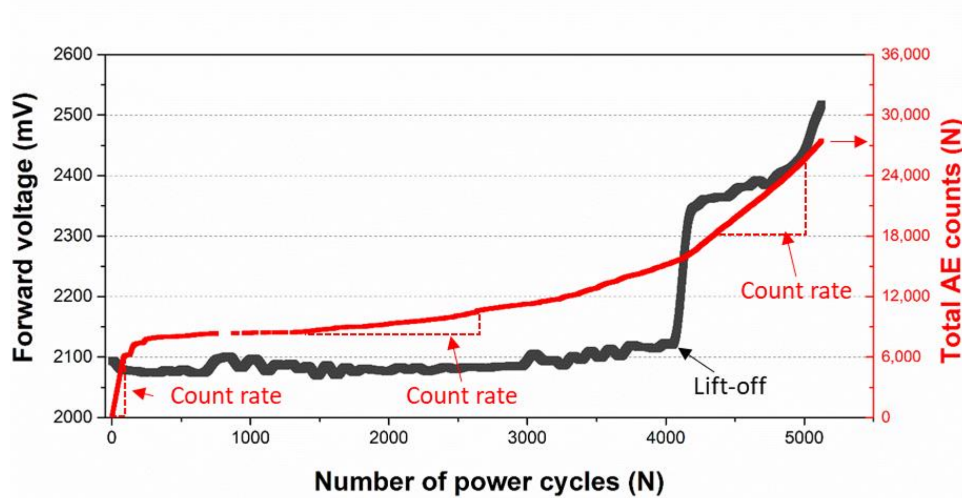

(a)

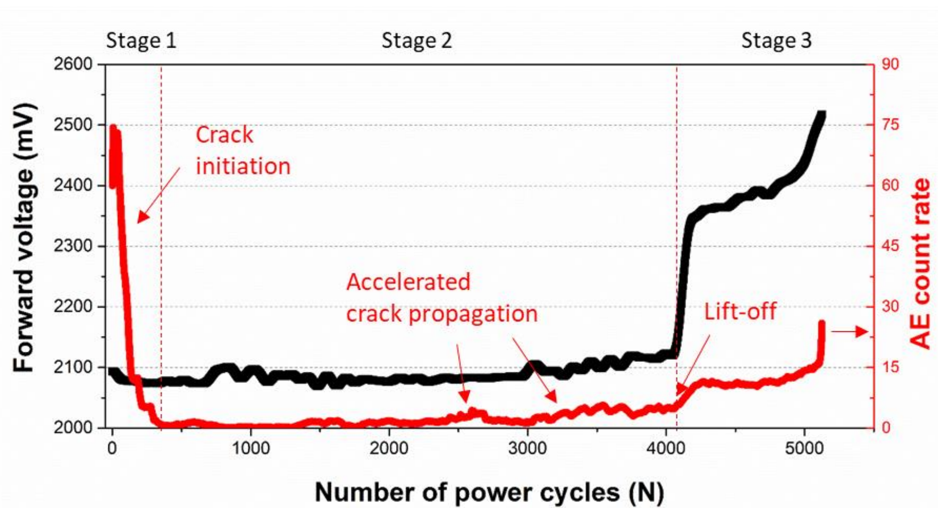

(b)

Fig. 4.14 Monitoring result of total AE counts (a) and AE count rate (b) during PCT with the monitoring results of forward voltage.

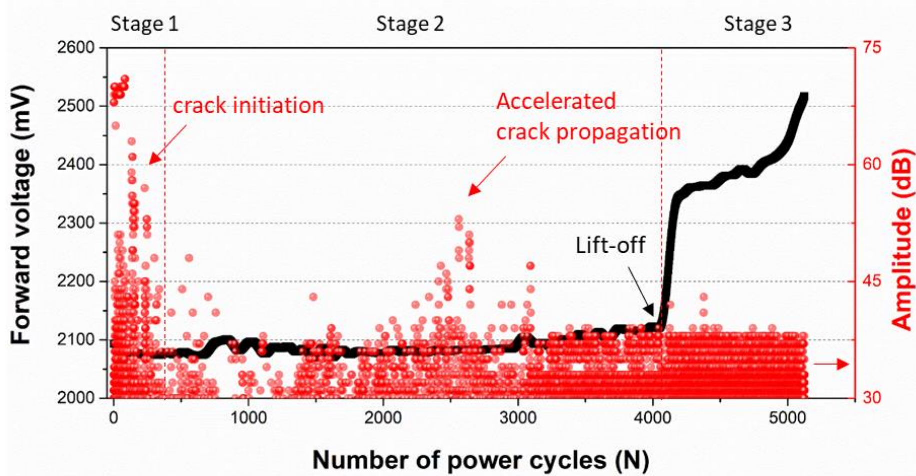

Fig. 4.15 Monitoring result of amplitude of collected AE signals during PCT with the monitoring results of forward voltage.

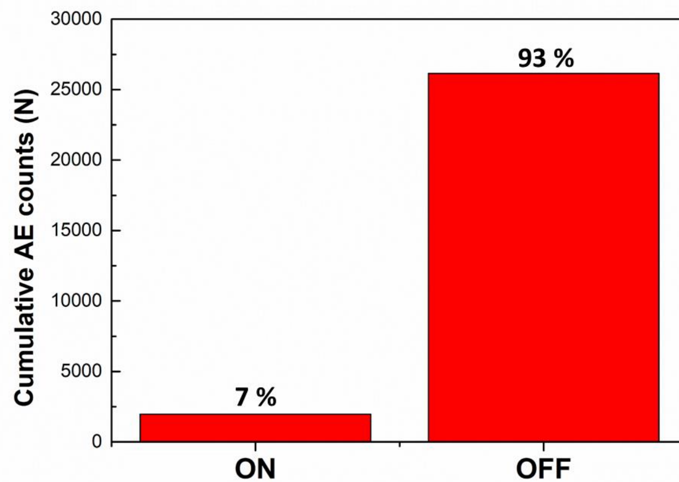

Fig. 4.16 Cumulative counts of collected AE signals during switching ON and OFF period of PCT.

4.5 Conclusion

This chapter presents that the application of AE monitoring can detect the progress of failure in power discrete SiC-SBD devices during power cycling test as follows.

Various AE noise including power switching noise was completely eliminated through noise cancelling process using the specially designed blank specimens. A number of AE signals were successfully detected during PCT before reaching final failure. By physics-of-failure analysis, the initiation and propagation of fatigue cracks of Al ribbons bonding were observed, while there was no thermal damage in Ag sinter joints. The source of AE signals is attributed to the initiation and propagation of fatigue cracks of Al ribbons. This demonstrates that AE monitoring has excellent sensitivity to fatigue cracking. AE acquisition can be used for a sensitive early warning method by detecting fatigue cracks leading to catastrophic ribbon's lift-off failure.

The variation of an AE count rate was divided into three stages, which highly correlated with three-step process of fatigue crack propagation observed in Al ribbon bonding, defined as initiation, propagation, and catastrophic lift-off fracture. The amplitude of collected AE signals supports the correlation between AE activities and the fatigue process. Thus, it can be concluded that AE monitoring offers not only detecting fatigue crack initiation and propagation but also an early warning before catastrophic lift-off fracture.

Reference

[1] 1. S. H. Tran, Z. Khatir, R. Lallemand, A. Ibrahim, J. P. Ousten, J. Ewanchuk, and S. V. Mollov, "Constant Δt j power cycling strategy in DC mode for top-metal and bond-wire contacts degradation investigations," IEEE Trans. Power Electron., vol. 34, no. 3, pp. 2171–2180, 2019.

[2] C. Durand, M. Klingler, M. Bigerelle, and D. Coutellier, "Solder fatigue failures in a new designed power module under power cycling," Microelectron. Reliab., vol. 66, pp. 122–133, 2016.

[3] V. N. Popok, K. B. Pedersen, P. K. Kristensen, and K. Pedersen, "Comprehensive physical analysis of bond wire interfaces in power modules," Microelectron. Reliab., vol. 58, pp. 58–64, 2016.

[4] N. Patil, J. Celaya, D. Das, K. Goebel, and M. Pecht, "Precursor parameter identification for insulated gate bipolar transistor (IGBT) prognostics," IEEE Trans. Reliab., vol. 58, no. 2, pp. 271–276, 2009.

[5] A. Hanif, Y. Yu, D. Devoto, and F. Khan, "A comprehensive review toward the state-of-the-art in failure and lifetime predictions of power electronic devices," IEEE Trans. Power Electron., vol. 34, no. 5, pp. 4729–4746, 2019.

[6] H. Oh, B. Han, P. McCluskey, C. Han, and B. D. Youn, "Physics-of-failure, condition monitoring, and prognostics of insulated gate bipolar transistor modules: A review," IEEE Trans. Power Electron., vol. 30, no. 5, pp. 2413–2426, 2015.

[7] U. M. Choi, F. Blaabjerg, and S. Jørgensen, "Power cycling test methods for reliability assessment of power device modules in respect to temperature stress," IEEE Trans. Power Electron., vol. 33, no. 3, pp. 2531–2551, 2018.

[8] A. Lahyani, P. Venet, G. Grellet, and P. J. Viverge, "Failure prediction of electrolytic

capacitors during operation of a switchmode power supply," IEEE Trans. Power Electron., vol. 13, no. 6, pp. 1199–1207, 1998.

[9] H. Huang and P. A. Mawby, "A lifetime estimation technique for voltage source inverters," IEEE Trans. Power Electron., vol. 28, no. 8, pp. 4113–4119, 2013.

[10] U.-M. Choi, F. Blaabjerg, S. Jorgensen, M.-N. Stig, and R. Bjorn, "Reliability improvement of power Converters by means of condition monitoring of IGBT modules," IEEE Trans. Power Electron., vol. 32, no. 10, pp. 7990–7997, 2017.

[11] D. H. Kohn, P. Ducheyne, and J. Awerbuch, "Acoustic emission during fatigue of Ti-6Al-4V: Incipient fatigue crack detection limits and generalized data analysis methodology," J. Mater. Sci., vol. 27, no. 12, pp. 3133–3142, 1992.

[12] C.-Y. Choe, W.-S. Jung, and J.-W. Byeon, "Damage evaluation in lithium cobalt oxide/carbon electrodes of secondary battery by acoustic emission monitoring," Mater. Trans., vol. 56, no. 2, pp. 269–273, 2015.

[13] S. Levikari, T. J. Karkkainen, C. Andersson, J. Tamminen, and P. Silventoinen, "Acoustic phenomena in damaged ceramic capacitors," IEEE Trans. Ind. Electron., vol. 65, no. 1, pp. 570–577, 2018.

[14] B. Legros, P. X. Thivel, Y. Bultel, M. Boinet, and R. P. Nogueira, "Acoustic emission: Towards a real-time diagnosis technique for Proton exchange membrane fuel cell operation," J. Power Sources, vol. 195, no. 24, pp. 8124–8133, 2010.

[15] T. J. Karkkainen et al., "Acoustic emission in power semiconductor modules-First observations," IEEE Trans. Power Electron., vol. 29, no. 11, pp. 6081–6086, 2014.

[16] C. Choe, C. Chen, and S. Noh, "Thermal shock performance of DBA / AMB substrates plated by Ni and Ni-P layers for high-temperature applications of power device modules," Materials., vol. 11, pp. 2394-1–13, 2018.

[17] R. Khazaka, L. Mendizabal, D. Henry, and R. Hanna, “Survey of high-temperature reliability of power electronics packaging components,” IEEE Trans. Power Electron., vol. 30, no. 5, pp. 2456–2464, 2015.

[18] K. Suganuma, S. Sakamoto, N. Kagami, D. Wakuda, K. S. Kim, and M. Nogi, “Low-temperature low-pressure die attach with hybrid silver particle paste,” Microelectron. Reliab., vol. 52, no. 2, pp. 375–380, 2012.

[19] S. Fu, Y. Mei, X. Li, C. Ma, and G. Q. Lu, “Reliability evaluation of multichip phase-leg IGBT modules using pressureless sintering of nanosilver paste by power cycling tests,” IEEE Trans. Power Electron., vol. 32, no. 8, pp. 6049–6058, 2017.

[20] J. Dai, J. Li, P. Agyakwa, M. Corfield, and C. M. Johnson, “Comparative thermal and structural characterization of sintered nano-silver and high-lead solder die attachments during power cycling,” IEEE Trans. Device Mater. Reliab., vol. 18, no. 2, pp. 256–265, 2018.

[21] F. Yu, J. Cui, Z. Zhou, K. Fang, R. W. Johnson, and M. C. Hamilton, “Reliability of Ag sintering for power semiconductor Die attach in high-temperature applications,” IEEE Trans. Power Electron., vol. 32, no. 9, pp. 7083–7095, 2017.

[22] S. Park, S. Nagao, T. Sugahara, and K. Suganuma, “Mechanical stabilities of ultrasonic Al ribbon bonding on electroless nickel immersion gold finished Cu substrates,” Jpn. J. Appl. Phys., vol. 53, no. 4 SPEC. ISSUE, 2014.

[23] M. Held, P. Jacob, G. Nicoletti, P. Scacco, and M.-. Poech, “Fast power cycling test of IGBT modules in traction application,” in Proceedings of Second International Conference on Power Electronics and Drive Systems, 1997, vol. 1, pp. 425–430 vol.1.

[24] JEDEC JESD 51-1 Integrated circuit thermal measurement method - electrical test method (single semiconductor device), 1995.

[25] C. Durand, M. Klingler, D. Coutellier, and H. Naceur, "Power cycling reliability of power module: A survey," IEEE Trans. Device Mater. Reliab., vol. 16, no. 1, pp. 80–97, 2016.

[26] J. A. Pascoe, D. S. Zarouchas, R. C. Alderliesten, and R. Benedictus, "Using acoustic emission to understand fatigue crack growth within a single load cycle," Eng. Fract. Mech., vol. 194, no. March, pp. 281–300, 2018.

[27] K. Rhodes, N. Dudney, E. Lara-Curzio, and C. Daniel, "Understanding the degradation of silicon electrodes for lithium-ion batteries using acoustic emission," J. Electrochem. Soc., vol. 157, no. 12, p. A1354, 2010.

[28] C. Buttay, C. Raynaud, H. Morel, M. Lazar, G. Civrac, and D. Bergogne, "High-temperature behavior of SiC power diodes," Proc. 2011 14th Eur. Conf. Power Electron. Appl. EPE 2011, no. October, pp. 0–9, 2011.

[29] S. Dusmez, H. Duran, and B. Akin, "Remaining useful lifetime estimation for thermally stressed power MOSFETs based on on-state resistance variation," IEEE Trans. Ind. Appl., vol. 52, no. 3, pp. 2554–2563, 2016.

[30] K. S. Siow and Y. T. Lin, "Identifying the development state of sintered silver (Ag) as bonding material in microelectronic packaging via a patent landscape study," J. Electron. Packag., vol. 138, no. c, pp. 1–18, 2016.

[31] C. Chen, C. Choe, Z. Zhang, D. Kim, and K. Suganuma, "Low-stress design of bonding structure and its thermal shock performance (− 50 to 250 °C) in SiC/DBC power die-attached modules," J. Mater. Sci. Mater. Electron., vol. 29, no. 16, pp. 14335–14346, 2018.

[32] C. Weber, M. Hutter, S. Schmitz, and K. D. Lang, "Dependency of the porosity and the layer thickness on the reliability of Ag sintered joints during active power cycling," Proc. - Electron. Components Technol. Conf., vol. 2015-July, pp. 1866–1873, 2015.

[33] A. Alghassi, S. Perinpanayagam, M. Samie, and T. Sreenuch, "Computationally efficient,

real-time, and embeddable prognostic techniques for power electronics," IEEE Trans. Power Electron., vol. 30, no. 5, pp. 2623–2634, 2015.

[34] P. D. Reigosa, H. Wang, Y. Yang, and F. Blaabjerg, "Prediction of bond wire fatigue of IGBTs in a PV inverter under a long-term operation," IEEE Trans. Power Electron., vol. 31, no. 10, pp. 7171–7182, 2016.

[35] K. Ma, U. Choi, and F. Blaabjerg GAE, "Prediction and validation of cumulative distribution function for power semiconductor devices with mission profiles in motor drive application," IEEE Trans. Power Electron., vol. 33, no. 11, pp. 9843–9853, 2018.

[36] A. K. Rao, "Acoustic emission and signal analysis" Def. Sci. J., vol. 40, no. 1, pp. 55–70, 1990.

[37] D. G. Aggelis and T. E. Matikas, "Effect of plate wave dispersion on the acoustic emission parameters in metals," Comput. Struct., vol. 98–99, pp. 17–22, 2012.

[38] P. J. de Groot, P. A. M. Wijnen, and R. B. F. Janssen, "Real-time frequency determination of acoustic emission for different fracture mechanisms in carbon/epoxy composites," Compos. Sci. Technol., vol. 55, no. 4, pp. 405–412, 1995.

[39] C. M. Scala and S. M. K. Cousland, "Acoustic emission during fatigue crack propagation in the aluminium alloys 2024 and 2124," Mater. Sci. Eng., vol. 61, no. 3, pp. 211–218, 1983.

[40] Z. Han, H. Luo, Y. Zhang, and J. Cao, "Effects of micro-structure on fatigue crack propagation and acoustic emission behaviors in a micro-alloyed steel," Mater. Sci. Eng. A, vol. 559, pp. 534–542, 2013.

[41] W. G. Clark, "Fracture mechanics in fatigue," Exp. Mech., vol. 11, no. 9, pp. 421–428, 1971.

[42] V. Moorthy, T. Jayakumar, and B. Raj, "Influence of microstructure on acoustic emission

behavior during stage 2 fatigue crack growth in solution annealed, thermally aged and weld specimens of AISI type 316 stainless steel," Mater. Sci. Eng. A, vol. 212, no. 2, pp. 273–280, 1996.

[43] C. K. Mukhopadhyay, G. Sasikala, T. Jayakumar, and B. Raj, "Acoustic emission during fracture toughness tests of SA333 Gr.6 steel," Eng. Fract. Mech., vol. 96, pp. 294–306, 2012.

[44] M. Chai, Z. Zhang, and Q. Duan, "A new qualitative acoustic emission parameter based on Shannon's entropy for damage monitoring," Mech. Syst. Signal Process., vol. 100, no. December 2017, pp. 617–629, 2018.

Chapter 5

Conclusions

In this thesis, thermal degradation mechanism of advanced package materials for high-temperature power modules, involving sintered micro-porous Ag and Ni-metalized DBA/AMB substrates, were presented. Additionally, a novel damage real-time monitoring method for power modules was developed.

In Chapter 1, the reliability issues of advanced package materials for high-temperature power electronics were summarized. The recent research trends of real-time failure monitoring as well as the used AE technique in this thesis were blifely described. The research objectives of the present thesis were also presented.

In Chapter 2, sintered micro-porous Ag was fabricated to evaluate its thermal aging mechanism. The changes in tensile strength, electrical resistivity and microstructural variations in sintered porous Ag were investigated during thermal exposure at 250 °C. The relationship between microstructural variations and mechanical/electrical properties was discussed. Tensile strength and electrical resistivity of sintered Ag was varified with thermal exposure time. Strength processed via three steps including deterioration, recovering, and maintaining during the thermal exposure up to 1000 hours. Electrical resistivity decreased in the middle of the thermal exposure period. On the other hands, Grain growth and pore coarsening occurred until 500 hours, while porosity mostly reduced from 200 to 500 hours. As it can be seen from the results, the decreased and recovered tensile strength results from Ag grain growth and porosity reduction in the different exposure time, respectively. Electrical resistivity decreased with exposure time especially from 200 to 500 hours. It was dominantly affected by porosity reduction that occurred in the same period.

In Chapter 3, DBA/AMB substrates with three types of ceramic plates and with two types of Ni metallization were fabricated. The thermal shock resistance and failure mechanism for substrates as well as metallizaion layers on substrates was evaluated under thermal shock test

between −50 °C and 250 °C. AMB substrates with AlN and Al_2O_3 fractured only after a thermal shock test of 10 cycles, while AMB with Si_3N_4 survived after a thermal shock test up to 1000 cycles. On the other hand, all DBA substrates were not fractured up to 1000 cycles. However, after 1000 cycles, Ni–P electroless plating layer on DBA/AMB substrates roughened and cracked, regardless of ceramic and metal type after 1000 cycles, while Ni electroplating did not cracked. As the result, the Ni-plated AMB substrates with Si_3N_4 as well as the Ni-plated DBA substrates with Al_2O_3, AlN, and Si_3N_4 are proposed as the most promising material designs for high-temperature power substrates. In addition, beneath a cracked Ni–P layer of DBA substrates, severe GBS deformation of Al was observed. It is presented that the GBS deformation of metal layers results in cracking and roughening of the Ni–P layer on metals.

Chapter 4 presents that the application of AE monitoring can detect of failure in power discrete SiC-SBD devices during power cycling test. A number of AE signals was successfully detected during power cycling test before reaching final failure. The initiation and propagation of fatigue cracks were observed in Al ribbon bonding, while there was no thermal damage in Ag die-attach joints. As it can be seen from the failure analysis results, the source of AE signals is attributed to the initiation and propagation of fatigue cracks leading to ribbon's lift-off failure. Thus, it demonstrates that AE has excellent sensitivity to fatigue cracking. AE acquisition can be used for a sensitive early warning method by detecting fatigue cracks leading to catastoplic ribbon's lift-off failure. The variation of AE count rate was divided into three stages. It was highly coreleated with the three step process of fatigue crack in Al ribbon bonding, defined as intiation, propagation, and catastrophic frature. The amlitiude of collected AE signals supports the corelation between AE activities and fatigue process. It can be concluded that AE monitoring offers not only to detect fatigue crack initiation and propagation accurately but also to provide early warning before catastrophic lift-off fracture.

Consequently, the thermal degradation mechanisms of Ag die-attach joints and DBA/AMB substrates were presented in this thesis. The most durable material designs were suggested for WBG power devices that require to operate at extremely high temperatures. In addition, novel AE monitoring was proposed as early warning method before catastrophic lift-off fracture of Al ribbon bonding.

List of publications

A. Papers

1. **Chanyang Choe**, Seungjun Noh, Chuantong Chen, Dongjin Kim, and Katsuaki Suganuma, "Influence of thermal aging upon mechanical and electrical properties of sintered porous silver during high temperature exposure", Microelectronics reliability, 88 (2018), 695–700.

2. **Chanyang Choe**, Chuantong Chen, Seungjun Noh, and Katsuaki Suganuma, "Thermal shock performance of DBA/AMB substrates plated by Ni and Ni-P layer for high temperature applications of power device modules", Materials, 11[12] (2018) 2394.

3. **Chanyang Choe**, Chuantong Chen, Shijo Nagao, and Katsuaki Suganuma, "Acoustic emission monitoring of fatigue damage in Al ribbon of power electronic devices during power cycling test", submitted (2020).

4. Seungjun Noh, **Chanyang Choe**, Chuantong Chen, and Katsuaki Suganuma, "Heat-resistant die-attach with cold-rolled Ag sheet", Applied Physics Express, 11 [1] (2018), 016501_1–4.

5. Seungjun Noh, **Chanyang Choe**, Chuantong Chen, and Katsuaki Suganuma, "Printed wire interconnection using Ag sinter paste for wide band gap power semiconductors", Journal of Materials Science: Materials in Electronics, 29 [17] (2018), 15223–15232.

6. Chuantong Chen, **Chanyang Choe**, Zheng Zhang, Dongjin Kim, and Katsuaki Suganuma, “Low-stress design of bonding structure and its thermal shock performance (− 50 to 250 °C) in SiC/DBC power die-attached modules”, Journal of Materials Science: Materials in Electronics, 29 [16] (2018), 14335–14346

7. Chuantong Chen, Zheng Zhang, **Chanyang Choe**, Dongjin Kim, Seungjun Noh, Toru Sugahara, and Katsuaki Suganuma, “Improvement of bond strength of Ag sinter joining on electroless Au plated substrate by one step preheating treatment”, Journal of Electronic Materials, 48[2](2019, 1106-1115.

8. Dongjin Kim, Chuantong Chen, Aiji Suetake, **Chanyang Choe**, Tohru Sugahara, Shijo Nagao, and Katsuaki Suganuma, “Development of thermal shock-resistant of GaN/DBC die-attached module by using Ag sinter paste and thermal stress relaxation structure”, Microelectronics Reliability, 88–90 (2018), 779–787.

9. Chuantong Chen, Seungjun Noh, Hao Zhang, **Chanyang Choe**, Jinting Jiu, Shijo Nagao, and Katsuaki Suganuma, “Bonding technology based on solid porous Ag for large area chip” Scripta Materialia, 146 [15] (2018), 123–127.

10. Jeyun Yeom, Shijo Nagao, Chuantong Chen, Tohru Sugahara, Hao Zhang, **Chanyang Choe**, Cai-Fu Li, and Katsuaki Suganuma, “Ag particles for sinter bonding: Flakes or spheres?”, Appl. Phys. Lett., 114 (2019), 253103.

11. Chuantong Chen, Dongjin Kim, Zhenghong Wang, Zheng Zhang, Yue Gao, **Chanyang Choe** and Katsuaki Suganuma. “Low temperature low pressure solid-state porous Ag bonding for large area and its high-reliability design in die-attached power modules”, Ceramics International, 45 [7] (2019), 9573-9579

B. Proceedings and Presentations

1. **Chanyang Choe**, Donjin Kim, Chuantong Chen, Seungjun Noh, Semin Park, and Katsuaki Suganuma, “(Invited lecture) Assembly and reliability of advanced packaging technologies in high-temperature SiC power modules” 2019 Fall Conference of the Korean Institute of Metals and Materials, Daegu, Korea, October 23-25 (2019)

2. **Chanyang Choe**, Seungjun Noh, Chuantong Chen, Dongjin Kim, and Katsuaki Suganuma “Influence of thermal exposure upon mechanical/electrical properties and microstructure of sintered micro-porous silver” 29th European symposium on reliability of electron devices, Failure physics and analysis (ESREF 2018), Aalborg, Denmark, October 1-5 (2018)

3. **Chanyang Choe**, Seungjun Noh, Chuantong Chen, Katsuaki Suganuma, “AE Evaluation of GaN Die-attach on DBC Substrate”, 14th international ceramics congress (CITEC 2018), Perugia, Italy, June 04–08, (2018).

4. **Chanyang Choe**, Seungjun Noh, Toshiyuki Ishina, Shijo Nagao and Katsuaki Suganuma, “Thermal effect on material properties of sintered porous silver during high temperature

ageing", 18th International Conference on Electronic Packaging Technology (ICEPT 2017), Harbin, China, August 16–18 (2017).

5. **Chanyang Choe**, Chuantong Chen, Aishi Suetake, Noriko Kagami, Shijo Nagao, Toshiyuki Ishina, Ichihito Narita, Seigo Kurosaka, and Katsuaki Suganuma, "Sinter Joining of GaN Die on DBA/DBC Substrates and Their Thermal Stability", MS&T2017, Pittsburgh, Pennsylvania, USA, October 8-12 (2017)

6. **Chanyang Choe**, Seungjun Noh, Toshiyuki Ishina, Chuantong Chen, Shijo Nagao and Katsuaki Suganuma, "Acoustic emission detection of Ag sinter joint failures of GaN power assembly", 161th annual meeting by the Japan institute of metal and materials, Sapporo, Japan, September 06–08 (2017).

7. **Chanyang Choe**, Seungjun Noh, Chuantong Chen, Toshiyuki Ishina, Shijo Nagao and Katsuaki Suganuma, "Thermal effect on the material properties of sintered porous silver during high temperature ageing", 2017 International Conference on Electronic Packaging Technology (ICEPT 2017), Harbin, China, August 16-18 (2017)

8. Chuantong Chen, **Chanyang Choe**, and Katsuaki Suganuma, "Large area bonding technology by using solid porous Ag in die-attached modules", 14th International ceramics congress(CIMTEC 2018), Perugia, Italy, June 4-8 (2018)

9. Seungjun Noh, **Chanyang Choe**, Chuantong Chen, Hao Zhang, and Katsuaki Suganuma

“Bonding technology using cold-rolled Ag sheet in die-attachment applications”, International Power Electronics Conference (IPEC 2018), Niigata, Japan, May 20-24 (2018)

10. Katsuaki Suganuma, Naoki Sato, Aishi Suetake, **Chanyang Choe**, Toru Sugahara, Shijo Nagao, and Chuantong Chen, “(Invited lecture) Packaging Material Technology for Wide Band Gap Power Devices and Its Performance/Reliability Evaluation” Americas International Meeting on Electrochemistry and Solid State Science (AiMES2018), Cancun, Mexico, September 30 to October 4 (2018)

11. Chuantong Chen, Aiji Suetake, **Chanyang Choe**, Seungjun Noh, Katsuaki Suganuma, “Low-stress Bonding Technology Design for SiC Power Die-attached Modules”, 14th International Forum on Wide Bandgap Semiconductors 2017 (IFWS2017), Beijing, China, November 1–3 (2017).